

# **Characterization of the Auroral Electrojet and the Ambient and Modified D Region for HAARP Using Long-Path VLF Diagnostics**

**Timothy F. Bell**

**STAR Laboratory, 350 Serra Mall  
Stanford University  
Stanford CA 94305-9515**

**15 Mar 2001**

**Final Report**

<b>APPROVED FOR PUBLIC RELEASE; DISTRIBUTION IS UNLIMITED.</b>
--



**AIR FORCE RESEARCH LABORATORY  
Space Vehicles Directorate  
29 Randolph Rd  
AIR FORCE MATERIEL COMMAND  
Hanscom AFB, MA 01731-3010**

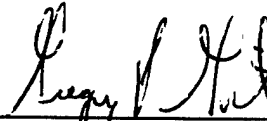
---

**20020815 058**

"This technical report has been reviewed and is approved for publication"



JAMES C. BATTIS  
Contract Manager



GREGORY P. GINET  
Branch Chief

This report has been reviewed by the ESC Public Affairs Office (PA) and is releasable to the National Technical Information Service (NTIS).

Qualified requestors may obtain additional copies from the Defense Technical Information Center (DTIC). All others should apply to the National Technical Information Service (NTIS).

If your address has changed, if you wish to be removed from the mailing list, or if the addressee is no longer employed by your organization, please notify AFRL/VSIP, 29 Randolph Road, Hanscom AFB, MA 01731-3010. This will assist us in maintaining a current mailing list.

Do not return copies of this report unless contractual obligations or notices on a specific document require that it be returned.

**REPORT DOCUMENTATION PAGE**Form Approved  
OMB No. 0704-0188

Public reporting burden for this collection of information is estimated to average 1 hour per response, including the time for reviewing instructions, searching existing data sources, gathering and maintaining the data needed, and completing and reviewing this collection of information. Send comments regarding this burden estimate or any other aspect of this collection of information, including suggestions for reducing this burden to Department of Defense, Washington Headquarters Services, Directorate for Information Operations and Reports (0704-0188), 1215 Jefferson Davis Highway, Suite 1204, Arlington, VA 22202-4302. Respondents should be aware that notwithstanding any other provision of law, no person shall be subject to any penalty for failing to comply with a collection of information if it does not display a currently valid OMB control number. PLEASE DO NOT RETURN YOUR FORM TO THE ABOVE ADDRESS.

**1. REPORT DATE (DD-MM-YYYY)**

15 March 2001

**2. REPORT TYPE**

Final

**3. DATES COVERED (From - To)**

09/27/96-12/31/99

**4. TITLE AND SUBTITLE**

Characterization of the Auroral Electrojet and the Ambient and Modified D region for HAARP using long-path VLF diagnostics

**5a. CONTRACT NUMBER**

F19628-96-C-0149

**5b. GRANT NUMBER****5c. PROGRAM ELEMENT NUMBER**

61102p

**6. AUTHOR(S)**

Bell, Timothy F.

**5d. PROJECT NUMBER**

4266

**5e. TASK NUMBER**

GH

**5f. WORK UNIT NUMBER**

AG

**7. PERFORMING ORGANIZATION NAME(S) AND ADDRESS(ES)**

STAR Laboratory  
Stanford University  
Stanford, California  
94305

**8. PERFORMING ORGANIZATION REPORT NUMBER****9. SPONSORING / MONITORING AGENCY NAME(S) AND ADDRESS(ES)**

Air Force Research Laboratory  
29 Randolph Road  
Hanscom AFB, Maine 01731-3010  
Contract Manager: James  
Battis/VSBXI

**10. SPONSOR/MONITOR'S ACRONYM(S)****11. SPONSOR/MONITOR'S REPORT NUMBER(S)**

AFRL-VS-TR-2001-1573

**12. DISTRIBUTION / AVAILABILITY STATEMENT**

Approved for public release; distribution unlimited

**13. SUPPLEMENTARY NOTES****14. ABSTRACT**

During the period of performance a program of instrument construction, technique development, data acquisition, and data analysis was carried out in order to characterize the auroral electrojet and the ambient and modified D-region directly above and near the HAARP (High Frequency Active Auroral Research Program) facility in Alaska. To accomplish this goal, five VLF D-region diagnostic systems were constructed and deployed in five High Schools near the HAARP facility and along the west coast of Alaska. In addition in order to characterize the auroral electrojet on a continental scale and to allow prediction of its location, four VLF D-region diagnostic systems were constructed and deployed in four High Schools on the east coast of the United States and Canada. Data from the complete array of D-region diagnostic systems was acquired during a number of Fall and Spring HAARP campaigns during the period of performance. This data was then used to determine the state of the D-region above HAARP during the campaigns and to provide information on the location of the auroral electrojet. The salient scientific results from the observations were published in the scientific literature and also reported at the annual RF Ionospheric Interactions Workshop in Santa Fe, New Mexico. In addition a portion of this data formed one of the the bases of a Ph.D. dissertation completed at Stanford University.

**15. SUBJECT TERMS**

Ionospheric D-region, Enhanced electron density, VLF and HF wave absorption

**16. SECURITY CLASSIFICATION OF:****a. REPORT**

Unc1

**b. ABSTRACT**

Unc1

**c. THIS PAGE**

Unc1

**17. LIMITATION OF ABSTRACT**

Unc1

**18. NUMBER OF PAGES**

110

**19a. NAME OF RESPONSIBLE PERSON**

J. Battis/VSBXI

**19b. TELEPHONE NUMBER (include area code)**

**TABLE OF CONTENTS**

<b>Section</b>	<b>Page</b>
Title Page	1
Report Documentation Page	2
Table of Contents	3
1. Contract purpose	4
2. Work Provided	4
3. Instrumentation	5
4. Results of HAARP Campaigns	6
5. Appendix	7

## **1. CONTRACT PURPOSE**

The purpose of this contract (F19628-96-C-0149) was to carry out a program of instrument construction, technique development, data acquisition, and data analysis in order to characterize the auroral electrojet and the ambient and modified D-region directly above and near the HAARP (High Frequency Active Auroral Research Program) facility in Alaska. To accomplish this goal, five VLF D-region diagnostic systems were constructed and deployed in five High Schools near the HAARP facility and along the west coast of Alaska. In addition, to characterize the auroral electrojet on a continental scale and to allow prediction of its location, four VLF D-region diagnostic systems were constructed and deployed in four High Schools on the east coast of the United States and Canada. Data from the complete array of D-region diagnostic systems was acquired during a number of Fall and Spring HAARP campaigns during the period of performance. This data was then used to determine the state of the D-region above HAARP during the campaigns and to provide information on the location of the auroral electrojet. This information was essential to the understanding of how the HAARP HF signal interacted with the charged constituents of the D-region to produce ULF/ELF/VLF waves.

## **2. WORK PROVIDED**

During the period of performance of this contract, Stanford University carried out the following tasks:

Task 1: Stanford performed contract management, reporting, and technical overview activities of contracted work.

Task 2: Stanford constructed and assembled nine identical VLF D-region Diagnostics Systems whose purpose was to allow the characterization of the auroral electrojet and the ambient and modified D-region directly above and near the HAARP facility in Alaska.

Task 3: Stanford identified nine High Schools in which to house the VLF D-region diagnostics systems, and erected loop antennas at these sites to detect three subionospheric VLF signals from

three VLF transmitters that propagated above the HAARP facility. At each site the system was linked to the internet with the help of the local High School science teacher.

Task 4: Stanford supplied computer code to digitally measure at each High School the phase and amplitude of three subionospheric VLF signals from three VLF transmitters which propagated above the HAARP facility. These data files were sent through the internet to Stanford where the data were analyzed and posted on a Stanford internet page which was open to the public as well as HAARP scientists .

Task 5: Stanford acquired data with the deployed array of VLF D-region diagnostic systems in support of each Spring and Fall HAARP campaign during the period of performance. This data was analyzed and the scientific results were presented at the annual RF Ionospheric Interactions Workshop in Santa Fe, New Mexico. Experiment results were also published in the scientific literature, and formed one of the bases of a Ph.D. dissertation at Stanford University.

### 3. INSTRUMENTATION

Each of the nine VLF D-region Diagnostics Systems constructed under this contract operates in the same manner. At each site the VLF signals from the loop antenna is fed into a preamplifier box and sent to a line receiver where the signals are broadband filtered to remove high frequency noise and clipped to prevent saturation from nearby lightning sources. The signal is sampled by an A/D network under computer control at a rate of 100 kHz, and the data is buffered to a hard disk. Accurate time is provided through a GPS receiver. The buffered data are then formatted and sent to a Stanford University server by FTP over the internet.

Data from the hard disk are used in one of two ways. For determining the phase and amplitude of subionospheric VLF signals, the data are digitally filtered to provide a pass band of approximately 100 Hz centered on the VLF carrier of interest. This low bit rate data is then analyzed to obtain signal phase and amplitude. To determine the character and distribution of VLF signals over the entire 50 kHz passband, the data is Fourier analyzed and presented as a spectrogram. This high bit rate data is important in identifying local sources of VLF noise that may affect the

narrow band data, but requires much more memory. Thus it is generally used only in special circumstances.

#### 4. RESULTS OF HAARP CAMPAIGNS

Data acquired with the VLF D-region Diagnostics Systems during the period of performance have been analyzed and the results reported at the annual RF Ionospheric Interactions Workshops in Santa Fe, New Mexico. Results have also been published in the scientific literature and used in a Ph.D. dissertation at Stanford University, as documented below. This Ph.D. dissertation is reproduced in the Appendix.

Inan, U. S., N. G. Lehtinen, S. J. Lev-Tov, M. P. Johnson, T. F. Bell, and K. Hurley, Ionization of the lower ionosphere by  $\gamma$  -rays from a magnetar: detection of a low energy (3-10 keV) component, *Geophys. Res. Lett.*, 26, 3357, 1999.

Demirkol, M. K., U. S. Inan, T. F. Bell, S. G. Kanekal, and D. C. Wilkinson, Ionospheric effects of relativistic electron enhancement events, *Geophys. Res. Lett.* 26, 3557, 1999.

Demirkol, M. K., VLF remote sensing of the ambient and modified lower ionosphere, Ph.D. Dissertation, Stanford University, November, 1999.

## 5. APPENDIX

The methodology involved in determining the modified D-region temperature and collision frequency profiles utilizing the data collected at the three HAARP VLF D-region Diagnostics sites is described in the Ph.D. thesis of Dr. M. K. Demirkol. This thesis is presented on the following pages.



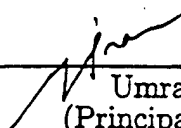
VLF REMOTE SENSING OF THE AMBIENT AND  
MODIFIED LOWER IONOSPHERE

A DISSERTATION  
SUBMITTED TO THE DEPARTMENT OF ELECTRICAL ENGINEERING  
AND THE COMMITTEE ON GRADUATE STUDIES  
OF STANFORD UNIVERSITY  
IN PARTIAL FULFILLMENT OF THE REQUIREMENTS  
FOR THE DEGREE OF  
DOCTOR OF PHILOSOPHY

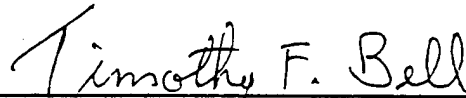
Mehmet Kürşad Demirkol  
November 2001

© Copyright 2001 by Mehmet Kürşad Demirkol  
All Rights Reserved

I certify that I have read this dissertation and that in my opinion it is fully adequate, in scope and quality, as a dissertation for the degree of Doctor of Philosophy.

  
\_\_\_\_\_  
Umran Inan  
(Principal Adviser)

I certify that I have read this dissertation and that in my opinion it is fully adequate, in scope and quality, as a dissertation for the degree of Doctor of Philosophy.

  
\_\_\_\_\_  
Timothy F. Bell

I certify that I have read this dissertation and that in my opinion it is fully adequate, in scope and quality, as a dissertation for the degree of Doctor of Philosophy.

  
\_\_\_\_\_  
Brad Osgood

Approved for the University Committee on Graduate Studies:

  
\_\_\_\_\_

# Dedication

To my parents  
*Sait and Sevim*  
and to my brother and sister  
*Fatih and Hilâl*

# Abstract

Electron density and temperature changes in the  $D$  region are sensitively manifested as changes in the amplitude and phase of subionospheric Very Low Frequency (VLF) signals propagating beneath the perturbed region. Both localized and large scale disturbances (either in electron density or temperature) in the  $D$  region cause significant scattering of VLF waves propagating in the earth-ionosphere waveguide, leading to measurable changes in the amplitude and phase of the VLF waves. Large scale auroral disturbances, associated with intensification of the auroral electrojet, as well as ionospheric disturbances produced during relativistic electron enhancements, cause characteristic changes over relatively long time scales that allow the assessment of the 'ambient' ionosphere. Localized ionospheric disturbances are also produced by powerful HF transmitting facilities such as the High Power Auroral Stimulation (HIPAS) facility, the High frequency Active Auroral Research Program (HAARP), and also by lightning discharges. Amplitude and phase changes of VLF waveguide signals scattered from such artificially heated ionospheric patches are known to be detectable. In this study, we describe a new inversion algorithm to determine altitude profiles of electron density and collision frequency within such a localized disturbance by using the measured amplitude and phase of three different VLF signals at three separate receiving sites. For this purpose a new optimization algorithm is developed which is primarily based on the recursive usage of the three dimensional version of the Long Wave Propagation Capability (LWPC) code used to model the subionospheric propagation and scattering of VLF signals in the earth-ionosphere waveguide in the presence of ionospheric disturbances.

## Acknowledgements

My research was supervised by Professor Umran S. Inan, and Dr. Timothy F. Bell. I am grateful to Prof. Inan for his support, encouragement and patient guidance. I would like to thank Dr. Bell for his invaluable suggestions and comments.

Thanks also are due to the members of VLF group who were generally friendly and helpful. I would like to thank Michael Chevalier for his dedicated help during the March 1999 HAARP experiments in Alaska. I would like to thank Sean Lev-Tov and Steve Cummer for their patient answers to my questions concerning LWPC modeling. I would like to thank Michael Johnson for his Matlab support and his support during our field campaign in Alaska.

I would like to thank teachers Michelle and Michael Balars from Healy Lake school, and Michael Lutes from Wasilla High School, for their generous support and help during the March 1999 HAARP experiments.

I would like to thank my old friend Aykutlu Dâna for his constant help and support during our years in the university. Now our paths seem to be drifting apart. No way.

I had constant support and motivation from Leyla Özşen, who was one of the loveliest aspects of my life at Stanford.

Most of all, I am grateful for the generous support and encouragement of my parents. Without their prayers I would never find the strength to start and to finish this work. I would like to thank my sister, Hilâl for her random phone calls filling me with joy and my brother Fatih who has given me the motivation to be a better student so that I could be a better example for him.

This research was supported by the Air Force Phillips Laboratory through grant F19628-96-C-0149.

# Contents

<b>Dedication</b>	<b>iv</b>
<b>Abstract</b>	<b>v</b>
<b>Acknowledgements</b>	<b>vi</b>
<b>1 Introduction</b>	<b>1</b>
1.1 The Ionosphere . . . . .	2
1.2 The Earth-Ionosphere Waveguide . . . . .	4
1.3 VLF Propagation Models . . . . .	9
1.4 Ionospheric Heating . . . . .	14
1.4.1 The Luxembourg Effect . . . . .	16
1.4.2 HF/VLF Coupling . . . . .	17
1.4.3 VLF Diagnostics of the Modified <i>D</i> region . . . . .	20
1.5 Contributions . . . . .	22
<b>2 VLF Signal Propagation Models</b>	<b>25</b>
2.1 Long Wave Propagation Capability . . . . .	25
2.1.1 PRESEG . . . . .	28
2.1.2 MODEFINDER . . . . .	29
2.1.3 FASTMC . . . . .	29
2.1.4 Example 2D simulation . . . . .	30
2.2 3D Numerical Modeling . . . . .	32
2.2.1 SCATTER . . . . .	37

## CONTENTS

viii

2.2.2	SUMOUT . . . . .	37
2.3	Analysis of a Single Mode Case . . . . .	37
<b>3</b>	<b>Ambient Electron Density Profile</b>	<b>46</b>
3.1	Ionospheric Effects of Relativistic Electron Enhancement Events . . .	47
3.1.1	Description of data . . . . .	50
3.1.2	Ground and Satellite Data Comparisons . . . . .	52
3.1.3	Model Calculations . . . . .	54
3.2	Determination of the Electron Density Profile . . . . .	60
<b>4</b>	<b>Modified Collision Frequency</b>	<b>64</b>
4.1	HF Heater-Induced Modification of Electron Collision Frequency . . .	65
4.2	Inversion Algorithm to Determine $\nu(z)$ . . . . .	69
<b>5</b>	<b>March 1999 HAARP Campaign</b>	<b>78</b>
5.1	HAARP Facility Description . . . . .	78
5.2	VLF Remote System . . . . .	81
5.3	Experimental Results . . . . .	82
5.4	Example Inversion of VLF data from 25 March 1999 . . . . .	87
5.4.1	Data Selection and Calibration . . . . .	90
5.4.2	The Ambient Electron Density Profile . . . . .	93
5.4.3	The Modified Collision Frequency Profile . . . . .	98
<b>6</b>	<b>Summary and Suggestions for Future Work</b>	<b>101</b>
6.1	Summary . . . . .	101
6.2	Suggestions for Future Work . . . . .	103
6.2.1	Improved Electron Density Model . . . . .	103
6.2.2	Future Experiments . . . . .	103
	<b>Bibliography</b>	<b>105</b>



## List of Tables

1.1	Locations of VLF Receiver FY and heating facility HIPAS in Alaska.	18
1.2	List of VLF transmitters used during HIPAS 1992 Campaign . . . . .	18
4.1	Amplitude and phase changes for the original and regenerated collision frequency profiles. . . . .	75
5.1	List of HAARP Diagnostic tools. . . . .	81
5.2	List of VLF receivers used in the VLF Diagnostic System during HAARP 1999 Campaign . . . . .	82
5.3	List of VLF transmitters used during HAARP 1999 Campaign . . . . .	82
5.4	List of the amplitude and phase measurements at Healy. . . . .	89
5.5	List of the amplitude and phase measurements at Wasilla. . . . .	89
5.6	List of the amplitude and phase measurements at Delta Junction. . .	90
5.7	The measured values of the transmitter signals at the receivers and model results. . . . .	96

# List of Figures

1.1	Typical midlatitude ionospheric electron density profile for sunspot maximum and minimum conditions during day-time and night-time. The different altitude regions in the ionosphere are labelled with $D$ , $E$ , $F_1$ , and $F_2$ [Richmond, 1987]. . . . .	5
1.2	VLF signal propagation can be thought of as repeated reflection back and forth in the earth-ionosphere waveguide. . . . .	6
1.3	(a) Typical nighttime electron density as a function of altitude in the $D$ region. (b) A typical model for the effective electron collision frequency versus altitude in the lower ionosphere. . . . .	8
1.4	(a) <b>Ray Paths.</b> Possible discrete ray paths from a transmitter to a receiver. There are an integral number of reflections. Only the first three ray paths are indicated. For the $n^{th}$ order ray path there are $2^{n-1}$ reflection points in the ionosphere. (b) <b>Waveguide modes.</b> The vertical variation of the field amplitude of different modes are shown. The labels $\vec{F}_0$ and $\vec{F}_1$ are referred to later in connection with equation (1.12). Also shown are raypaths for component uniform plane waves (solid and dashed) the superposition of which can be used to represent the waveguide modes. Each mode corresponds to an incidence angle $\theta_n$ for the component waves. . . . .	11

1.5	When the Earth surface is treated as a perfect electric conductor and the ionosphere is treated as a perfect magnetic conductor, we find $R^e = 1$ and $R^i = -1$ . Thus the resonance mode condition gives us the eigenangles in the figure for $h = 85$ km and $k = \omega/c = (2\pi)(25 \text{ kHz})/(3 \times 10^8 \text{ m/s}) = 5.2359 \times 10^{-4} \text{ m}^{-1}$ . The numbers refer to the mode numbers $n$ .	15
1.6	Geometry and nomenclature involved in ionospheric cross-modulation.	16
1.7	Configuration of the great circle paths between the three VLF transmitters and the observation site at Fort Yukon, Alaska	19
1.8	(a) Raw NPM amplitude data recorded at FY while the HIPAS receiver was ON for 100 ms and OFF for 400 ms (2Hz periodicity), repeated for 28 min. (b) Superposed epoch analysis (with $T=500$ ms) of the raw data set from (a). (c) Spectral analysis of the raw data set from (a). (d) Superposed epoch analysis with $T=500$ ms of raw NPM phase data at FY during which the HIPAS HF heater was on for 100 ms and off for 400 ms (2 Hz periodicity) (e) Spectral analysis of the same raw data [Bell et al., 1995].	21
1.9	Development of algorithm for extraction of $D$ region electron collision frequency profile from VLF amplitude and phase changes measured at three different sites.	23
2.1	The geometry of the 2D VLF signal propagation problem. The properties of the ionosphere and the Earth are assumed to be constant in the $y$ direction.	26
2.2	Flow diagram for the LWPC code for 2D modeling of VLF signal propagation in the earth-ionosphere waveguide. <b>TTTRR.lwpc</b> is the input model file which contains the required parameters for the three FORTRAN programs, namely PRESEG, MODEFINDER and FASTMC, described in the text.	28
2.3	NLK-FY path for the 2D simulation of VLF signal propagation.	32

## LIST OF FIGURES

xii

2.4	Eigenangle solutions found by MODEFINDER for the NLK signal propagating to FY for the first segment of the path. Each point corresponds to a different mode as indicated. . . . .	33
2.5	The amplitude and phase of the VLF signal changes as it propagates in the earth-ionosphere waveguide. The solid lines correspond to the forced and natural boundaries on the propagation path as segmented by PRESEG. . . . .	34
2.6	Illustration of the 3D modeling of the VLF wave propagation in the presence of a localized disturbance. The main leg corresponds to the GCP between the transmitter and the receiver. The signal at the receiver consists of a vector sum of the direct signal along the Main Path and the scattered signal arriving from Leg 2. . . . .	35
2.7	Flow of the LWPC code for 3D simulation of VLF signal propagation in the earth-ionosphere waveguide. In this model, VLF signal propagation is simulated on two different legs denoted as Main and Leg 1 in Figure 2.6. The scattered field is calculated by the FORTRAN program SCATTER and another simulation is carried out for the propagation of this scattered field to the receiver, over the path denoted as Leg 2. Finally SUMOUT calculates the total electric field that is received. . . . .	36
3.1	Configuration of NLK-FY path with respect to SAMPEX measurements of the relativistic precipitation zone. The NLK-FY path is chosen since the strongest flux levels are at the subauroral latitudes traversed by this path. . . . .	48
3.2	The particle flux measured on the GOES-7 and SAMPEX satellites exhibits the well known relatively regular 27-day periodicity with typical rises on a 2 to 3-day time scale and decays on a 3 to 4-day scale. . . .	49

- 3.3 (a) A geographic view of the VLF propagation path from NLK to Fort Yukon, Alaska. The NLK-FY path is situated such that the relativistic precipitation region (shown shaded) covers a significant portion of the great circle propagation path. (b) The mechanism of the particle precipitation-VLF interaction is schematically shown above. A ground VLF transmitter (T) launches a signal into the earth-ionosphere waveguide. In the region of relativistic particle precipitation the local electron density is increased by  $\Delta N_e$ , causing the local electrical conductivity to change. The waveguide signal propagating under the region of relativistic electron precipitation is modified in response to the conductivity change, allowing the observation of this conductivity change as phase and amplitude variations in the VLF signal. . . . . 51
- 3.4 (a) The three-hour-averaged amplitude of the NLK signal (24.8 kHz) at Fort Yukon (FY) on each day. (b) Electron precipitation flux as measured on GOES-7. A 27-day variation is apparent in each data set. 53
- 3.5 VLF signal amplitudes on days 300 and 307 shown in the interval 0600-0900 UT. The difference in the amplitude for these two days is  $> 10$  dB. VLF signal amplitude from Day 307 corresponds to a day where an electron precipitation enhancement takes place, while the signal from Day 300 is a day where the relativistic electron flux level is moderate. 55
- 3.6 5-minute average GOES-7 data appears to be strongly correlated with VLF amplitude. Correlation coefficients up to  $\sim -0.7$  are calculated. 56
- 3.7 (a) Ionization profiles corresponding to the different levels (1, 2, 3, 4, 5) of relativistic electron precipitation fluxes as shown in (b) A typical relativistic electron precipitation enhancement shown here rising and falling in 9 days. In many cases event durations are as much as 10-15 days. The flux levels and energy spectra of the precipitation was taken to be as given by *Gaines et al.* [1995], based on measurements on the UARS satellite. . . . . 58

# LIST OF FIGURES

xiv

3.8	(a) Integral flux of $> 4$ MeV electrons measured on each day on SAM-PEX during passes nearest (in longitude) to the NLK-FY path. The largest flux variation generally occurs near $L \sim 6$ . (b) Flux level at $L = 6$ as a function of day. . . . .	58
3.9	The predicted NLK signal amplitude variation as observed at Fort Yukon. . . . .	59
3.10	The flux level is modeled as a Gaussian centered at $L = 6$ . Since each flux level corresponds to a different electron density profile, it is possible to segment the propagation path, each segment including the corresponding electron density profile as shown a, b, c and d above. . . . .	61
3.11	The segmentation of the VLF propagation path from NAA to Wasilla according to the Gaussian spatial flux model centered at $L = 6$ . . . . .	62
4.1	Calculated disturbed collision frequency profile for a given ambient collision frequency and electron density profile. The assumed angle between the wave normal and $\vec{B}$ is $13.5^\circ$ . The frequency of the heater wave is 2.86 MHz, and the two mode combined power of the HF transmitter is $9.3 \times 10^{-4}$ watts/m <sup>2</sup> . . . . .	68
4.2	Collision frequency profile is modeled with six different values of collision frequency at six different altitudes in the $D$ -region. The altitude range sampled is chosen on the basis of the sensitivity of the subionospheric VLF signal to changes at different altitudes. . . . .	70
4.3	Three VLF signals with different frequencies propagating under a heated region will be used in the inversion technique. The propagation paths of the signals from the transmitters (T) to the receivers (R) are also different, since in general each VLF transmitter operates at a pre-allocated frequency. . . . .	71
4.4	Flow graph for the inversion algorithm. . . . .	73
4.5	For a single VLF signal each iteration corresponds to finding the amplitude and phase change for 12 different collision frequency profiles generated by $\bar{\nu}^m \pm \delta_j \bar{\nu}^m$ for $j = 1, 2, \dots, 6$ and choosing the profile which results in the smallest error value. . . . .	74

# LIST OF FIGURES

xv

4.6	Tests of the inversion algorithm. (a) Example 1; (b) Example 2. . . .	76
4.7	Collision frequency profiles used to find the best initial profile to be used in the inversion algorithm. . . . .	77
5.1	The HAARP HF prototype transmitting array. . . . .	79
5.2	Effects spanning 16 decades in frequency produced by HAARP. . . .	80
5.3	VLF transmitter and receiver locations. . . . .	83
5.4	Receiver locations with respect to the circular region heated by HAARP. The receivers are located such that the propagation paths of the VLF signals pass through the heated region. . . . .	84
5.5	Superposed epoch analysis results and spectra of the NPM, NAA and NLK signal amplitudes observed at Delta Junction, Wasilla and Healy respectively, between 05:45-06:00 UT on 03/25/1999. The 25 Hz modulation is apparent on the NLK and NPM signals. The peak at 39 Hz on the NPM signal is due to local interference. . . . .	85
5.6	Amplitude and phase modulations of the VLF signal from NLK as received at Healy. A 25 Hz modulation is clear both in the time and frequency domains. . . . .	86
5.7	NLK amplitude spectrum from 06:40 to 07:05 in 5 minute intervals on 03/10/1999. It is clear that the amplitude modulation is due to HAARP. . . . .	88
5.8	On the left panels, superposed epoch analysis of amplitude and phase data from NLK and NPM are shown. On the right panels, the spectra of the respective data are shown. . . . .	91
5.9	NAA amplitude shows no 25 Hz modulation on 03/25/1999. . . . .	92
5.10	The overall transfer function $D_{out}/E_{in}$ consists of three transfer functions, gain of the antenna, gain of the analog front end, and gain of the digital receiver. . . . .	92
5.11	Calibration plots for the receivers at Wasilla, Delta Junction and Healy. . . . .	94
5.12	Different electron density profiles used in the modeling of the Gaussian spatial distribution centered at $L = 6$ . . . . .	95

## LIST OF FIGURES

xvi

5.13	The GCP paths of the three VLF signals are divided into segments where the electron density profiles are different and correspond to a Gaussian flux level model as described in Chapter 3. . . . .	96
5.14	Different electron density profiles shown here are plotted in the same color as the segments of the propagation paths where they are used to model the ionosphere. . . . .	97
5.15	Amplitude and phase change pairs arrived at in different steps $m$ of the iterative inversion process. The measured amplitude and phase change is shown by the circle. . . . .	99
5.16	Collision frequency profile used as an initial estimation, the final profile generated at the end of the inversion, and the theoretically expected profile is shown. . . . .	100



# Chapter 1

## Introduction

This dissertation describes the development of an inversion process which uses amplitude and phase changes of coherent subionospheric electromagnetic signals radiated by *very-low-frequency* transmitters to determine the electron collision frequency profile in a localized region of the Earth's lower ionosphere which is artificially modified by powerful High Frequency radiowave heating. The Very-Low-Frequency (VLF) signals constitute the portion of the spectrum between 3 kHz and 30 kHz, although in this work we are mostly interested in the range 20 kHz and 30 kHz, i.e., the upper end of the VLF spectrum. The *ionosphere* consists of a number of ionized regions above the Earth's surface, and plays a very important part in global communication and navigation systems [Kelley, 1989]. The so-called *D* region, lying between 60 to 90 km altitude, is a good reflector for VLF waves, the approximate height of reflection for 20-30 kHz waves varying from ~65 km during the day to ~85 km during the night. This lowest portion of the ionosphere is the partially ionized atmospheric region that is generally a difficult region to measure, being too high for aircraft and for balloons, too low for orbiting satellites, and having too few electrons for effective measurements by high and very high frequency direct line-of-sight radar systems. Ground-based radio remote sensing at very low frequencies is the most effective method for studying this region [Sechrist, 1974].

The fact that VLF waves are effectively reflected by the *D* region can be exploited to measure the electrical conductivity of this region. The *D* region conductivity

depends upon both the number density and temperature of the ambient electrons. Thus, the amplitude and phase of VLF waves propagating via reflection between the ionosphere and the conducting Earth are sensitively dependent on changes in the volume density and temperature of the ambient electrons. Effects of the electron temperature on conductivity are typically expressed in terms of the frequency of the collisions of the electrons with neutral atmospheric constituents. The specific problem investigated in this dissertation is the inversion of the amplitude and phase changes in the VLF signals in order to determine the electron collision frequency profile within an ionospheric region illuminated by a powerful high frequency radio transmitter. In this chapter we provide a brief background on the ionosphere, the earth-ionosphere waveguide, very low frequency propagation, and the so-called Luxembourg effect. We also describe and formulate the scientific problem addressed herein and list the contributions of this dissertation.

## 1.1 The Ionosphere

The ionosphere is a region of the atmosphere extending from an altitude of about 60 to more than 1000 km in which there exists a significant number of free electrons and ions. The presence of these freely mobile carriers of electric current makes this region an electrical conductor, which reflects waves over a broad range of frequencies.

The existence of an ionized layer in the upper atmosphere was appreciated at the beginning of the 20<sup>th</sup> century. Marconi demonstrated that radio waves could propagate across large distances beyond the horizon, as if they were guided between a conducting layer and the ground. Even as early as 1878, Stewart [Stewart, 1878], from the studies of diurnal oscillations in the Earth's magnetic field, indicated that these variations might be due to tidal oscillations in the upper atmosphere. However only in 1924 was the existence of an ionized conducting layer fully proven. Appleton and Barnett [Appleton and Barnett, 1925] in England and Breit and Tuve [Breit and Tuve, 1926] in the USA, on both sides of Atlantic, conducted experiments demonstrating the existence of the ionosphere.

The existence of the ionosphere is a consequence of two commonly known properties of the atmosphere. First, the density of the atmosphere decreases with altitude above the Earth's surface, and second, the atmosphere absorbs much of the ultraviolet (UV) and higher energy radiation incident upon it from the Sun and other cosmic sources. Incoming high energy radiation ionizes the atmospheric constituents. At heights of the order of 1000 km or more the medium is almost fully ionized, but so tenuous that the ion and the electron concentrations are relatively small. At lower levels there is more air to be ionized so that the radiation is more strongly absorbed and the electron and ion concentrations are higher. The ions and free electrons created this way are absorbed by chemical interactions (recombination and attachment processes) with other ions and atoms, leading to a dynamic equilibrium between the production of the electrons and their absorption, resulting in an average finite free electron and ion density. At still lower altitudes the air density is so high that the absorption process dominates and resulting in much lower free electron densities.

The ionosphere can be viewed as a variable shell of plasma surrounding the Earth. Above 1000 km the atmosphere is a fully ionized plasma and is therefore a relatively good electrical conductor. Furthermore, the density of air is so low that free electrons and ions do not undergo collisions with other ions or molecules, and can freely move under the influence of electromagnetic fields. Under these conditions the Earth's magnetic field has a strong effect on the structure of the medium, and the region is thus known as *magnetosphere*. It extends out to a distance of  $14R_E$  on the sunlit side of the Earth, where  $R_E \simeq 6400$  km is the radius of the Earth.

Historically the ionosphere has been divided into layers, the earliest detected being the *E* layer, so named due to reflection of electric fields. The *D* and *F* layers are below and above the *E* layer respectively. The *D* region, between 60 and 90 km is highly variable with much lower electron density. However, the electron density in all of these regions widely varies with time of day, season, solar cycle and the level of magnetospheric and/or solar wind activity [Davies 1965; p. 265]. The focus of our attention in this work is the *D* region of the ionosphere, lying between  $\sim 60$  and 90 km. Typical profiles of electron density and identification of the various altitude ranges are given in Figure 1.1.

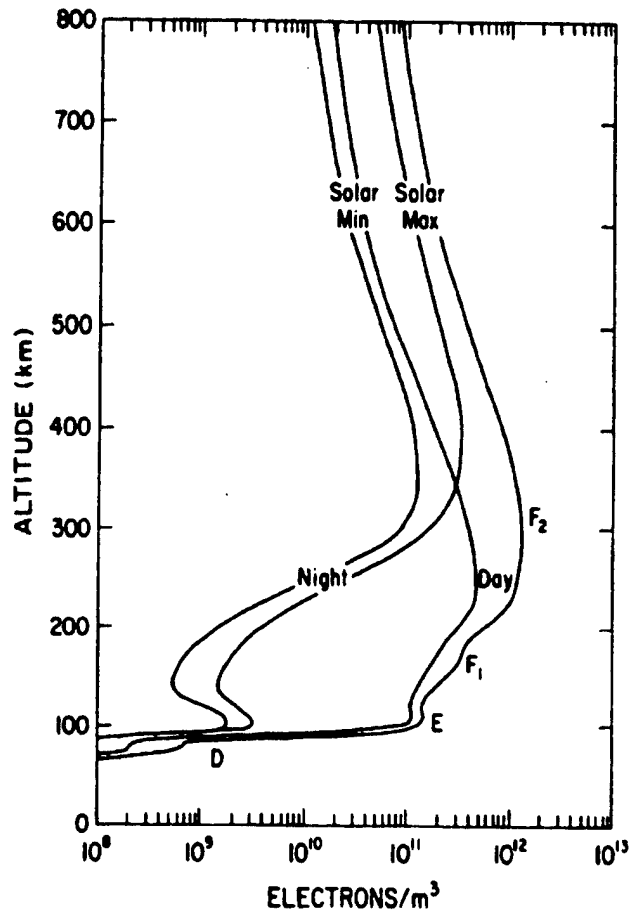


Figure 1.1: Typical midlatitude ionospheric electron density profile for sunspot maximum and minimum conditions during day-time and night-time. The different altitude regions in the ionosphere are labelled with  $D$ ,  $E$ ,  $F_1$ , and  $F_2$  [Richmond, 1987].

## 1.2 The Earth-Ionosphere Waveguide

One of the properties of electromagnetic waves is that they reflect from conducting boundaries and can thus be channelled or guided between such boundaries. The surface of the Earth is a moderately good conductor of electricity, and can reflect radio signals in the lower frequency signal ranges, including VLF waves [Davies, 1956; p. 45]. The ionosphere, on the other hand, is a complicated, highly lossy (conducting), and anisotropic medium and the  $D$  region is a good reflector of VLF waves, as mentioned above. The Earth and the ionosphere thus constitute the two boundaries of a waveguide within which VLF radio waves can propagate, commonly referred to as the *earth-ionosphere waveguide*.

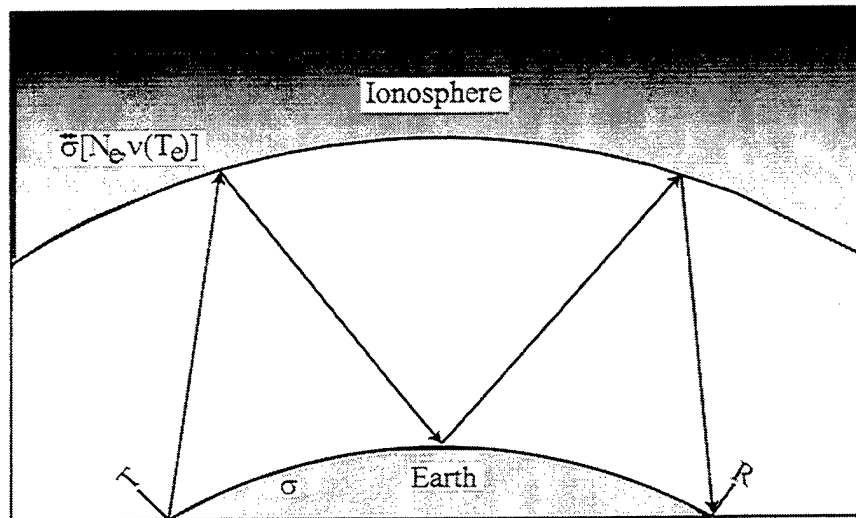


Figure 1.2: VLF signal propagation can be thought of as repeated reflection back and forth in the earth-ionosphere waveguide.

The propagation of VLF electromagnetic signals in the earth-ionosphere waveguide can be thought of in terms of signals reflecting back and forth between the Earth and ionosphere as shown in Figure 1.2, although analysis of this propagation can be more effectively described in terms of waveguide modes as described in Section 1.3. An electromagnetic wave totally reflects from a medium with varying dielectric properties at the point at which the refractive index is zero. For an isotropic lossless

plasma, this condition is realized when  $\omega \simeq \omega_p$ , where  $\omega_p$  is the plasma frequency of the medium given by  $\omega_p = 4\pi N_e q_e^2 / (\epsilon_0 m_e)$ , with  $N_e$  being the number density of electrons,  $q_e$  being the charge of an electron,  $\epsilon_0$  being the permittivity of free space, and  $m_e$  being the mass of an electron. However, in the VLF range, the absorption, reflection and transmission of a radio signal incident on the ionosphere depends on factors such as the wave frequency, the angle of incidence, the altitude profiles of electron and ion concentrations, the altitude profile of electron temperature and thus the rate at which these constituents collide with neutrals (i.e., the collision frequency), and the intensity and local orientation of the Earth's magnetic field. Due to the influence of the Earth's magnetic field, and the presence of absorption due to collisions, the refractive index does not reach zero at any  $D$  region altitude, so total reflection never occurs, but substantial partial reflection is possible. The region of the ionosphere where such partial reflection occurs can be thought of as a region where the refractive index changes very rapidly over distances comparable to a wavelength. When this occurs, the region acts like a sharp boundary between two media and reflection occurs. Quantitatively, the effective reflection height under nighttime conditions for VLF waves is determined by the condition [Wait and Spies, 1964]:

$$\omega \simeq \frac{\omega_p^2}{\nu} \simeq 2.5 \times 10^5 \text{ s}^{-1} \quad (1.1)$$

where  $\omega_p$  is the plasma frequency of the medium given by  $\omega_p = 4\pi N_e q_e^2 / (\epsilon_0 m_e)$ , with  $N_e$  being the number density of electrons,  $q_e$  being the charge of an electron,  $\epsilon_0$  being the permittivity of free space, and  $m_e$  being the mass of an electron;  $\omega$  is the wave frequency; and  $\nu$  is effective collision frequency of electrons with heavy particles.

The reflecting properties of the ionosphere are thus dependent on the number density of electrons,  $N_e$ , which varies with height above the Earth's surface (Figure 1.3) and which is particularly variable in the nighttime  $D$  region. A typical  $D$  region electron density profile is shown in Figure 1.3-a and in the critical altitude range of 60 to 90 km can be approximately described by a two-parameter exponential profile,

$$N_e(h) = 1.43 \times 10^{13} \exp [(\beta - 0.15)(h - h')] \quad (1.2)$$

with  $N_e$  in electrons/cm<sup>3</sup>,  $h'$  being the effective reflection height in km, and  $\beta$  in km<sup>-1</sup> determining the sharpness (slope) of the profile. Typical values for  $h'$  and  $\beta$  for nighttime conditions are  $h' \simeq 85$  km and  $\beta \simeq 0.5$  km<sup>-1</sup>, respectively [Wait and Spies, 1964]. The overall electron density profile shown in Figure 1.3-a has been used in a range of recent work involving modeling of VLF scattering from localized ionospheric disturbances [Inan et al., 1992; Rodriguez et al., 1994; Lev-Tov et al., 1995].

Absorption of radio waves in the ionosphere occurs primarily due to collisions between electrons and the neutral constituents of the atmosphere. Electrons move in response to the electromagnetic fields of the propagating waves and collide with the neutrals and ambient ions. These collisions transfer the propagating wave energy to thermal energy, and thus reduce the wave intensity. The lower regions of the ionosphere have the greatest density of neutrals and thus have the highest rate of occurrence of these collisions [Ratcliffe, 1972]. A typical collision frequency profile as a function of altitude is shown in Figure 1.3-b.

The average number of collisions  $\nu$  which an electron makes per unit time with the air molecules depends upon the number density of the molecules, and therefore is determined largely by the density and composition of the air and also to a lesser degree by the velocity distribution of the electrons [Budden, 1961]. Various collision frequency altitude profiles exist for electron-neutral particle collisions  $\nu_e(z)$  [Morfitt and Shellman, 1976]. An exponential profile as given in equation (1.3) is a typical example:

$$\nu_e(z) = 1.816 \times e^{-0.15z} \quad (1.3)$$

where  $\nu$  is in s<sup>-1</sup>, and  $z$  is in km. This profile is adopted as the ambient (unperturbed) collision frequency profile in this work.

### 1.3 VLF Propagation Models

Understanding and accurate modeling of the propagation of electromagnetic waves in the earth-ionosphere waveguide is essential for the purpose of this dissertation. Any

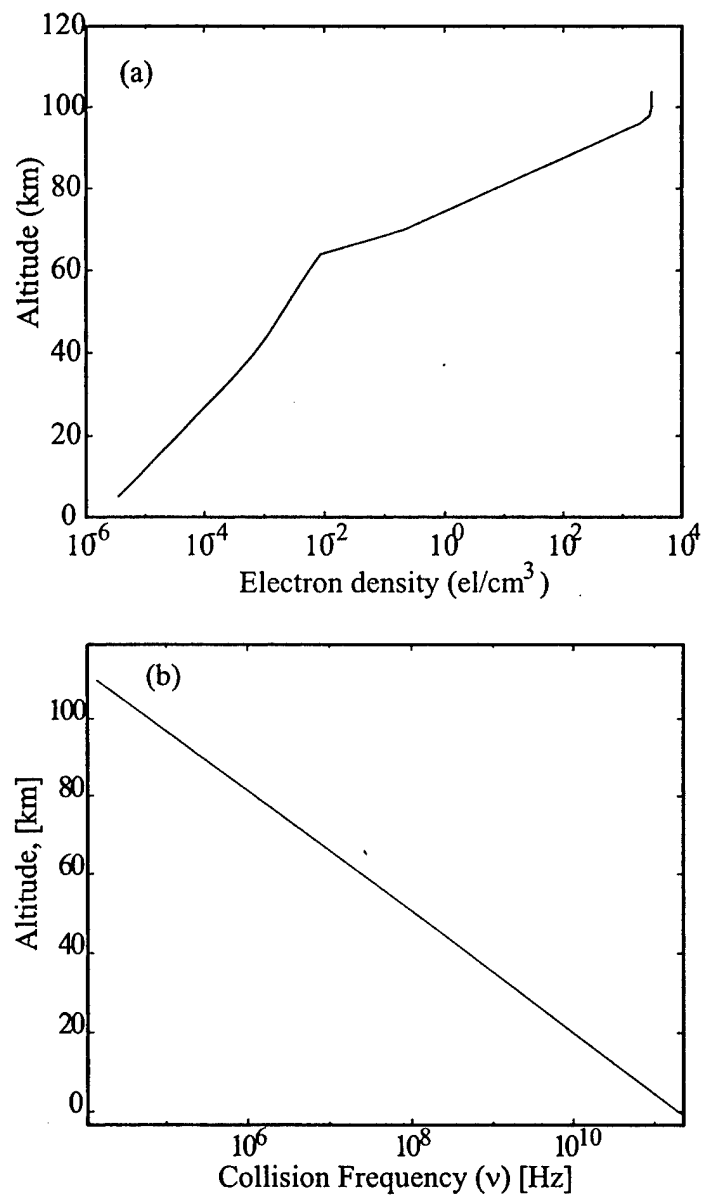


Figure 1.3: (a) Typical nighttime electron density as a function of altitude in the *D* region. (b) A typical model for the effective electron collision frequency versus altitude in the lower ionosphere.



model of electromagnetic wave propagation must be based on a simple set of formulas known as *Maxwell's equations*, as given below in differential form:

$$\nabla \times \vec{E} = -\frac{\partial \vec{B}}{\partial t} \quad (1.4)$$

$$\nabla \times \vec{H} = \vec{J} + \frac{\partial \vec{D}}{\partial t} \quad (1.5)$$

$$\nabla \cdot \vec{D} = \rho \quad (1.6)$$

$$\nabla \cdot \vec{B} = 0 \quad (1.7)$$

where

$\vec{E}$  is the total electric field,

$\vec{H}$  is the total magnetic field,

$\vec{D} = \epsilon \vec{E}$ ,

$\vec{B} = \mu \vec{H}$ ,

$\epsilon$  is the permittivity of the medium,

$\mu$  is the permeability of the medium,

$\rho$  is the volume charge density, and

$\vec{J}$  is the current density.

The electric and magnetic fields everywhere within the waveguide are obtained by solving these equations subject to boundary conditions. The radio receivers used to acquire the data utilized in this dissertation are designed to measure the electromagnetic fields at ground level.

There are mainly two methods for studying the propagation of VLF signals in the earth-ionosphere waveguide. The ray optics approach [Born and Wolf, 1965] is generally easier to visualize and analyze. This method simply traces the different

discrete ray paths that complete an integral number of reflections between the transmitter and the receiver (Figure 1.4). The number of complete reflections of the wave between the Earth and ionosphere before it reaches the receiver is called the order of the ray path. As the order of the ray path increases the angle of incidence on the ionosphere also increases. Since the absorption and transmission rates are higher for higher angles of incidence, the total effect of these signals at the receiver becomes less and less significant with increasing angle of incidence.

In ray theory few ray paths need to be calculated for very short (<500) km propagation paths. However when the propagation path is longer, there are more ray paths with low attenuation between the transmitter and receiver and calculations become tedious. In addition, for each separation distance between the transmitter and receiver the ray path geometry changes and all of the calculations must be repeated.

Electromagnetic waves propagating in the earth-ionosphere waveguide can also be represented in terms of a sum of an infinite series of discrete waveguide modes. The order of a waveguide mode simply corresponds to the number of maxima and minima in the transverse vertical field pattern. As the waveguide mode order increases, the spatial attenuation factor increases. Thus, the higher order modes do not propagate as far in the waveguide as the lower order modes.

Each waveguide mode can be represented in terms of a superposition of two uniform plane waves propagating by reflecting back and forth between the waveguide walls, being incident on the boundaries at a discrete angle  $\theta_n$  from the vertical [Inan and Inan, 1999; p. 269]. The discrete set of complex angles  $\theta_n$  for which this occurs are called the *eigenangles*, each of which corresponding to a single waveguide mode.

Accurate modeling of propagation in the earth-ionosphere waveguide is not complete if the influence of the Earth curvature is not accounted for. If this approach is used to yield an electric field  $\vec{E}$  and a magnetic field  $\vec{H}$  whose components are each functions of  $\Psi(r, \theta)$ , an infinite sum of rather complicated spherical wave functions [Wait, 1970; p. 157] results :

$$\Psi(r, \theta) = \sum_{n=1}^{\infty} D_q z_q(kr) P_q(-\cos \theta) \quad (1.8)$$

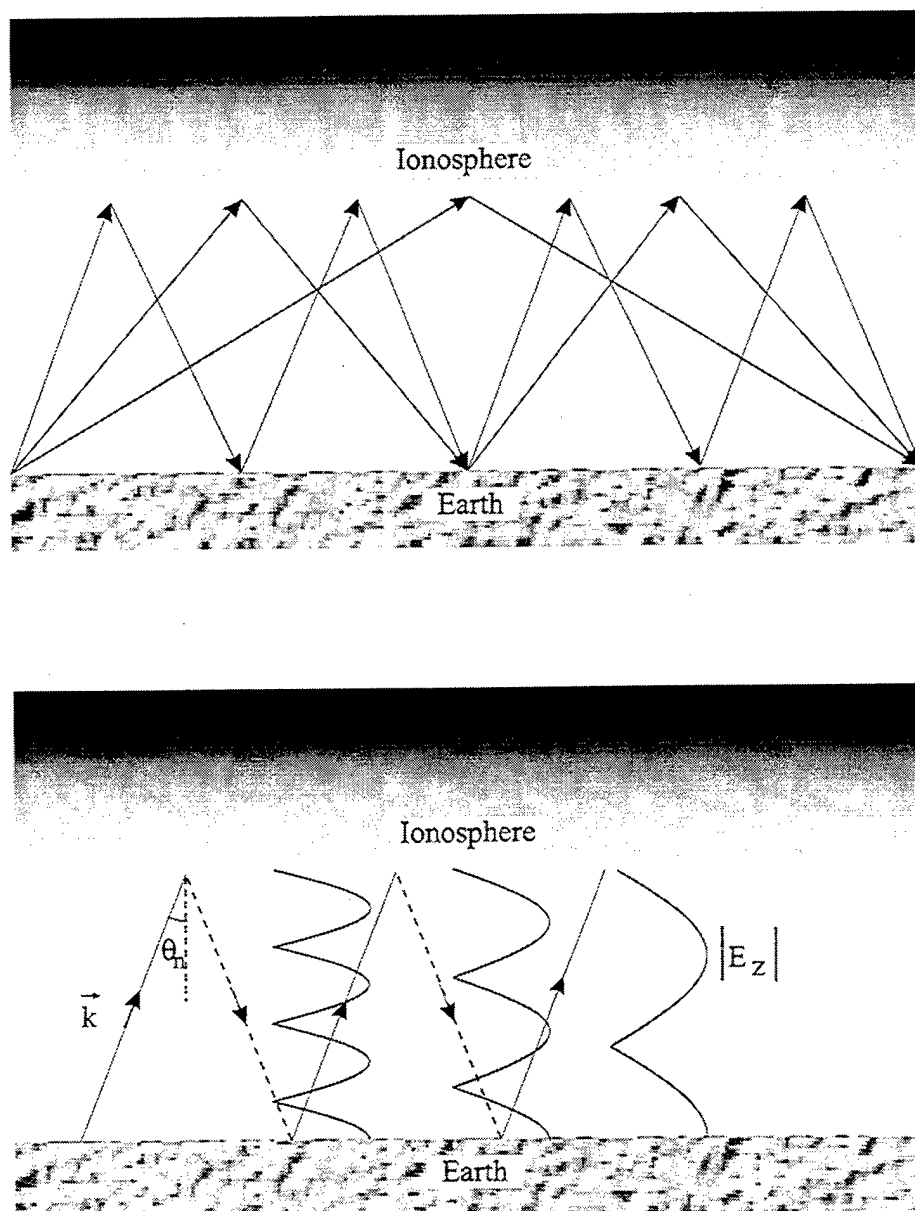


Figure 1.4: (a) **Ray Paths**. Possible discrete ray paths from a transmitter to a receiver. There are an integral number of reflections. Only the first three ray paths are indicated. For the  $n^{\text{th}}$  order ray path there are  $2^{n-1}$  reflection points in the ionosphere. (b) **Waveguide modes**. The vertical variation of the field amplitude of different modes are shown. The labels  $\vec{F}_0$  and  $\vec{F}_1$  are referred to later in connection with equation (1.12). Also shown are raypaths for component uniform plane waves (solid and dashed) the superposition of which can be used to represent the waveguide modes. Each mode corresponds to an incidence angle  $\theta_n$  for the component waves.

where

$r, \theta$  are spherical coordinates,

$n$  is the mode number,

$q$  is a complex number,

$D_\nu$  are the mode coefficients,

$z_\nu$  are Hankel functions of the first and second kind of order  $\nu$ ,

$k = \omega/c$ ,

$\omega = 2\pi f$ ,

$f$  is the wave frequency, and

$P_\nu$  are Legendre functions.

It was shown [Wait, 1970; p. 136] that under undisturbed ionospheric conditions, with the space between the Earth and the ionosphere taken to constitute a spherically concentric waveguide, and with homogeneous conditions along the entire path, the total electric field  $\vec{E}_{\text{total}}$  at a great circle path (GCP) distance  $d$  from the transmitter can be written as:

$$E_{\text{total}}(d) = \frac{1}{\sqrt{|\sin(d/R_E)|}} \sum_n^\infty A_n^{T,R} \exp[-ik_0 S_n d] \quad (1.9)$$

where

$n$  is the mode number,

$i = \sqrt{-1}$ ,

$\theta_n$  is the complex valued angle of incidence of each mode on the ionosphere, known as the eigenangle,

$S_n = \sin(\theta_n)$ , is the sine of the complex eigenangle  $\theta_n$ ,

$R_E$  is the radius of Earth,

$$A_n^{T,R} = K T_n R_n,$$

$$K = a\sqrt{Pf}, \text{ where}$$

$a$  is a constant coefficient,

$P$  is the radiated power,

$f$  is the signal frequency, and where

$$T_n = \sum_{j=1}^3 t_j \Lambda_{j,n}^T G_{j,n}^T(z) \quad (1.10)$$

$$R_n = \sum_{j=1}^3 r_j \Lambda_{j,n}^R G_{j,n}^R(z) \quad (1.11)$$

$j = 1, 2, 3$ , represent the three dimensions,  $x, y, z$  where the GCP lies along the  $x$  direction,

$t_j$  and  $r_j$  are factors for the orientation of the transmitter and the receiver antenna respectively,

$\Lambda_{j,n}^T$  and  $\Lambda_{j,n}^R$  are the initial excitation factors for each mode with respect to the transmitter and receiver antenna respectively,

$G_{j,n}^T(z)$  and  $G_{j,n}^R(z)$  are the *height gain factors* for each mode evaluated at the transmitter and receiver antenna respectively.

When the waveguide walls are not homogeneous but exhibit slowly varying conductivity, the angle of incidence  $\theta_n$  is a function of the propagation path and the  $\sin(\theta_n)$  term in equation (1.9) is replaced by  $\int^d \sin[\theta_n(x)] dx$ .

Any quantitative use of equation (1.9) requires that the complex eigenangles  $\theta_n$  are known. The eigenangles  $\theta_n$  can be determined using Budden's formulation of the

earth-ionosphere waveguide problem [Budden, 1961; p. 115-123]. In this formulation, a modal equation is developed in terms of reflection coefficients at the ionosphere and Earth, designated respectively as  $R^i(\theta_n)$  and  $R^g(\theta_n)$  where  $\theta_n$  is the angle of incidence of the waves on the ionosphere as above. The ionosphere is an anisotropic medium due to the existence of Earth's magnetic field, thus the reflection coefficient is actually a coefficient matrix. Since the medium is lossy, the reflection matrix is complex. In order to have the upgoing wave and the twice reflected wave interfere constructively, the twice reflected wave must have a total phase change of  $2\pi m$ . Thus if we let  $\vec{F}_0$  denote the upgoing wave and the  $\vec{F}_1$  denote the twice reflected wave (See Figure 1.4), the coherence or self-consistent mode condition is given in (1.12). The eigenangles are determined from this equation by setting  $|\vec{F}_1| = |\vec{F}_0|$ .

$$|\vec{F}_1| e^{-i2\pi m} = |\vec{F}_0| \bar{R}^g(\theta_n) \bar{R}^i(\theta_n) e^{-2ikh \sin \theta_n} \quad (1.12)$$

At the simplest level, we can approximate the earth-ionosphere waveguide by treating the ground as a perfect electric conductor and the ionosphere as a perfect magnetic conductor [Davies, 1965; p. 423]. In this case  $R^i = -1$ ,  $R^g = 1$ , and the resultant eigenangles obtained from equation (1.12) are shown in Figure 1.5.

## 1.4 Ionospheric Heating

The basic thrust of this dissertation is to develop and apply a new method of diagnostics of the lower ionosphere under conditions when it is modified by a powerful HF heater. The method utilized relies upon the measurement of the modulation pattern of the HF heater as it is imposed on a VLF radio beacon signal. The fundamental physical means of coupling of the HF and VLF signals is the nonlinear response of the ionosphere to the powerful HF heater wave. One of the first recognized manifestations of ionospheric heating by radio waves was the so-called '*Luxembourg effect*', involving such nonlinear coupling between two radio signals.

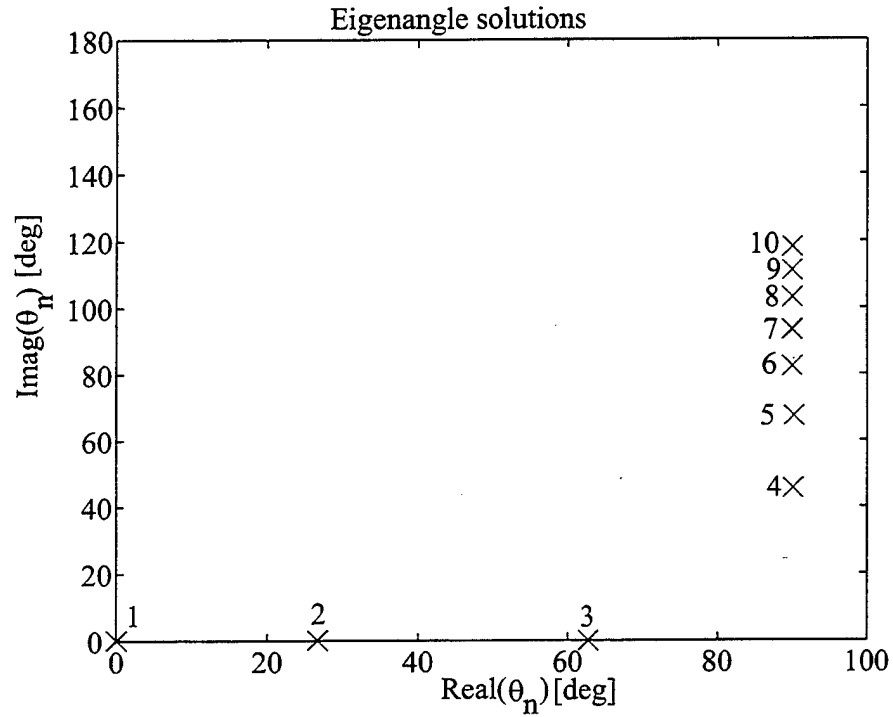


Figure 1.5: When the Earth surface is treated as a perfect electric conductor and the ionosphere is treated as a perfect magnetic conductor, we find  $R^g = 1$  and  $R^i = -1$ . Thus the resonance mode condition gives us the eigenangles in the figure for  $h = 85$  km and  $k = \omega/c = (2\pi)(25 \text{ kHz})/(3 \times 10^8 \text{ m/s}) = 5.2359 \times 10^{-4} \text{ m}^{-1}$ . The numbers refer to the mode numbers  $n$ .

### 1.4.1 The Luxembourg Effect

In 1933, it was discovered that the AM radio transmissions received in Eindhoven, Netherlands from a station in Beromunster, Switzerland, frequently had superimposed upon them the modulation of transmissions at a different radio frequency broadcast from Luxemburg [Tellegen, 1933]. This event, called the *Luxembourg effect* or *ionospheric cross-modulation* or *wave interaction*, was interpreted to be caused by a nonlinearity in the ionosphere. The geometry involved in the ionospheric cross modulation is illustrated in Figure 1.6.

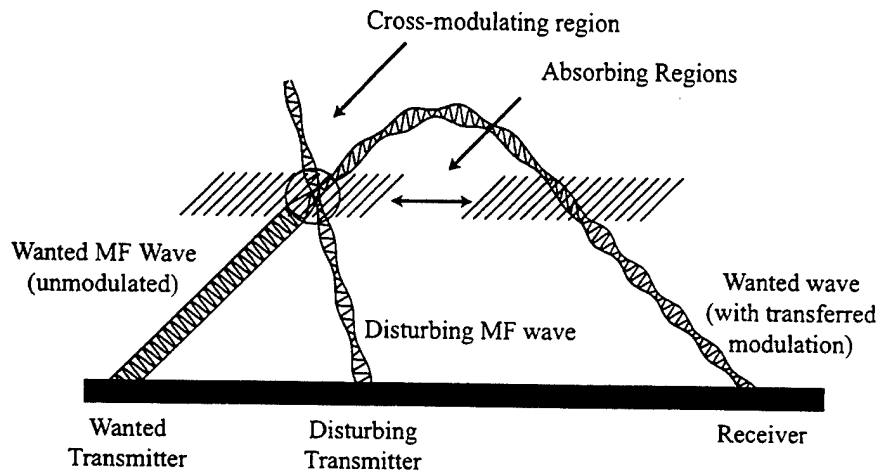


Figure 1.6: Geometry and nomenclature involved in ionospheric cross-modulation.

A receiver is tuned to receive a signal called the *wanted wave* (shown as initially unmodulated) from a *wanted transmitter*. The received signal shows modulation, called *transfer modulation*, imposed on the *wanted wave* in the *cross-modulating region* under the action of the *disturbing wave*. When a powerful disturbing wave is absorbed in the cross-modulation region, this absorbed energy goes partially into an increase in the mean energy of the electrons, increasing the electron collision frequency. The modulation of the disturbing wave therefore produces corresponding variations in the collision frequency of the region. Consequently, the absorption of the transmitted and wanted wave which propagates through this region exhibits the same time variation; i.e., the modulation is “transferred” from the disturbing wave to the wanted wave



[Bailey and Martyn, 1934].

The initial studies of ionospheric modification in the context of Luxembourg effect have evolved into a new field of high frequency (HF) ionospheric modification studies conducted with dedicated experimental heating transmitters. Powerful HF heating facilities have been constructed in the United States, Norway, and Russia for controlled ionospheric experiments [Wang and Brandt, 1990; and references therein]. Although these ionospheric heating experiments have a wide range of objectives, one of the documented effects of heating of the ionosphere by HF waves is the resultant enhancement of increasing the electron collision frequency in the  $D$  region by an order of magnitude over areas greater than  $300 \text{ km}^2$  [Stubbe and Kopka, 1979]. Such large changes in the  $D$  region in turn affect the propagation of VLF waves in earth-ionosphere waveguide as has been first observed by Barr *et al.* [1985] and as further discussed in the next subsection.

### 1.4.2 HF/VLF Coupling

The feasibility of measuring the amplitude and phase of the VLF waveguide signals scattered by artificially heated portions of the ionosphere has been demonstrated by different experiments [Barr *et al.*, 1985; Dowden *et al.*, 1991]. In this section we briefly describe an experiment which documented VLF signatures of ionospheric heating by the High Power Auroral Stimulation (HIPAS) HF facility (located near Fairbanks, Alaska) in 1992 [Bell *et al.*, 1995].

In the Fall 1992 and Spring 1993, an ionospheric modification campaign was carried out to determine the characteristics of the lower ionosphere during the operations of the HIPAS HF heater. The VLF data described in this section were acquired at Fort Yukon (FY), Alaska. The HIPAS facility operated with a total radiated power of 800 kW and an effective radiated power of 55 MW (ERP) at 2.85 MHz. The receiver at FY continuously monitored the signals from VLF transmitters NPM in Hawaii, NLK in Washington and Silver Creek (SC) in Nebraska. The configuration of the great circle paths between the transmitters and the receiver is shown in Figure 1.7. Table 1.1 shows latitude and longitude information for the VLF receiver site FY

	Latitude	Longitude
FY (VLF Receiver)	66.6°N	145.2°W
HIPAS (Heating Facility)	64.9°N	146.8°W

Table 1.1: Locations of VLF Receiver FY and heating facility HIPAS in Alaska.

Transmitter Name	Latitude	Longitude	Frequency (kHz)	Power (kW)
NLK (Jim Creek, Washington)	48° 12' N	121° 55' W	24.8	850
SC (Silver Creek, Nebraska)	41° 30' N	97° 36' N	48.5	60
NPM (Lualualei, Hawaii)	21° 25' N	158° 09' N	23.4	300

Table 1.2: List of VLF transmitters used during HIPAS 1992 Campaign

and the HIPAS observatory, Table 1.2 shows the list of VLF transmitters used in this experiment.

The great circle path of the NPM signal received at FY passes within 20 km of HIPAS. The distances between the NLK-FY and SC-FY great circle paths and the HIPAS facility were much larger and thus VLF signals from NLK and SC did not show any sign of ionospheric heating. But the amplitude and phase of the signal from the NPM transmitter observed in Fort Yukon exhibited a clear change with the same ON/OFF modulation pattern as that of the HIPAS HF transmissions. For 28 minutes, the HIPAS vertical beam (20° full beam width at half maximum power) was switched ON and OFF at 2 Hz. Figure 1.8 shows the results of this experiment. The upper panel shows the NPM amplitude during the 28 minutes the experiment was conducted. The middle left panel is the superposed epoch analysis which is obtained simply by dividing the data in the upper panel into 500 ms serial sections and subsequently summing and averaging to obtain the final single 500 ms result. The first 100 ms segment of each 500 ms period corresponds to the ON period of the HF heater. When the heater is OFF, the total signal received at FY is simply the unperturbed NPM signal which propagates directly to FY. However when the heater is ON, in addition to the direct signal, there is the signal scattered from the heated ionosphere over the HIPAS heater, resulting in an amplitude increase of about 0.18 dB in the total received signal. In other words, the 100 ms ON/400 ms OFF modulation of the HF heater is 'transferred' to the NPM-FY VLF signal, precisely

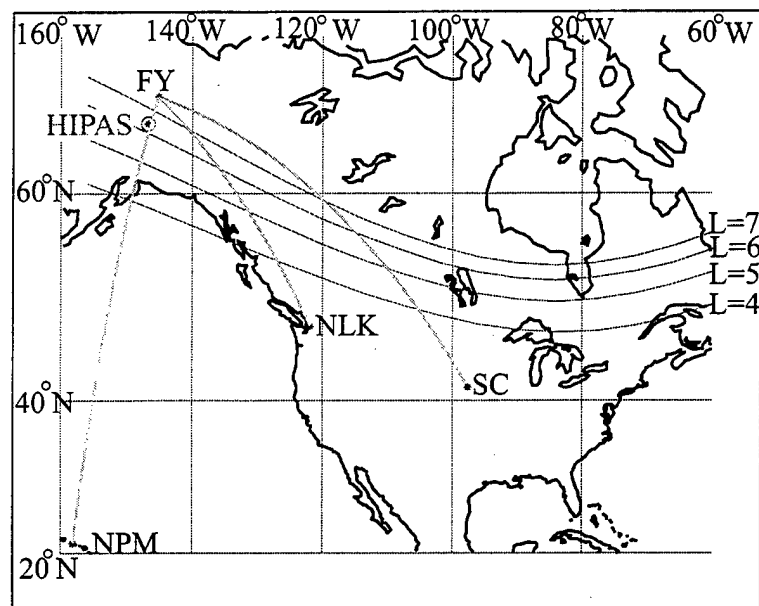


Figure 1.7: Configuration of the great circle paths between the three VLF transmitters and the observation site at Fort Yukon, Alaska

in the same manner as the classical cross-modulation problem depicted in Figure ??.

The lower left panel shows the spectral analysis of the raw data. Peaks at 2 Hz and its harmonics are clear indications of the VLF modulation resulting from the pulse modulation of the HF heater signal. The panels on the right show the superposed epoch analysis of the measured phase of NPM signal and the spectral analysis of the raw phase data. The HF heating modulation is clearly evident on the NPM signal phase, with the phase change being  $\sim 4.5^\circ$ .

### 1.4.3 VLF Diagnostics of the Modified $D$ region

The Stanford VLF observations during the 1992 HIPAS campaign were conducted as part of the development/testing of a new diagnostic technique whereby the phase and amplitude changes of the VLF signals propagating nearby a heated ionospheric region are used to determine the collision frequency profile in the heated region. This technique was developed as a diagnostic tool for the new HAARP (HF Active Auroral Research Program) ionospheric heating facility, now operational in Alaska (Chapter 5). In this subsection we briefly describe the formulation of this new diagnostic tool, the various components of which constitute the core of this Ph.D. dissertation.

The measurement of any given VLF signal phase and amplitude changes produced by a HF heater provides data from which we can characterize the electron collision frequency profile with two free parameters. The measurement of the phase and amplitude changes in  $N$  distinct signals (at  $N$  different frequencies) thus provides data from which we can characterize this profile with  $2N$  free parameters. Due to practical considerations (e.g., availability of VLF transmitters and field deployment sites), the Stanford VLF  $D$  region diagnostic technique is based on the use of 3 distinct VLF signals, as described in the next paragraph.

Amplitude and phase changes of three different VLF signals received at three different sites are measured with high time resolution both before, during and after episodes of HF heating with prescribed modulation patterns. The transferred modulation on the subionospheric VLF signals are then extracted via analysis (similar to that shown in Figure 1.8) and are interpreted in terms of altitude profiles of  $D$

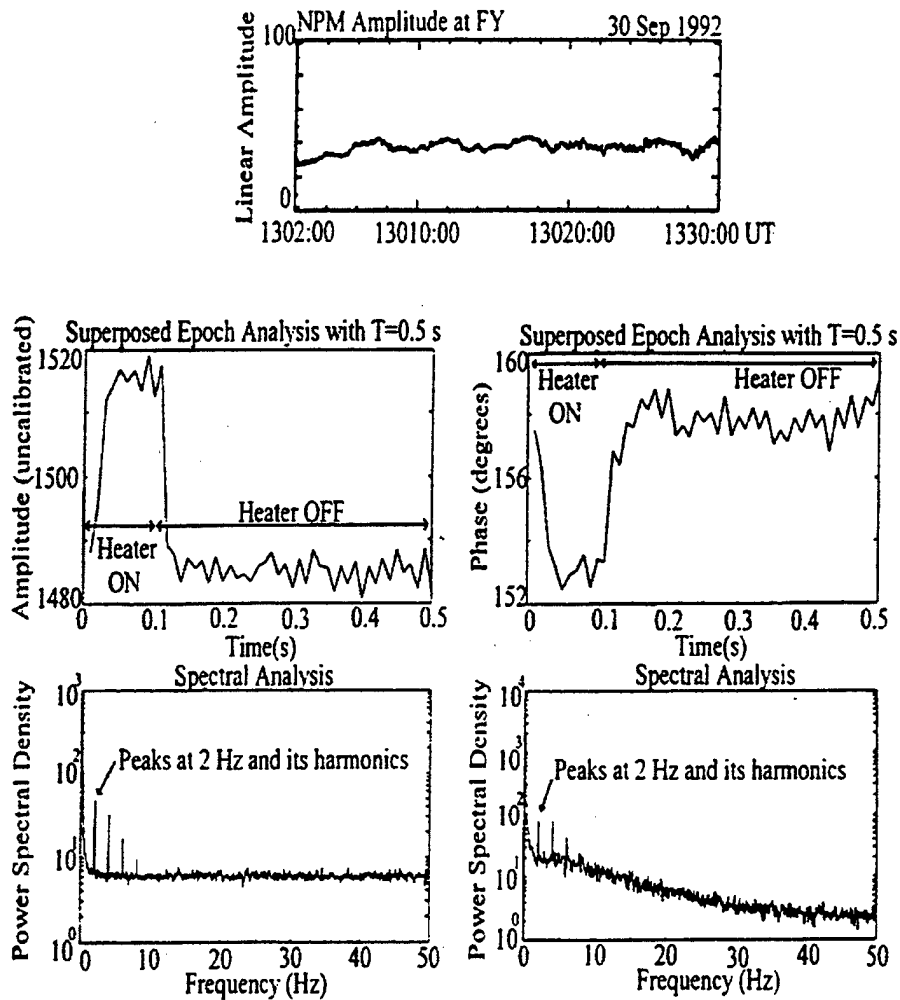


Figure 1.8: (a) Raw NPM amplitude data recorded at FY while the HIPAS receiver was ON for 100 ms and OFF for 400 ms (2Hz periodicity), repeated for 28 min. (b) Superposed epoch analysis (with  $T=500$  ms) of the raw data set from (a). (c) Spectral analysis of the raw data set from (a). (d) Superposed epoch analysis with  $T=500$  ms of raw NPM phase data at FY during which the HIPAS HF heater was on for 100 ms and off for 400 ms (2 Hz periodicity) (e) Spectral analysis of the same raw data [Bell et al., 1995].

region electron collision frequency, or equivalently, electron temperature profiles.

This VLF long path diagnostic technique relies heavily on sophisticated models of VLF propagation and scattering, as indicated in Figure 1.9. The propagation of the VLF signal in the earth-ionosphere waveguide along the great circle path from the VLF transmitter to the receiver, and its scattering from the heated ionospheric patch, are modeled with the Long Wave Propagation Capability (LWPC) code [Ferguson and Snyder, 1987] and a three dimensional version of this code recently developed at Stanford, both described in detail in Chapter 2. The use of the VLF propagation and scattering codes for extraction of  $D$  region electron collision frequency and temperature profiles from VLF amplitude and phase data from multiple sites as shown in Figure 1.9 constitutes the new VLF  $D$  region diagnostic tool which is the subject of this dissertation.

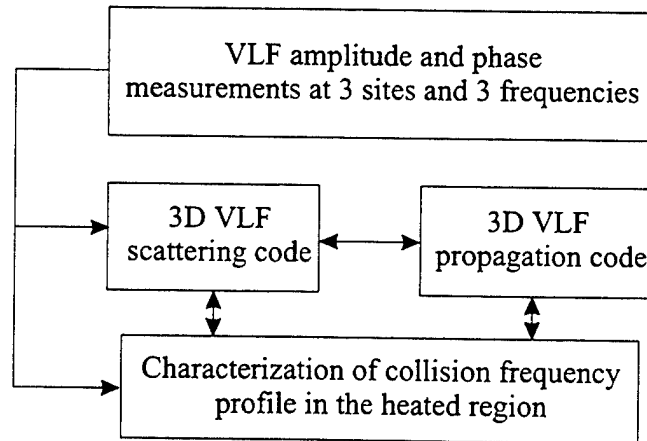


Figure 1.9: Development of algorithm for extraction of  $D$  region electron collision frequency profile from VLF amplitude and phase changes measured at three different sites.

## 1.5 Contributions

The contributions of this dissertations are as follows :

- Interpretation of an observed correlation between relativistic electron precipitation enhancement events and subionospheric VLF signal amplitude in subauroral regions. VLF signal amplitudes exhibit  $> 10$  dB changes, exhibiting the same 27 day cycle and 2–3 day rise and fall time pattern as relativistic electron enhancement events recorded by GOES 7 and SAMPEX. This new observation [Demirkol *et al.*, 1999] indicates that the nighttime lower ionospheric electron density at subauroral latitudes is detectably affected by 27-day periodicity in solar rotation. The experimental data and its interpretation is presented in Chapter 3.
- Development of a method to determine the ambient electron density profile over a subauroral propagation path based on the fact that  $D$  region electron density profile is strongly modulated by precipitation enhancement events. This new method is described in Section 3.2.
- Development of a new inversion algorithm to determine the altitude profile of electron collision frequency (or temperature) within localized disturbances by using the measured amplitude and phase of three different VLF signals at three separate receiving sites. Localized disturbances are routinely produced by powerful HF transmitting facilities such as the High Power Auroral Stimulation (HIPAS) facility [Bell *et al.*, 1995] and the High frequency Active Auroral Research Program (HAARP) and also by lightning discharges [Inan *et al.*, 1996]. The new optimization algorithm developed here is primarily based on the recursive usage of the three dimensional version [Poulsen *et al.*, 1993] of the Long Wave Propagation Capability (LWPC) code used to model the subionospheric propagation and scattering of VLF signals in the earth-ionosphere waveguide in the presence of ionospheric disturbances. The new inversion algorithm is described and documented in Chapter 4.
- Application of the inversion techniques to experimental data acquired during the March 1999 HAARP campaign. The new inversion technique is used to extract the first measurements of the effective electron collision frequency in a heated region, as described in Chapter 5.

## Chapter 2

# VLF Signal Propagation Models

VLF waves at large distances ( $> \sim 1000$  km) from their source can be conveniently represented in terms of a summation of multiple waveguide modes, each propagating with a different complex eigenangle in the waveguide formed by the conducting curved Earth and the anisotropic, imperfectly conducting curved ionosphere with a dipping magnetic field. In this chapter, we describe the tools we use to quantitatively analyze the propagation and scattering of such signals and also present an analysis of a single waveguide mode case.

### 2.1 Long Wave Propagation Capability

The Long Wave Propagation Capability (LWPC) code, developed over many years by the Naval Oceans System Center [Ferguson and Snyder, 1987], and now widely used, is a combination of FORTRAN programs which enable the user to model the propagation of VLF signals in two dimensions along the Great Circle Path (GCP) between a transmitter and a receiver. Following is a brief description of these programs together with their input and output specifications.

Given the required parameters, the electric field along a propagation path can be calculated using the straightforward two dimensional method given by equation (1.9). In this case the dimensions are  $x$  and  $z$ , where  $x$  is along the great circle path between the transmitter and the receiver, and  $z$  is the altitude, and all of the



properties of the ionosphere and ground are assumed to be constant in the  $y$  direction. Figure 2.1 shows the geometry for the 2D VLF propagation problem.

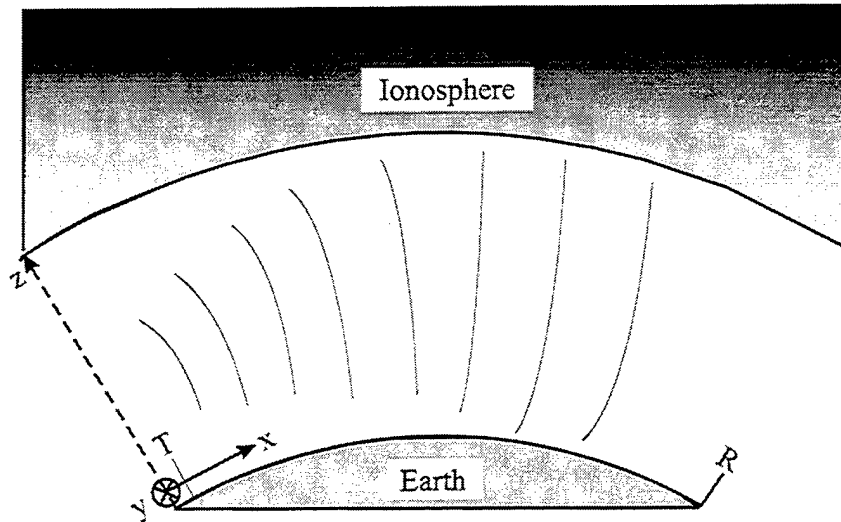


Figure 2.1: The geometry of the 2D VLF signal propagation problem. The properties of the ionosphere and the Earth are assumed to be constant in the  $y$  direction.

The customary means for entering input parameters into the LWPC code is in terms of a model file which contains all of the required parameters for different components of the LWPC. This model file is generally named **TTTRR.lwpc** where TTT stands for the three letters describing the transmitter, and RR stands for the two letters describing the receiver. After the input file is prepared, a script named **model\_2d** is used to run the different FORTRAN programs described below in the required order. Figure 2.2 shows the flow of this process.

Some of the parameters listed in the **TTTRR.lwpc** file and used by different components of LWPC are listed below :

$f$ , frequency in kHz (default = 23.4),

$P$ , radiated power in kW (default = 1),

$T_{long}, T_{lat}$ , transmitter coordinates in degrees west and north (default = 158.15/21.41),

- $R_{long}, R_{lat}$ , receiver coordinates in degrees west and north (default = 0/0),
- $d\rho$  distance increment in km (default = 5),
- $\rho_{max}$ , maximum distance in km (default = 10000),
- $year, month, day$ , for terminator calculations (default = 1984/03/15),
- $gmt$  Greenwich time in hours (default = -24),
- $nrseg$  number of segments in terminator boundary (default = 5),
- $range_r, range_i$ , range of real and imaginary parts of the eigenangles to be found (default = 60.0/90.0, 0.0/-7.0),
- $\alpha_{max}$  maximum attenuation rate in dB/Mm used by MODESRCH/MODEFNDR to identify a finite number of most significant modes, (default = 200),
- $\chi$  terminator boundary in deg of solar zenith angle (default = 90),
- $p_{cap}$  polar cap boundary in deg of magnetic dip angle (default = 70),
- $R_{comp}$ , received electric field component, =1 if  $z$ , =2 if  $y$  (default = 1),
- $R_{alt}, T_{alt}$  receiving and transmitting platform altitude in km (default = 0.0),
- $\gamma$ , inclination of the transmitting antenna with respect to the vertical in degrees (default = 0.0),
- $\theta$ , orientation of the transmitting antenna's projection in the horizontal plane with respect to the direction of propagation in degrees (default = 0.0), and
- $Topht$ , height of the bottom of the ionosphere in km (default = 90).

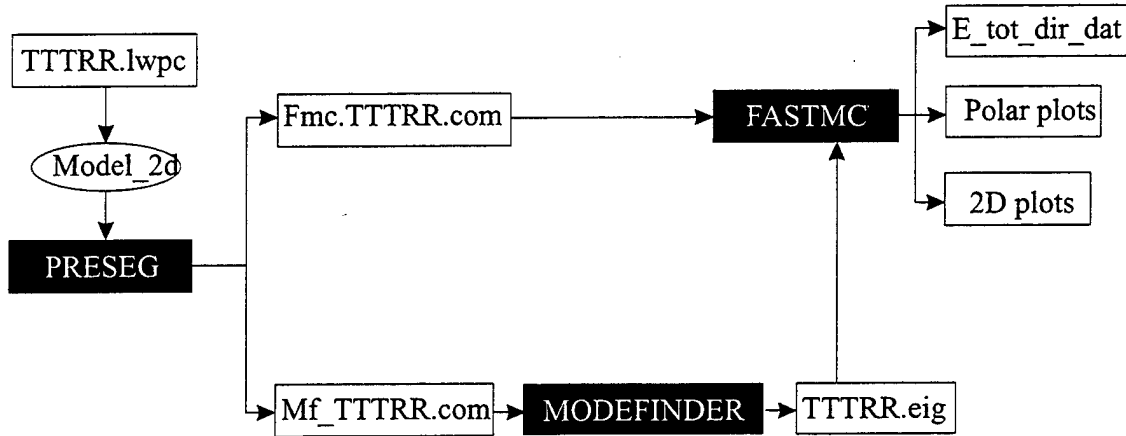


Figure 2.2: Flow diagram for the LWPC code for 2D modeling of VLF signal propagation in the earth-ionosphere waveguide. **TTTRR.lwpc** is the input model file which contains the required parameters for the three FORTRAN programs, namely PRESEG, MODEFINDER and FASTMC, described in the text.

### 2.1.1 PRESEG

PRESEG is a FORTRAN program which uses the **TTTRR.lwpc** model file and segments the propagation path between the transmitter and the receiver based on ionosphere, ground, and magnetic field changes [Pappert and Snyder, 1972a; Wait and Spies, 1968]. It creates output files **mf\_TTTRR.com** and **fmc\_TTTRR.com** which contain this segmentation information and which are used by MODEFINDER and FASTMC respectively. PRESEG segments the path according to the directions given in the **TTTRR.lwpc** file as well as automatic segmentation rules, such as the known (as derived from a previously input conductivity map of the Earth) conductivity changes of the Earth [Hauser et al., 1969] as the signal propagates along the great circle path, crossing boundaries such as those between ground and sea, rocky versus marshy soil, as well as different ionospheric regions, such as low or mid latitudes, auroral regions, etc..

### 2.1.2 MODEFINDER

The solutions to the mode equation (2.8) in general cannot be expressed in closed form for realistic ionospheric conditions. For this purpose, a computer program called MODEFINDER is employed [Morfitt and Shellman, 1976; Ferguson and Snyder, 1987]. This program was developed initially by the Naval Ocean Systems Center in order to numerically determine the values of the sine of the complex eigenangle,  $S_n$ , as defined in connection with equation (1.9). It is designed to obtain these mode constants rapidly and accurately. The MODEFINDER program obtains the full-wave solutions of the modal equations for  $|\vec{F}_1(\theta)| = |\vec{F}_0|$  in terms of the eigenangles.

Two other input parameters that are included in the **TTTRR.lwpc** model file are the altitude profiles of the electron density and collision frequency. The MODEFINDER program uses this information and first modifies the density profile in order to eliminate those heights for which the electron densities have negligible effects on the modal solutions. The modal solutions of equation (1.12) are determined within a bounded region of the complex  $\theta$  plane determined by  $range_r$ ,  $range_i$ , and  $\alpha_{max}$ . In the process of determining the reflection coefficients of the ionosphere, MODEFINDER calculates an effective reflection height. From the resultant values of the reflection coefficient matrix elements and the modal eigenangle solutions, the attenuation rate, phase velocity, initial excitation, height gain factors and the polarization mixing ratios for each mode are determined [Morfitt and Shellman, 1976].

### 2.1.3 FASTMC

In order to calculate the mode conversion coefficient matrices at the different slabs created by PRESEG, a FORTRAN program called FASTMC is used [Pappert and Shockey, 1972; Pappert and Snyder, 1972b]. FASTMC is a simplified version of a more fundamental FORTRAN program called FULLMC. FASTMC uses a number of approximations in order to reduce the execution time of FULLMC [Ferguson and Snyder, 1980; Poulsen, 1991] and is exclusively used in this thesis for the calculation of mode conversion matrices.

### 2.1.4 Example 2D simulation

Since the LWPC code is capable of accounting for mode conversion effects at the interface between two slabs having one or more different geophysical parameters, we can model ionospheric disturbances which lie on the great circle propagation path of the VLF signal propagating from a transmitter to a receiver, as long as such disturbances can be represented as infinite strips perpendicular to the path and with no variation in the  $y$  direction. Thus, it is possible to study the effects of a disturbance on the VLF amplitude and phase as a function, for example, of the width of the disturbance along the  $x$  axis. Conversely, it should in principle be possible to solve the inverse problem, i.e., to determine the width (along the path) of a disturbance from measurements of the associated amplitude and phase. In Chapter 3, we employ such an inversion method to determine the ambient electron density profile.

As an example of the use of LWPC for 2D modeling of VLF propagation, we consider the propagation path between the NLK (24.8 kHz) transmitter in Washington (121.9°W, 48.20°N) to Fort Yukon (FY), Alaska (145.2°W, 66.6°N). We also assume the hypothetical presence of an ionospheric disturbance along the propagation path. The **NLKFY.lwpc** model file used for this case is:

```
/export/home/demirkol/Programs/nlkfy
2
/export/home/demirkol/profiles/densprofs/electr.profile2
/export/home/demirkol/profiles/densprofs/sp_relative_profs/d3_11.dat
0
NLKF
NLKFY
&datum
freq=24.8 trlat=48.200 trlong=121.910
rclat=66.560 rclong=145.218
max_alt=110.0
ibound0 = 1400 1900
insptype0=(1,0) (2,0) (1,0)
&end
```

The first line indicates the path where all of the simulation files should be read from and written to. The second line is the number of different electron density profiles (in this case 2) that will be used in the propagation path of the VLF signal. Next the locations of these tabular electron density profile files are given. Alternatively, it is possible to use an exponential profile similar to that in equation (1.2). The number 0 on the next line corresponds to the number of collision frequency profile to be used in the calculations, in this case meaning that an ambient profile should be employed in this specific simulation. The next few lines specify the frequency of the VLF signal as well as transmitter and receiver locations. IBOUND0 corresponds to the great circle distances (from the transmitter) in km where a user forced boundary exists, in this case representing the beginning and end of a disturbance between 1400 to 1900 km. INSPHYPE0 corresponds to different combinations of (electron density, collision frequency) profiles that will be used in each of these segments. In this case, the profile combination (1,0) is used in the region between the transmitter and the 1400<sup>th</sup> km along the propagation path, consisting of the first (1) electron density profile listed in the model file and the ambient (0) collision frequency profile. Between the 1400<sup>th</sup> and 1900<sup>th</sup> km the second (2) electron density profile is used together with the ambient (0) collision frequency profile corresponding to (2,0). After the second boundary, the combination is again (1,0). The geometry of the problem is shown in Figure 2.3.

The eigenangle solutions in the first segment of the propagation path are shown in Figure 2.4. The field amplitude and phase of the total VLF signal at different points along the GCP between NLK and FY are shown in Figure 2.5. The characteristic deep nulls along the propagation path occurs as a result of destructive interference between different waveguide modes, each propagating with slightly different phase and velocity and different attenuation rates. At large distances, these large variations in the total field intensity are reduced, since most of the modes are attenuated out, and the signal is constituted by only a few modes.

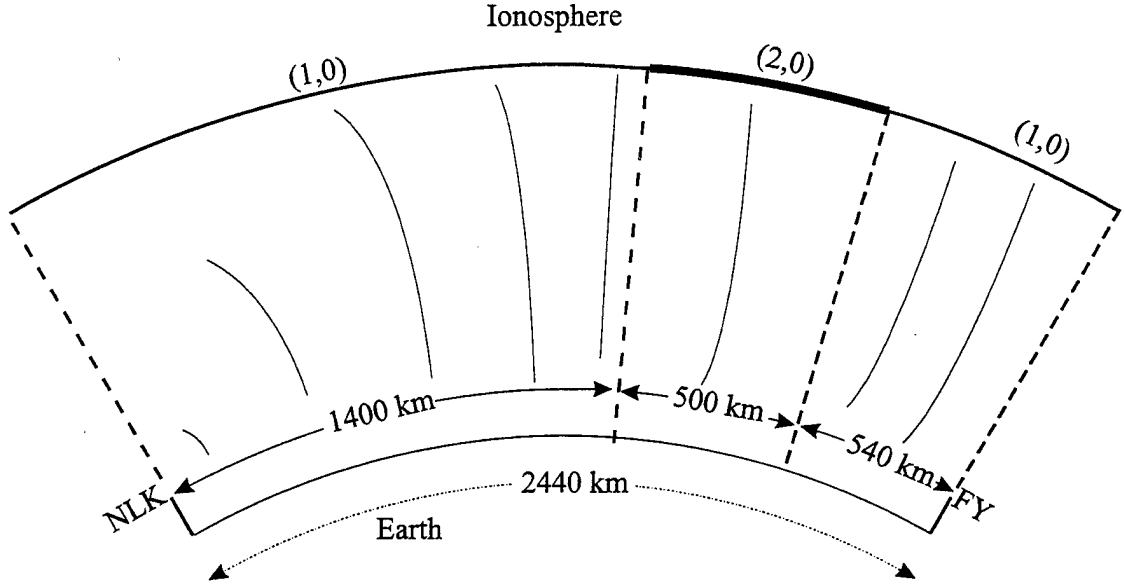


Figure 2.3: NLK-FY path for the 2D simulation of VLF signal propagation.

## 2.2 3D Numerical Modeling

A 2D model is necessarily limited in application since most realistic ionospheric disturbances encountered in practice have a three dimensional structure. Examples of 3D ionospheric disturbances are those produced by lightning discharges [Rodriguez *et al.*, 1992] and powerful HF ionospheric heaters. A 3D model is needed for accurate description of VLF propagation and scattering in the presence of such disturbances. Such a 3D model was developed at Stanford University [Poulsen, 1991] and have been applied for interpretation of VLF signal amplitude and phase changes observed in association with lightning discharges [Poulsen *et al.* 1993; Lev-Tov *et al.*, 1995; Inan *et al.*, 1996]. The geometry of the 3D problem is shown in Figure 2.6. The 3D nature of the model allows for ionospheric parameter variations both in the direction of the GCP ( $x$  direction) and the direction transverse to it ( $y$  direction).

In the 3D case the total electric field a distance  $d$  from the transmitter as given for 2D by equation (1.9) changes to equation (2.1) given below [Wait, 1964] :

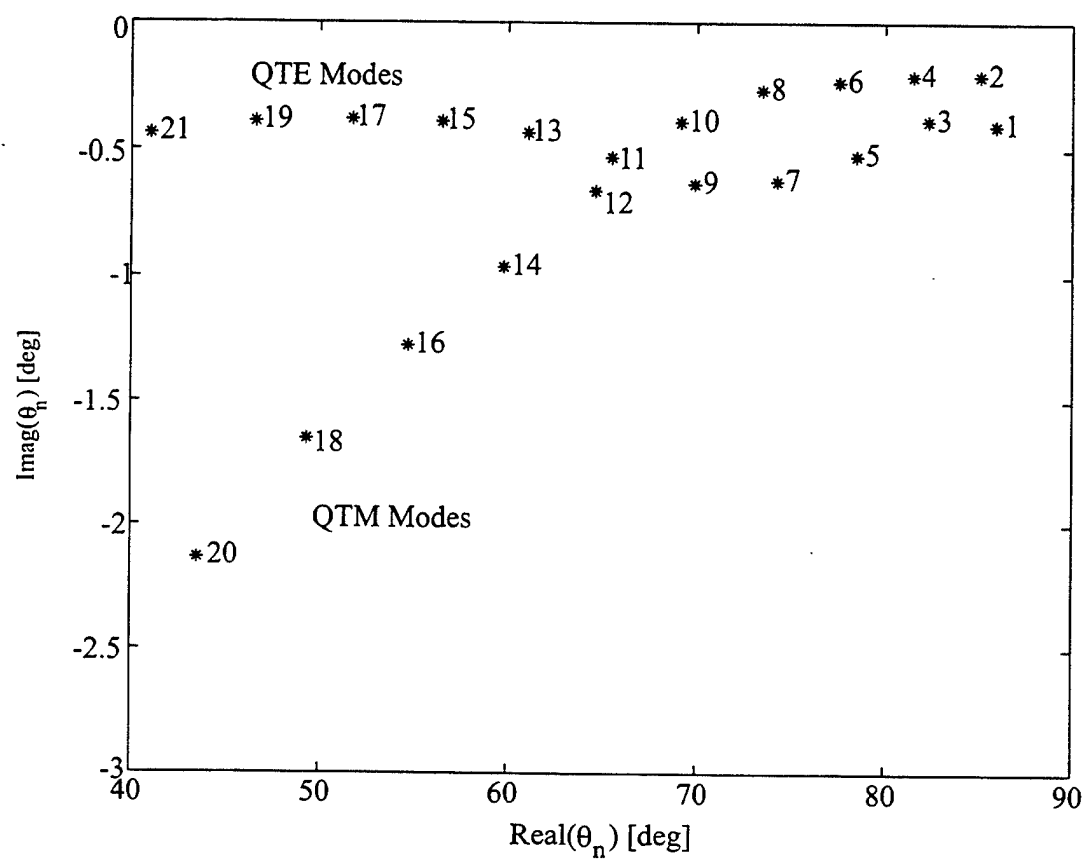


Figure 2.4: Eigenangle solutions found by MODEFINDER for the NLK signal propagating to FY for the first segment of the path. Each point corresponds to a different mode as indicated.



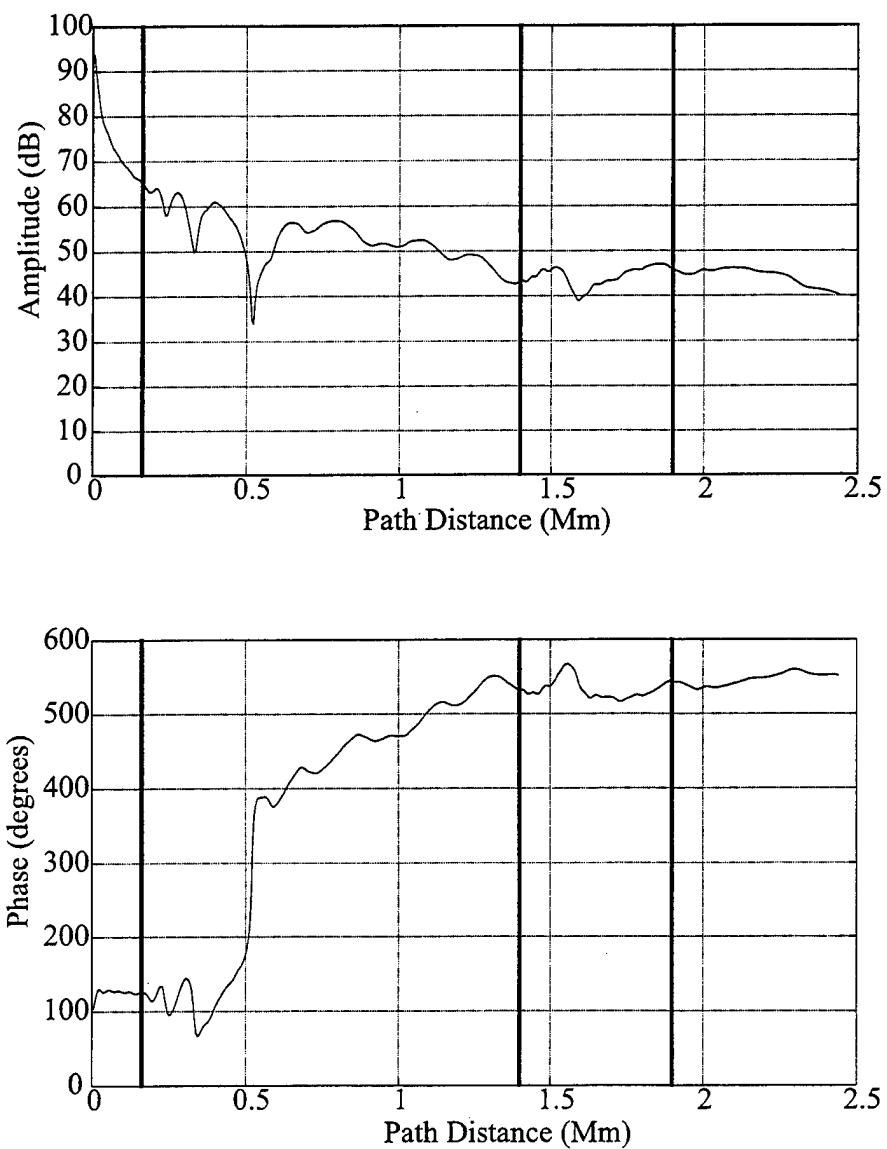


Figure 2.5: The amplitude and phase of the VLF signal changes as it propagates in the earth-ionosphere waveguide. The solid lines correspond to the forced and natural boundaries on the propagation path as segmented by PRESEG.

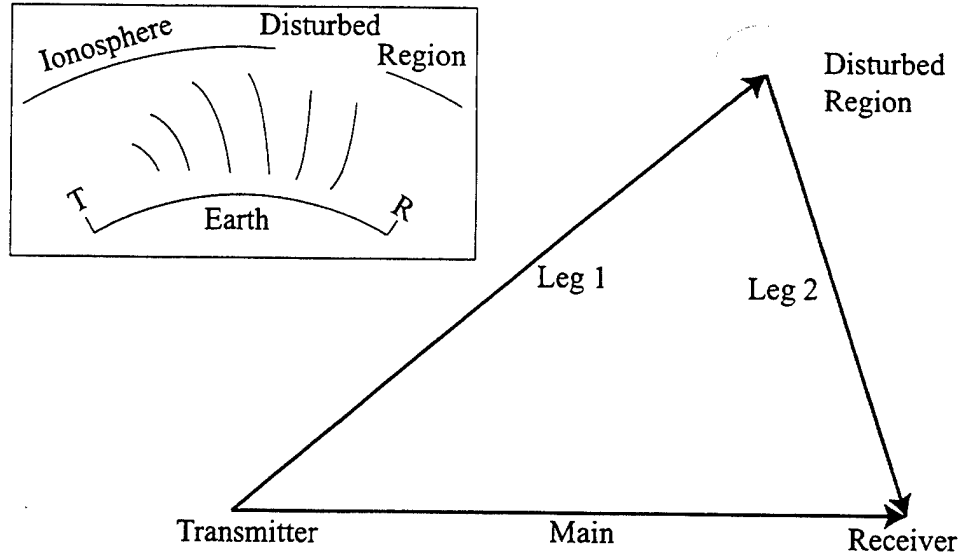


Figure 2.6: Illustration of the 3D modeling of the VLF wave propagation in the presence of a localized disturbance. The main leg corresponds to the GCP between the transmitter and the receiver. The signal at the receiver consists of a vector sum of the direct signal along the Main Path and the scattered signal arriving from Leg 2.

$$E_{\text{total}}(d) \simeq \sqrt{\frac{d}{R_E |\sin(d/R_E)|}} \sum_n^{\infty} A_n^{T,R} \frac{1}{\sqrt{d/R_E}} \exp \left[ -ik_0 \int_C S_n(x', y') ds \right] \quad (2.1)$$

where the integration contour is along the path of minimum total phase between the transmitter and the observation point located at distance  $d$ . However this equation is only an approximation, assuming slow variation of the properties in the  $x$  and  $y$  direction. A more detailed analysis of this problem is given elsewhere [Poulsen, 1991].

Based on the formulation described in Poulsen [1991] and Poulsen *et al.* [1993], the 3D VLF code consists of the LWPC code combined with two other programs called SCATTER and SUMOUT, in order to simulate the propagation of VLF signals in the presence of localized lower ionospheric disturbances. A schematic flow graph of the 3D simulation code is given in Figure 2.7, where SCATTER and SUMOUT are briefly described below.

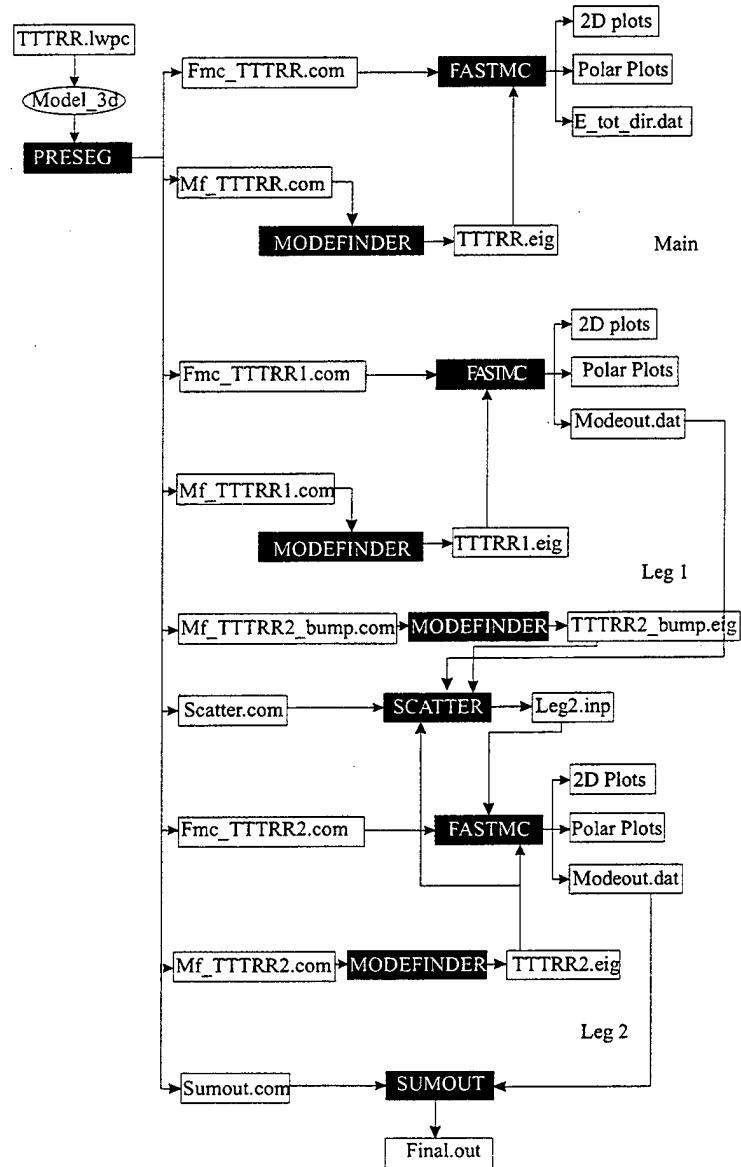


Figure 2.7: Flow of the LWPC code for 3D simulation of VLF signal propagation in the earth-ionosphere waveguide. In this model, VLF signal propagation is simulated on two different legs denoted as Main and Leg 1 in Figure 2.6. The scattered field is calculated by the FORTRAN program SCATTER and another simulation is carried out for the propagation of this scattered field to the receiver, over the path denoted as Leg 2. Finally SUMOUT calculates the total electric field that is received.

### 2.2.1 SCATTER

The program SCATTER calculates the theoretical value of the change in the field measured at the receiver due to a cylindrically symmetric perturbation normalized by the theoretical value of the field that would have been received had there been no perturbation. SCATTER gives both the real and imaginary parts of this change in the field. A few of the important parameters in this program are :

$\theta_0$  the background complex eigenangle value,

$\theta_{peak}$  the eigenangle values at the center, or peak of the disturbance,

*spotsizes*, the size of the disturbed region in the ionosphere,

$x_0, y_0$  the location of the spot with respect to the great circle path of VLF signal propagation.

This program uses a specified lateral profile (e.g., a Gaussian distribution) as the horizontal roll-off function for the change in S value of the perturbation back to the background value as a function of distance from the center of the perturbation.

### 2.2.2 SUMOUT

The total field measured at the receiver is a sum of the field from the main leg, which is the direct propagation of the signal along the great circle path and the scattered field from the disturbance arriving over Leg 2. SUMOUT implements the vectorial addition of two fields.

## 2.3 Analysis of a Single Mode Case

The subject of this dissertation is to utilize the tools just described in order to measure the electron collision frequency profile within a heated ionospheric patch by exploiting the sensitive dependence of the VLF signal amplitude and phase on ionospheric properties such as electron density and temperature. In this section, we illustrate the

determination of the collision frequency profile for the simplest possible case in which the VLF signal is constituted by a single waveguide mode. This case can be treated analytically and its analysis illustrates the difficulty involved in the more general multimode case.

The individual modes may be identified in terms of the number of minima and maxima that the field quantities exhibit as a function of altitude (Figure 1.4-b) or in terms of the discrete eigenangles for which the mode fields can be coherently decomposed into a sum of two uniform plane waves which are in phase. The complex eigenangles may be obtained through a *full wave* solution of Maxwell's equations which yields a set of reflection coefficients satisfying the condition:

$$R^{(g)}(\theta) R^{(i)}(\theta) \exp(-2ikh \sin \theta) = 1 \quad (2.2)$$

which is simply obtained from equation (1.12) by setting  $|\vec{F}_1| = |\vec{F}_0|$ .

In general  $R^{(i)}$  is a matrix because of the anisotropic characteristic of the ionospheric plasma. However during daytime when the VLF reflection height approaches 70 km in altitude, the effects of the Earth's magnetic field are reduced and the ionosphere at this altitude can be considered isotropic. In this case  $R^{(i)}$  is a scalar.

In general the reflection coefficient  $R(\theta)$  is the ratio, at the boundary, of some field component  $F_r$  in the reflected wave to the same field component  $F_i$  in the incident wave.  $F_r$  and  $F_i$  are both measured very close to the boundary either at the atmosphere or at the ground. For the case of sharp boundaries, these reflection coefficients are called *Fresnel reflection coefficients*. For electromagnetic waves linearly polarized with the electric field vector in the plane of incidence (the  $x - z$  plane) the reflection coefficient at the ionospheric boundary is given as:

$$R = \frac{n \sin \theta - \sin \Psi}{n \sin \theta + \sin \Psi} \quad (2.3)$$

where

$n$ , is the refractive index as calculated by equation (4.4),

$\theta$  is the angle between the wave normal in the  $x - z$  plane and the boundary,

$\Psi$  is the angle between the transmitted wave normal and the boundary.

$\theta$  and  $\Psi$  are related to each other by Snell's law :

$$\cos \theta = n \cos \Psi \quad (2.4)$$

For electromagnetic waves linearly polarized with the electric field vector perpendicular to the plane of incidence (i.e., the  $x - z$  plane) the reflection coefficient at the ionospheric boundary is given as:

$$R = \frac{\sin \theta - n \sin \Psi}{\sin \theta + n \sin \Psi} \quad (2.5)$$

A better approximation should be used for the reflection coefficient from the ionosphere where the boundary is not sharp. In this case a stratified medium is assumed where the refractive index  $n(z)$  is a function of altitude, equivalent to a number of discrete thin layers in each of which the refractive index is constant. Snell's law applies at each of the boundaries :

$$n_k \cos \Psi_k = n_{k+1} \cos \Psi_{k+1} \quad (2.6)$$

In this case it can be shown that the correct formula for the reflection coefficient is given as [Budden, 1961; p. 117]:

$$R = i \exp \left( -2ik \int_0^{z_0} q dz \right) \quad (2.7)$$

where

$$q = \sqrt{n^2 - \cos^2 \theta},$$

$z_0$  is the height where  $q = 0$  and thus at which the wave is reflected.

Under night time conditions, the reflection height rises to approximately 90 km, where the Earth's magnetic field creates a strong anisotropy which leads to polarization coupling. In this case the reflection coefficients  $R^s$  and  $R^i$  must be regarded as matrices and written in the form  $\mathbf{R}^s$  and  $\mathbf{R}^i$  where

$\mathbf{R}_d^i(\theta) = \begin{bmatrix} \parallel R_{\parallel}^i(\theta)_d & \perp R_{\parallel}^i(\theta)_d \\ \parallel R_{\perp}^i(\theta)_d & \perp R_{\perp}^i(\theta)_d \end{bmatrix}$  is the complex ionospheric reflection coefficient matrix looking up in the ionosphere from height  $d$  and

$\mathbf{R}_d^g(\theta) = \begin{bmatrix} \parallel R_{\parallel}^g(\theta)_d & 0 \\ 0 & \perp R_{\perp}^g(\theta)_d \end{bmatrix}$  is the complex reflection matrix looking down from height  $d$  towards the ground.

The notation  $\parallel$  for  $R$ 's denotes polarization parallel to the plane of incidence while the notation  $\perp$  denotes polarization perpendicular to the plane of incidence. The first subscript on the  $R$ 's refers to the polarization of the incident wave while the second applies to the polarization of the reflected wave. These reflection coefficients are calculated and used in LWPC simulations.

In this case the modal equation given in (2.2) converts to a determinantal equation given by:

$$\left| \mathbf{R}_d^{(i)}(\theta) \mathbf{R}_d^{(g)}(\theta) - \mathbf{I} \right| = 0 \quad (2.8)$$

The total electric field at a great circle path (GCP) distance  $d$  from a transmitter has the form

$$E_{\text{total}}(d) = \frac{1}{\sqrt{|\sin(d/R_E)|}} \sum_n^{\infty} A_n^{T,R} \exp[-ik_0 \sin(\theta_n) d] \quad (2.9)$$

and is the electric field that would be measured along a direct path between a transmitter and receiver. In the presence of an HF heater induced disturbance of the  $D$  region of the ionosphere, there is the additional field scattered from the disturbed region which causes the amplitude and phase changes in the total received VLF signal to be different than that given by equation (2.9).

We now consider the hypothetical case in which only a single waveguide mode (say mode  $n=1$ ) is excited, so that  $n=1$  and  $A_1^{T,R}=1$ . Assuming that the ambient electron density profile and collision frequency profile are known the field amplitude and the eigenangle corresponding to each mode can be calculated using equation (2.2) and (4.4). Thus the direct field measured at a receiver station in the absence of the

disturbance is given by:

$$e^o(x_R, y_R) = \frac{\exp[-ik_0 \sin(\theta^o) d]}{\sqrt{|\sin(d/R_E)|}} \quad (2.10)$$

where

$$k_0 = w/c,$$

$\theta^o$  is the eigenangle corresponding to the dominant single mode propagating along the direct path between the transmitter and the receiver,  $\sin(\theta^o)$  is generally simply written as  $S^o$ .

$$d = \sqrt{(x_R - x_T)^2 + (y_R - y_T)^2},$$

$(x_R, y_R)$  and  $(x_T, y_T)$  are the receiver and transmitter locations respectively,

$R_E$  is the Earth radius.

Using a single mode scattering formulation [Poulsen *et al.*, 1990] the scattered field at the receiver is given by:

$$\begin{aligned} e(x_R, y_R) &= \underbrace{e^o(x_R, y_R)}_{\text{direct field}} + \underbrace{e^s(x_R, y_R)}_{\text{scattered field}} \\ &= e^o(x_R, y_R) - \frac{ik_0^2}{4} \iint_P \underbrace{[S^2(x', y') - (S^o)^2]}_{\Delta S^2} \cdot \underbrace{e(x', y')}_{\text{field inside disturbance}} \cdot \\ &\quad H_0^{(2)}(k_0 S^o R') dx' dy' \end{aligned} \quad (2.11)$$

where

$e$  is the modal wave field (i.e., the total field seen at  $(x_R, y_R)$  in the presence of some disturbance in the waveguide),

$e^o$  is the unperturbed modal wave field, also called the 'direct field',



$e^s$  is the secondary or scattered field (i.e., the field seen at  $(x_R, y_R)$  due to the disturbance),

$S^o$  is the ambient value of  $S$  in the absence of any disturbance, (in the single mode case this is a constant independent of  $x$  and  $y$ ),

$\Delta S^2$  the difference between the square of the sine of the perturbed eigenangle with respect to the square of the sine of the ambient eigenangle,

$P$  is the region of integration which extends over that portion of the  $x - y$  plane that encompasses the disturbance,

$H_0^{(2)}$  is the Hankel function of second kind of order zero, and

$R' = \sqrt{(x_R - x')^2 + (y_R - y')^2}$  is the distance from each integration point  $(x', y')$  within the disturbance to the observation point  $(x_R, y_R)$ .

The amplitude change ratio measured at the receiver station is then simply given by:

$$A_R = \frac{|e^o(x_R, y_R) + e^s(x_R, y_R)|}{|e^o(x_R, y_R)|} \quad (2.12)$$

and the phase change measured at the receiver station is given by:

$$\Delta\phi = \angle [e^o(x_R, y_R) + e^s(x_R, y_R)] - \angle e^o(x_R, y_R) \quad (2.13)$$

Since the value  $e^o(x_R, y_R)$  can be calculated with (2.10) for a specific transmitter-receiver configuration when the ambient electron density and collision frequency profile is known, it is in principle possible to find the complex valued  $e^s(x_R, y_R)$  by using amplitude and phase changes in the VLF signal. We now demonstrate how this could be done using 3 different VLF measurements, as described in Chapter 1. For this purpose we continue to make the hypothetical assumption that all VLF signals (direct and scattered) consist only of one waveguide mode, and that we have in hand three separate measurements of  $e^s(x_R, y_R)$  at three different frequencies, which may well have to be acquired at three different locations (see Figure 4.3),

as is necessary in practice. Since the three calculated scattered fields  $e^s(x_R, y_R)$  for each of the receiver sites are complex, this information can be used to determine the collision frequency profile with 6 parameters or with 6 degrees of freedom.

There are mainly two steps in this inversion of scattered fields to determine the collision frequency profile. The first step is to find the eigenangle of the mode corresponding to the propagating scattered signal. For this purpose, we make use of the fact [Poulsen *et al.*, 1993] that:

$$e^s(x_R, y_R) = f[S(x', y'), P] \quad (2.14)$$

$$= -\frac{ik_0^2}{4} \iint_P [S^2(x', y') - (S^o)^2] e(x', y') H_0^{(2)}(k_0 S^o R') dx' dy' \quad (2.15)$$

where  $e^s(x_R, y_R)$  is a function of the unknown  $S(x', y')$  which is the sine of the eigenangle of the scattered mode and  $P$  corresponds to the region disturbed by the heater. Equation (??) can be simplified by assuming a cylindrically symmetric disturbance with a center at  $(x_d, y_d)$  and having a radius of  $r_0$  and

$$S(x', y') = \exp\left(-\frac{\sqrt{(x' - x_d)^2 + (y' - y_d)^2}}{r_0}\right) (\sin \theta^s - \sin \theta^o) + \sin \theta^o \quad (2.16)$$

where we assume a Gaussian form (in the lateral direction) for the disturbance which generates a scattered signal mode with an eigenangle value of  $\theta^s$ .

In this case,  $e^s(x_R, y_R)$  is of the form  $A \sin \theta^s - B \sin \theta^o$  where A and B are constants that can be found by doing the integration given in (2.14). Thus  $\sin \theta^s = \sin^{-1} \{1/A [e^s(x_R, y_R) + B \sin(\theta^o)]\}$  and it is possible to directly find the eigenangle  $\theta^s$  of the scattered mode for three different VLF signals.

The second step is to find the vector  $\vec{\nu} = (\nu_1, \nu_2, \nu_3, \nu_4, \nu_5, \nu_6)$ , the vector containing the six values of the disturbed collision frequency profile  $\nu(z)$  at six different altitudes  $z_i$ , satisfying the model equation (2.8) with  $\theta_j^s$  for three different VLF signal frequencies. However it is simpler to express the modal equation in the form :

$$h(\vec{\nu}, \theta_j^s) = 0 \quad (2.17)$$

where  $h$  is a function of different parameters of which only  $\vec{\nu}$  is unknown. In this form it is easier to visualize the Newton-Raphson algorithm used for the inversion and described below:

- 1) Start with an initial estimation of  $\vec{\nu}^0 = (\nu_1^0, \nu_2^0, \nu_3^0, \nu_4^0, \nu_5^0, \nu_6^0)$ .
- 2) For the  $m^{th}$  iteration, let

$$\frac{\delta h}{\delta \nu_i} = \frac{h(\vec{\nu}^m + \delta \vec{\nu}_i^m, \theta_j^s) - h(\vec{\nu}^m - \delta \vec{\nu}_i^m, \theta_j^s)}{2\Delta \nu_i} \quad (2.18)$$

where

$$\delta \vec{\nu}_i^m = \alpha_i \left( 0, \dots, \underbrace{1}_{i^{th} \text{ position}}, \dots, 0 \right),$$

$j = 1, 2, 3$  corresponding to three different frequencies,

$i = 1, 2, \dots, 6$  for six different collision frequency values.

$\alpha_j$  is a constant which will be referred as *step size*.

- 3) From among the twelve different values of  $h(\vec{\nu}^m \pm \delta \vec{\nu}_i^m, \theta_j^s)$  for  $i = 1, 2, \dots, 6$  choose  $i$  such that  $\epsilon = \sum_{j=1}^3 |h(\vec{\nu}^m + \delta \vec{\nu}_i^m, \theta_j^s)|$  is minimized. Let this index be  $k$ .

- 4) Update the value of  $\vec{\nu}^{m+1} = \vec{\nu}^m + \Delta \vec{\nu}$ , i.e., either increment or decrement the real or the imaginary part of  $\theta^s$  by  $\Delta \theta_R$  or  $\Delta \theta_i$  by:

$$\Delta \vec{\nu} = \left( 0, \dots, \underbrace{\frac{h(\vec{\nu}^m, \theta_j^s)}{\frac{\delta h}{\delta \nu_k}} \alpha_i}_{k^{th} \text{ position}}, \dots, 0 \right) \quad (2.19)$$

5) Go to step 2 and continue until  $\varepsilon < \varepsilon_{\text{desired}}$ .

It is apparent from this single mode analysis that it is in principle possible to find the collision frequency profile within a disturbed region approximately by processing a set of observed VLF amplitude and phase changes. In practice, VLF signals propagating in the earth-ionosphere waveguide are constituted of a summation of multiple waveguide modes, so that the total field at the receiver in the absence of a disturbance is given by equation (2.9), and the eigenangles  $\theta$  and excitation constants  $A_n^{T,R}$  must be calculated numerically using LWPC as described in Section 2.1. The scattered signal at the receiver must also be calculated numerically using the 3D code described in Section 2.2. The general algorithm used in such a case for the inversion of VLF measurements to determine the collision frequency profile is described in Section 4.2.

## Chapter 3

# Ambient Electron Density Profile

The amplitude and phase of subionospheric VLF signals are sensitively dependent on the altitude profile of electron density along the propagation path. In this chapter we pursue the possibility of utilizing this dependence for the determination of the ambient (i.e., prior to ionospheric modification via HF heating) electron density from measured values of VLF amplitude and phase. Knowledge of the ambient electron density profile greatly simplifies the determination of the collision frequency profile within a disturbed region, as described in Section 4.1.

The latitude region of interest in this dissertation is the subauroral region in which the HAARP facility is located, and the ionospheric conditions at these latitudes are strongly influenced by relativistic electron precipitation. It has recently been shown [Demirkol *et al.*, 1999] that the amplitude of subionospheric VLF signals propagating in these regions are indeed closely associated with relativistic electron fluxes as measured on satellites. This close association, and the fact that relativistic electron enhancements on the average occur in a well defined range of subauroral latitudes, enables us to interrelate the ambient electron density profiles at different points along the subauroral traverse of a VLF path, which in turn facilitates the determination of the ambient density.

In the following we review the results reported in Demirkol *et al.*[1999] and describe the method used to determine the ambient electron density profile from VLF data.

### 3.1 Ionospheric Effects of Relativistic Electron Enhancement Events

The Earth's outer magnetosphere is often populated to a surprising degree by relativistic electrons [Paulikas and Blake, 1979]. Enhancements in the relativistic electron fluxes may be an important source of energy input to the atmosphere. Those precipitating electrons with energies  $> 1$  MeV can penetrate to altitudes as low as 50 km, affecting the atmospheric chemistry throughout the mesosphere [Gaines *et al.*, 1995]. Relativistic electron precipitation events are also believed to be a significant source of odd nitrogen in the middle atmosphere, possibly affecting ozone concentrations in some regions of the atmosphere [Callis *et al.*, 1991]. Relativistic electron precipitation events are associated with magnetospheric activity and may appear more frequently near a solar minimum than solar maximum [Baker *et al.*, 1986]. These events are strongest at subauroral ( $4.5 < L < 7$ ) latitudes (See Figure 3.1).

The enhancements of energetic particle fluxes within and near the local loss cone are documented in data from low altitude satellites such as SAMPEX [Baker *et al.*, 1986] and UARS [Gaines *et al.*, 1995], while the relativistic electron population at geosynchronous orbit is measured on GOES-7 and GOES-8. The particle flux as measured on these satellites exhibit the well known relatively regular 27-day periodicity with typical rises on a 2 to 3-day time scale and decays on a 3 to 4-day scale [Baker *et al.*, 1986]. (See Figure 3.2).

As mentioned previously, VLF sounding of the lower ionosphere (i.e., the measurement of the amplitude and phase of subionospherically propagating VLF signals) is a sensitive tool for the detection of ionospheric conductivity changes due to changes in electron density and/or temperature, especially at altitudes below 90 km [Sechrist, 1974]. Some of the early work on relativistic electron precipitation events has indeed relied on subionospheric VLF measurements [Thorne and Larsen, 1976]. Thus VLF measurements can be used to quantitatively assess the degree to which relativistic electron enhancements observed at satellite altitudes are accompanied by enhanced precipitation into the ionosphere. For this purpose, we search for the ionospheric signatures of relativistic electron precipitation by interpreting the observed

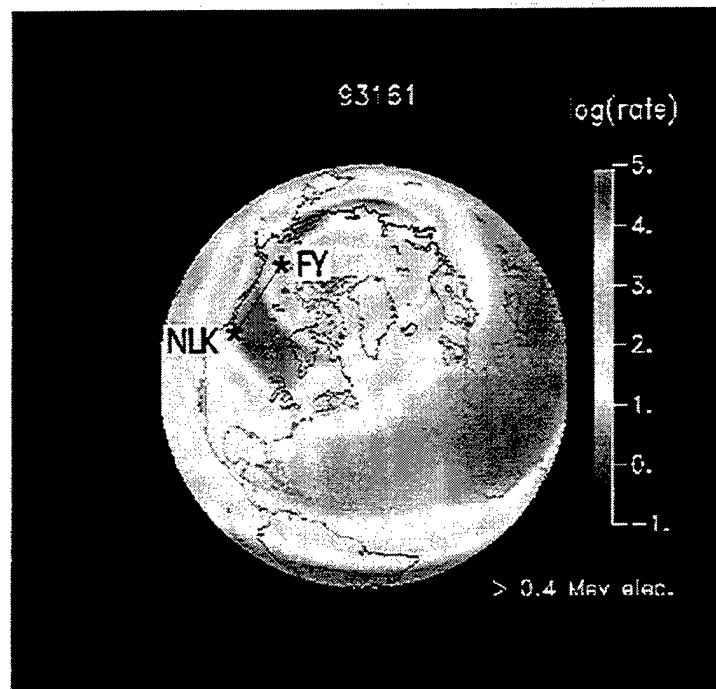


Figure 3.1: Configuration of NLK-FY path with respect to SAMPEX measurements of the relativistic precipitation zone. The NLK-FY path is chosen since the strongest flux levels are at the subauroral latitudes traversed by this path.

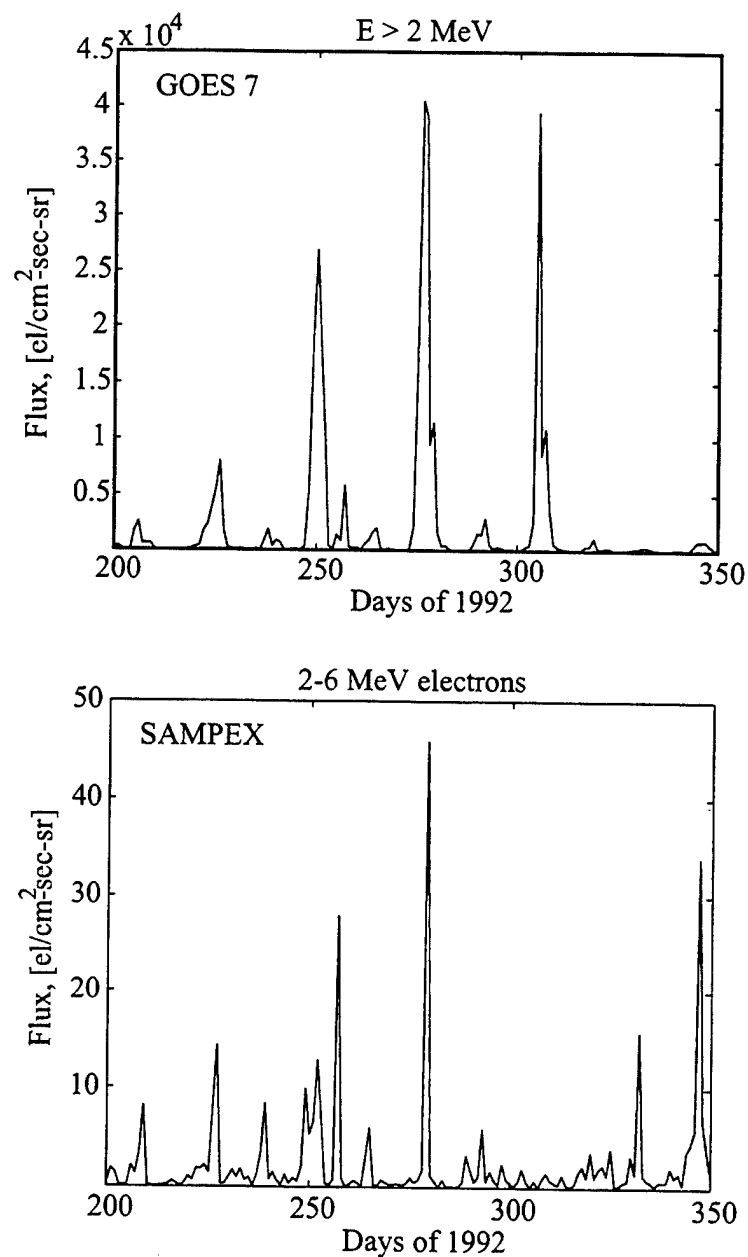


Figure 3.2: The particle flux measured on the GOES-7 and SAMPEX satellites exhibits the well known relatively regular 27-day periodicity with typical rises on a 2 to 3-day time scale and decays on a 3 to 4-day scale.



VLF amplitude variations in the light of theoretical models of VLF subionospheric wave propagation described in Chapter 2. Our results indicate that the nighttime *D* region is indeed strongly affected by this precipitation, with the nighttime electron density at 40-70 km altitudes clearly exhibiting the 27-day cycle associated with solar rotation.

### 3.1.1 Description of data

For this study, we focus our attention on the two month period of October and November 1992 (for which VLF data from Fort Yukon is continuously available) and utilize three different data sets, namely (i) VLF data, (ii) SAMPEX data, and (iii) GOES 7 data.

The VLF data consists of the recorded amplitude and phase of the subionospheric signal from the NLK transmitter (24.8 kHz) in Jim Creek, Washington (121.91° W, 48.20° N) as received at Fort Yukon (FY), Alaska (145.21° W, 66.56° N) during the period Oct-Nov 1992. Figure 3.3-a shows the NLK-FY great circle propagation path as well as lines of constant geomagnetic latitude. Since the fluxes of relativistic electrons exhibit fluctuations primarily at subauroral latitudes ( $4.5 < L < 7$ ), the NLK-FY path is well situated for monitoring the ionospheric effects of these relativistic electron enhancements.

Increases in the *D* region electron density caused by the high-energy particle precipitation increases the local electrical conductivity and perturbs the VLF signal propagating under the disturbed ionosphere. Figure 3.3-b shows a schematic description of this process.

The VLF data at FY during the Oct-Nov 1992 period was typically recorded during the period 0000 to 1200 UT. The signal amplitude in a 300 Hz band centered at the transmitter frequency (24.8 kHz) is regularly sampled and digitally recorded at a resolution of 100 Hz (i.e., samples taken at 10 ms intervals). Since the VLF signal amplitude can exhibit significant variation over short time scales, for example in response to burst precipitation effects [Cotton and Smith, 1991] or auroral electrojet enhancements [Cummer et al., 1996], studies of long term behavior are facilitated

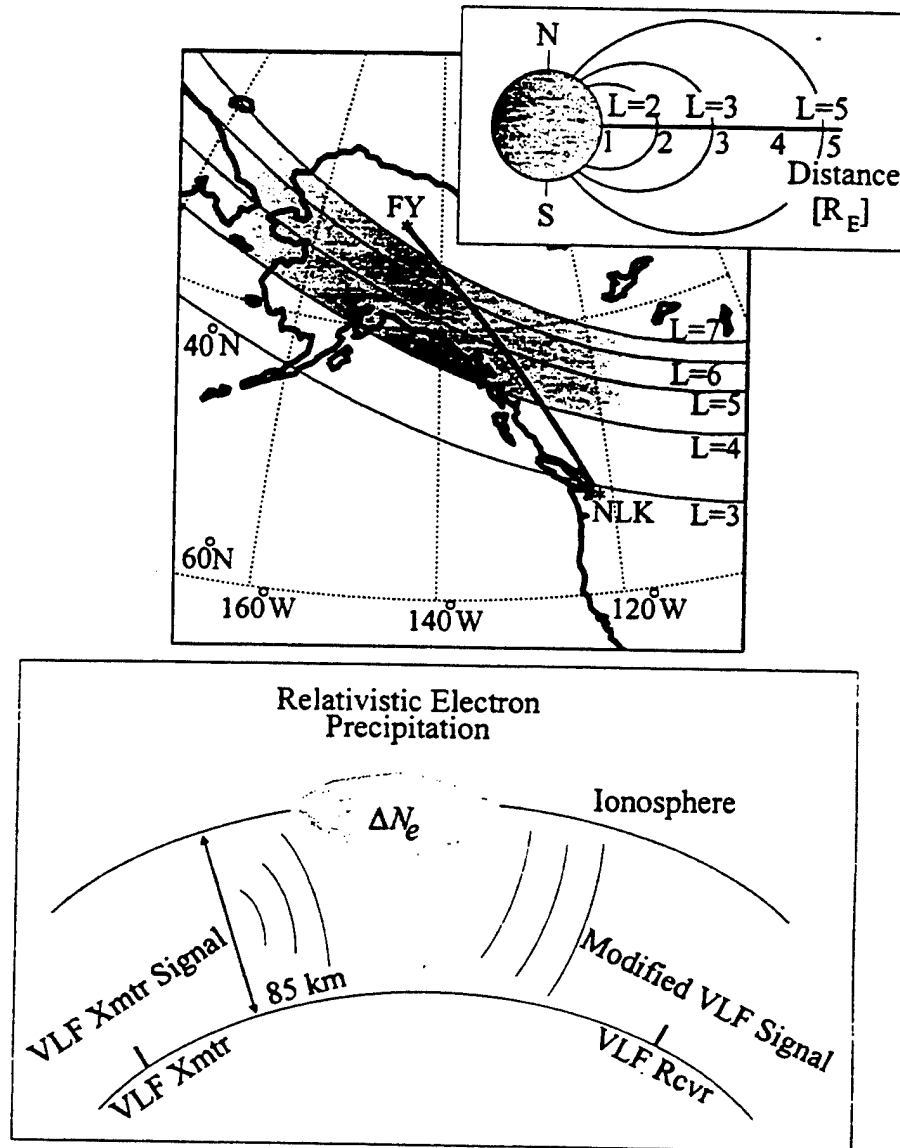


Figure 3.3: (a) A geographic view of the VLF propagation path from NLK to Fort Yukon, Alaska. The NLK-FY path is situated such that the relativistic precipitation region (shown shaded) covers a significant portion of the great circle propagation path. (b) The mechanism of the particle precipitation-VLF interaction is schematically shown above. A ground VLF transmitter (T) launches a signal into the earth-ionosphere waveguide. In the region of relativistic particle precipitation the local electron density is increased by  $\Delta N_e$ , causing the local electrical conductivity to change. The waveguide signal propagating under the region of relativistic electron precipitation is modified in response to the conductivity change, allowing the observation of this conductivity change as phase and amplitude variations in the VLF signal.

through the use of data averaged over a number of hours on each day. For this purpose we chose to average the VLF data over the time interval 0600 to 0900 UT each day, during which the entire NLK-FY path was under darkness throughout the study period. For each day, this simple 3 hour average of the signal amplitude is designated as the 'average' signal amplitude.

The Proton/Electron Telescope (PET) [Cook *et al.*, 1993] on SAMPEX is composed of an array of silicon solid state detectors that identify and measure the kinetic energy of electrons from  $\sim 1$  to  $\sim 30$  MeV and of H and He isotopes from  $\sim 20$  to  $\sim 80$  MeV/nuc. The SAMPEX data used in this work are integral fluxes of  $> 4$  MeV electrons measured in specific passes nearby the subionospheric paths.

The GOES-7 Energetic Particle Sensor (EPS) measures electrons from 0.6 to greater than 4.0 MeV, protons from .8 to 500 MeV, and alpha-particles from 4 to 500 MeV [Goes *Handbook*, 1994]. The electron measurements are made via solid state surface barrier detectors within a dome subassembly. The data used in this work are 5-minute averages of the integral fluxes of  $> 2$  MeV electrons.

### 3.1.2 Ground and Satellite Data Comparisons

The 'average' VLF amplitude for the October and November 1992 period is compared in Figure 3.4 with the corresponding satellite particle data measured by GOES-7. The GOES-7 electron flux maxima are clearly associated with the amplitude minima in the VLF data. A 27-day cycle is clearly apparent in the VLF data, similar to that observed in GOES data for the relativistic electron enhancement events, with the same 3-4 days of rise and fall times. In association with the two large electron flux enhancements which peak on days 276 and 305, the VLF signal amplitude exhibits changes  $> 9$  dB with rise and fall times of a few days. The VLF amplitude minima are delayed by about two days with respect to the peaks in GOES data; possible reasons for this delay are discussed later. The two smaller peaks in the GOES data, which are an order of magnitude below the two main peaks, are not associated with strong VLF amplitude minima.

To our knowledge this is the first observation of a subionospheric VLF amplitude

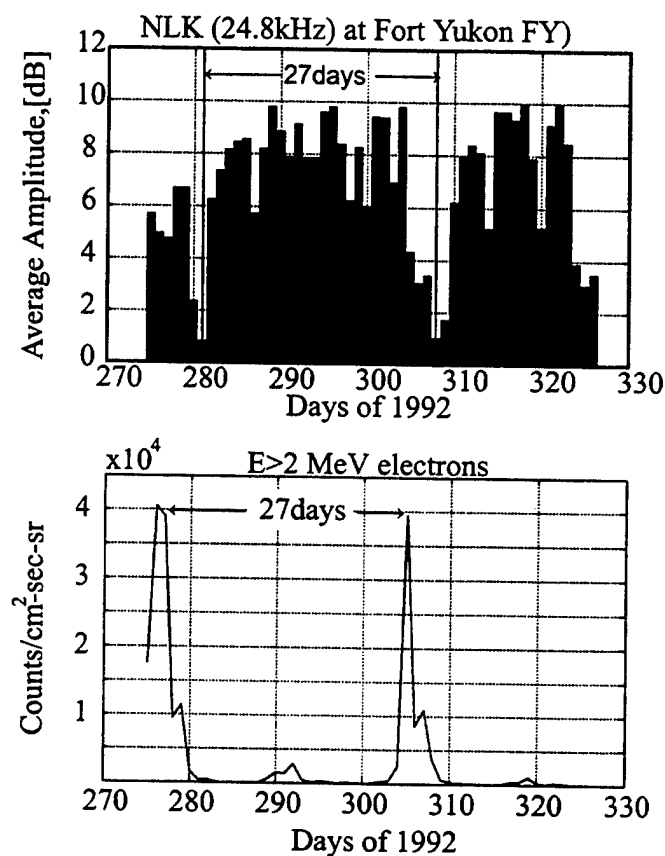


Figure 3.4: (a) The three-hour-averaged amplitude of the NLK signal (24.8 kHz) at Fort Yukon (FY) on each day. (b) Electron precipitation flux as measured on GOES-7. A 27-day variation is apparent in each data set.

variation exhibiting the same 27-day cycle as the relativistic electron enhancements events, thus indicating that the nighttime lower ionospheric electron density is detectably affected by the solar rotation. We note that since we use 3 hr averages of the VLF data, any measurement noise in the 300 Hz VLF channel is significantly reduced, and the daily variations shown in Figure 3.4-a are true indications of day to day changes in the lower ionosphere, principally due to auroral effects and long term precipitation associated with the auroral electrojet [Cummer *et al.*, 1996]. The 27 day variation is clearly the dominant effect, imposed on top of these other variations. At the same time the variability of the nighttime ionosphere due to the other auroral effects probably accounts for the lack of a VLF amplitude minima associated with the smaller peak in the GOES-7 data near day 292 (Figure 3.4). Using the three-hour-averaged amplitude, it appears that only relativistic electron enhanced flux levels above  $\sim 3 \times 10^3$  el/cm<sup>2</sup>-sr-s produce ionospheric effects that stand out in the presence of other ionospheric variations. Figure 3.5 shows the VLF signal amplitude for the same three hour period for two days when the flux level is at the maximum and minimum levels.

In view of the remarkable clarity by which the relativistic electron enhancement peaks are manifested in the daily averaged VLF data, it is interesting to consider whether the NLK-FY and GOES-7 data sets exhibit correlation on shorter time scales. Figure 3.6 shows comparison of data at 5 min resolution for a selected period (0600-0900 UT on October 25, 1992) in the vicinity of one of the peaks. We see that the VLF intensity increases in response to a decrease in the electron flux. In general a correlation coefficient of magnitude  $\sim 0.7$  was calculated between the two time series.

### 3.1.3 Model Calculations

The coincident occurrence of subionospheric VLF signal changes and relativistic electron enhancement peaks suggest that significant enhanced precipitation accompanies the enhancement events. In order to determine whether the observed VLF amplitude signatures are consistent with the ionospheric changes expected to be produced by such relativistic electron precipitation, we theoretically model the propagation of the

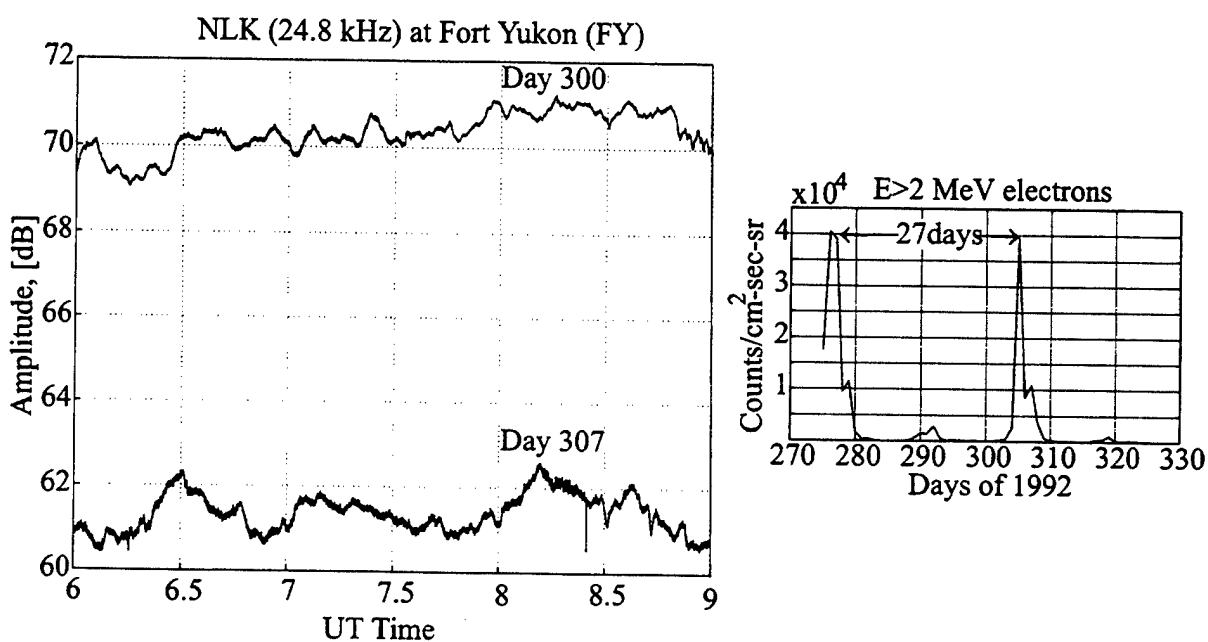


Figure 3.5: VLF signal amplitudes on days 300 and 307 shown in the interval 0600-0900 UT. The difference in the amplitude for these two days is  $> 10$  dB. VLF signal amplitude from Day 307 corresponds to a day where an electron precipitation enhancement takes place, while the signal from Day 300 is a day where the relativistic electron flux level is moderate.

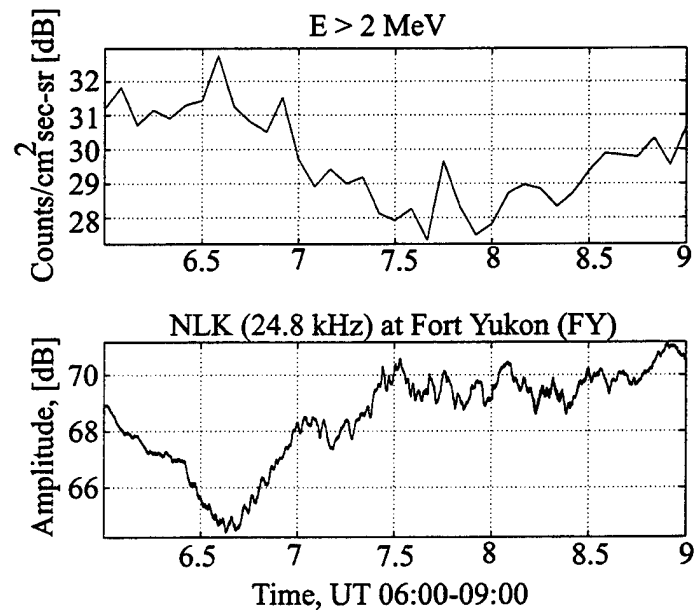


Figure 3.6: 5-minute average GOES-7 data appears to be strongly correlated with VLF amplitude. Correlation coefficients up to  $\sim -0.7$  are calculated.

VLF signal in the earth-ionosphere waveguide along the great circle path from NLK to FY. For this purpose, we use the Long Wave Propagation Capability (LWPC) code described in Section 2.1. The disturbance along the NLK-FY propagation path is modeled as a segment of the earth-ionosphere waveguide with a perturbed electron density profile caused by relativistic electron precipitation. Figure 3.7-a and 3.7-b show perturbed electron density profiles associated with different flux levels as determined by the method of *Gaines et al.* [1995]. Energetic electron data from SAMPEX, specifically integral flux of  $> 4$  MeV electrons, which was recorded during passes when the satellite was closest (in longitude) to the propagation path, is used in order to have the best estimate of electron flux levels in the ionospheric region which lies above the VLF path. A time period in the vicinity of the peak in relativistic flux on day 305 was chosen for this purpose.

There are two notable characteristic of the flux enhancements shown in Figure 3.8-a. First, we note that the largest flux level changes occur between  $5 < L < 7$ . Second, we note a significant spatial expansion of the disturbed region following day 304 which covers an increasingly larger segment of the NLK-FY path. This spatial expansion is the likely reason for the  $\sim 2$  day delay of the VLF amplitude minima with respect to the relativistic enhancement peak which was noted earlier in connection with Figure 3.4. Note that the VLF amplitude change is proportional to the electron enhancement as well as the length of the path segment affected [*Inan and Carpenter, 1987*].

For the VLF propagation model calculations, the propagation path NLK-FY was segmented using electron density profiles associated with the actual flux levels shown in Figure 3.8-a. Figure 3.8-b shows flux levels used in our model as derived from SAMPEX data for  $L \simeq 6$ . LWPC code calculations were carried out using these models of the ionospheric disturbance. The results shown in Figure 3.9 predict  $\sim 7$  dB maximum amplitude decrease, which compares generally well with the observed 9 dB signal amplitude decrease. The somewhat lower calculated amplitude change may be due to the fact that  $> 4$  MeV electron flux used to determine the associated electron density profiles, underestimated the relativistic electron enhancements which generally involve electrons with energies  $> 0.5$  MeV.



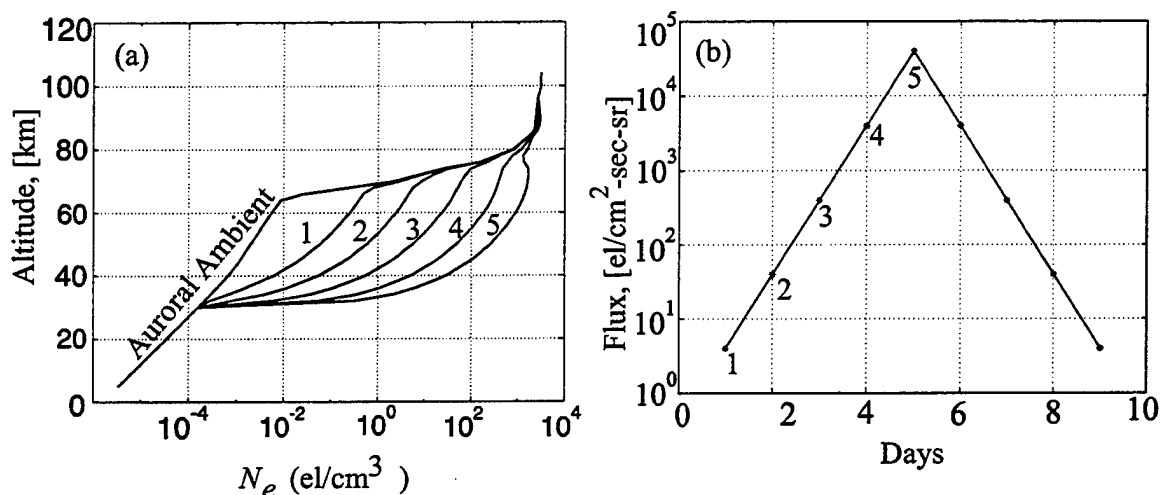


Figure 3.7: (a) Ionization profiles corresponding to the different levels (1, 2, 3, 4, 5) of relativistic electron precipitation fluxes as shown in (b). A typical relativistic electron precipitation enhancement shown here rising and falling in 9 days. In many cases event durations are as much as 10-15 days. The flux levels and energy spectra of the precipitation was taken to be as given by *Gaines et al.* [1995], based on measurements on the UARS satellite.

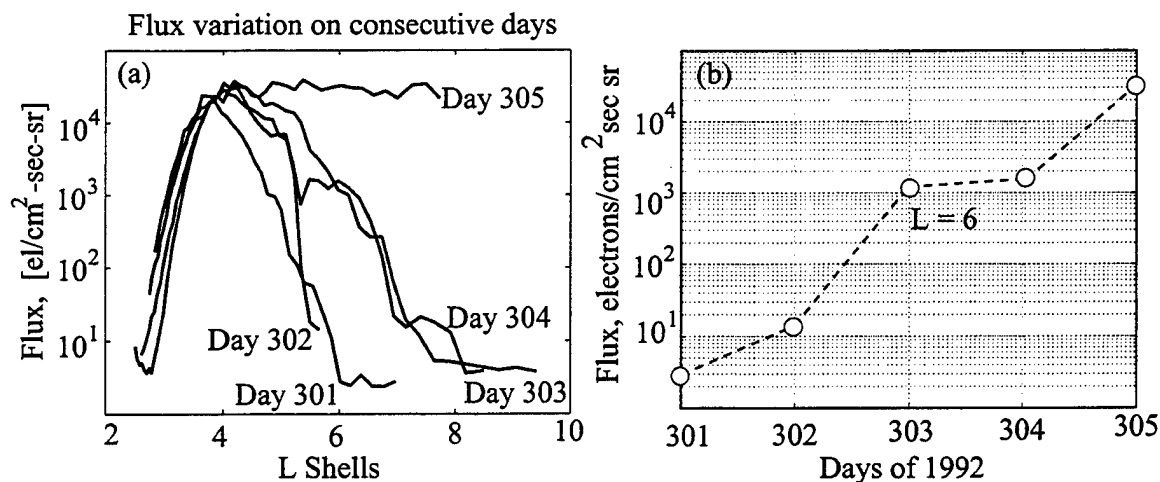


Figure 3.8: (a) Integral flux of  $> 4$  MeV electrons measured on each day on SAMPEX during passes nearest (in longitude) to the NLK-FY path. The largest flux variation generally occurs near  $L \sim 6$ . (b) Flux level at  $L = 6$  as a function of day.

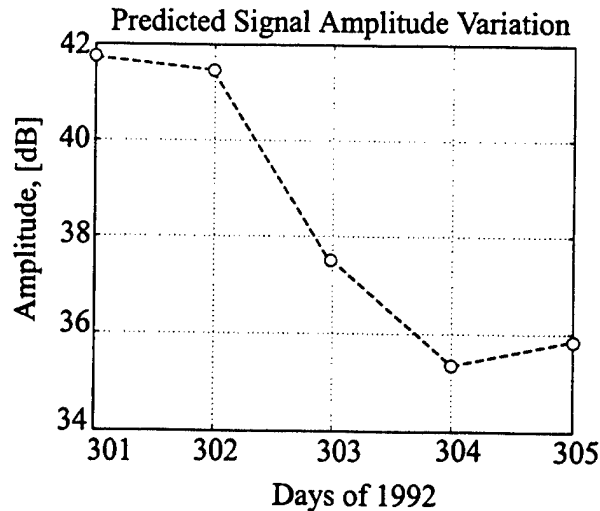


Figure 3.9: The predicted NLK signal amplitude variation as observed at Fort Yukon.

Comparison of VLF amplitude data with GOES-7 and SAMPEX data on relativistic electron flux levels show a clear association between the two data sets in the case of two successive relativistic electron enhancement episodes for which VLF data is available. The VLF amplitude and particle flux levels measured on GOES-7 show the same 27 day cycle and 2-3 days of rise and fall times for a characteristic relativistic precipitation enhancement event. VLF signal amplitudes exhibited  $> 9$  dB decreases associated with the electron flux level enhancements indicating that the nighttime electron density at 40-70 km altitudes is strongly influenced by the solar rotation, via the relativistic electron enhancement events driven by the solar wind. The ionospheric effect of the relativistic electron enhancements was observed only when the flux was above  $3 \times 10^3$  el/cm<sup>2</sup>-sr-s, apparently because of the fact that the VLF signature of the enhancement for lower fluxes is suppressed by other ionospheric variations.

Comparison of our VLF observations with theoretical predictions of amplitude decreases of  $> 7$  dB obtained using propagation model calculations provides satisfactory agreement. Calculations also show that the amplitude change associated with the lower peaks of the relativistic electron enhancement are less than 1 dB, not observable

in the presence of larger ionospheric variations associated with auroral effects.

We conclude on the basis of both observation and the theoretical analysis presented here that the conductivity of the nighttime lower ionosphere at subauroral latitudes is strongly modulated by the relativistic electron precipitation which accompanies relativistic electron enhancements. High-energy precipitation causes electron density enhancements in the  $D$  region of the ionosphere, which in turn affect VLF waves propagating in the perturbed earth-ionosphere waveguide. This realization also provides the first evidence of a detectable influence on the nighttime lower ionosphere of solar rotation, imposing a 27-day cycle on top of other variations of this region of our atmosphere.

Our results further indicate that VLF remote sensing can be a powerful tool for investigation of relativistic electron flux enhancements and their ionospheric and mesospheric effects. A system with multiple receiving stations observing VLF signals that cross the affected regions (see Figure 3.4) could be used to assess the spatial distribution of precipitation as well as the precipitation flux levels.

## 3.2 Determination of the Electron Density Profile

The close association between relativistic electron flux and VLF signal level as reported by *Demirkol et al.* [1999] and described in the previous section, and the relatively well defined latitude range over which these enhancements occur, form the basis of our method for determination of the electron density profile in different regions along VLF subauroral propagation path.

Noting that the largest day to day variations occur at  $L \simeq 6$ , we model the geomagnetic latitude distributions of the precipitating electron fluxes as a Gaussian with a center at  $L=6$  as illustrated in Figure 3.10. The Gaussian spatial distribution of the flux level is illustrated in Figure 3.10-a. A stepwise approximation to the Gaussian is made as illustrated. Each level of flux denoted by a, b, c and d results in an associated electron density profile as shown in Figure 3.10-b. The peak value and the horizontal width of this Gaussian function is yet to be determined. In order to find the width and the peak of the Gaussian, and thus to be able to identify the electron density

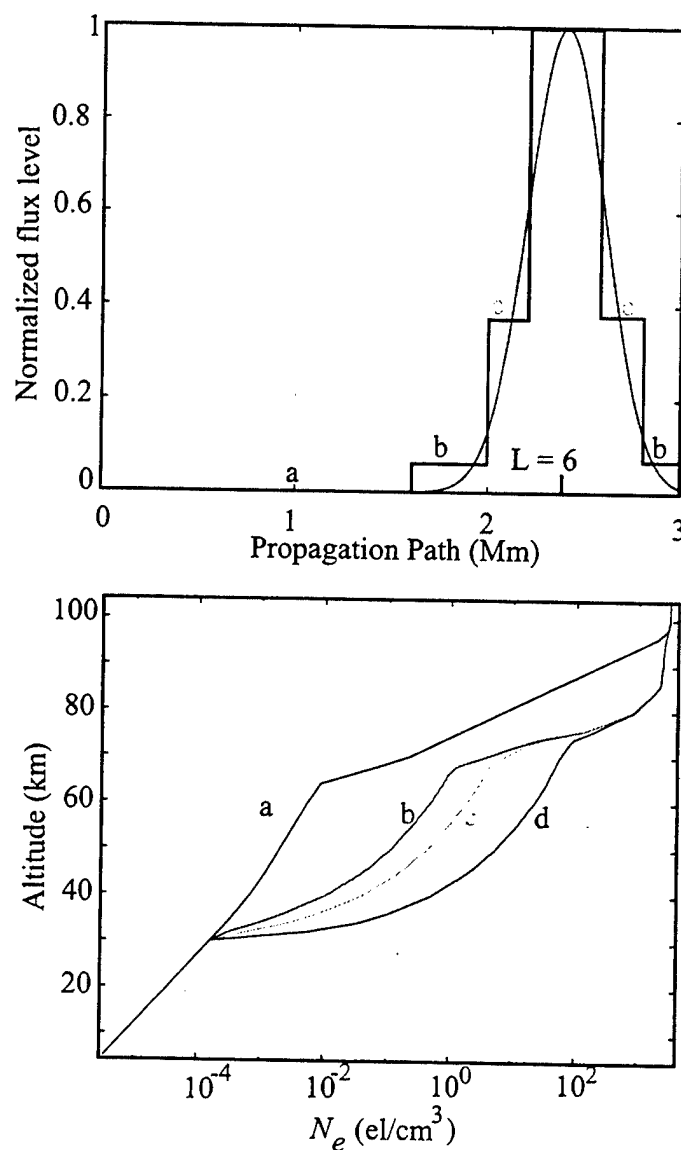


Figure 3.10: The flux level is modeled as a Gaussian centered at  $L = 6$ . Since each flux level corresponds to a different electron density profile, it is possible to segment the propagation path, each segment including the corresponding electron density profile as shown a, b, c and d above.

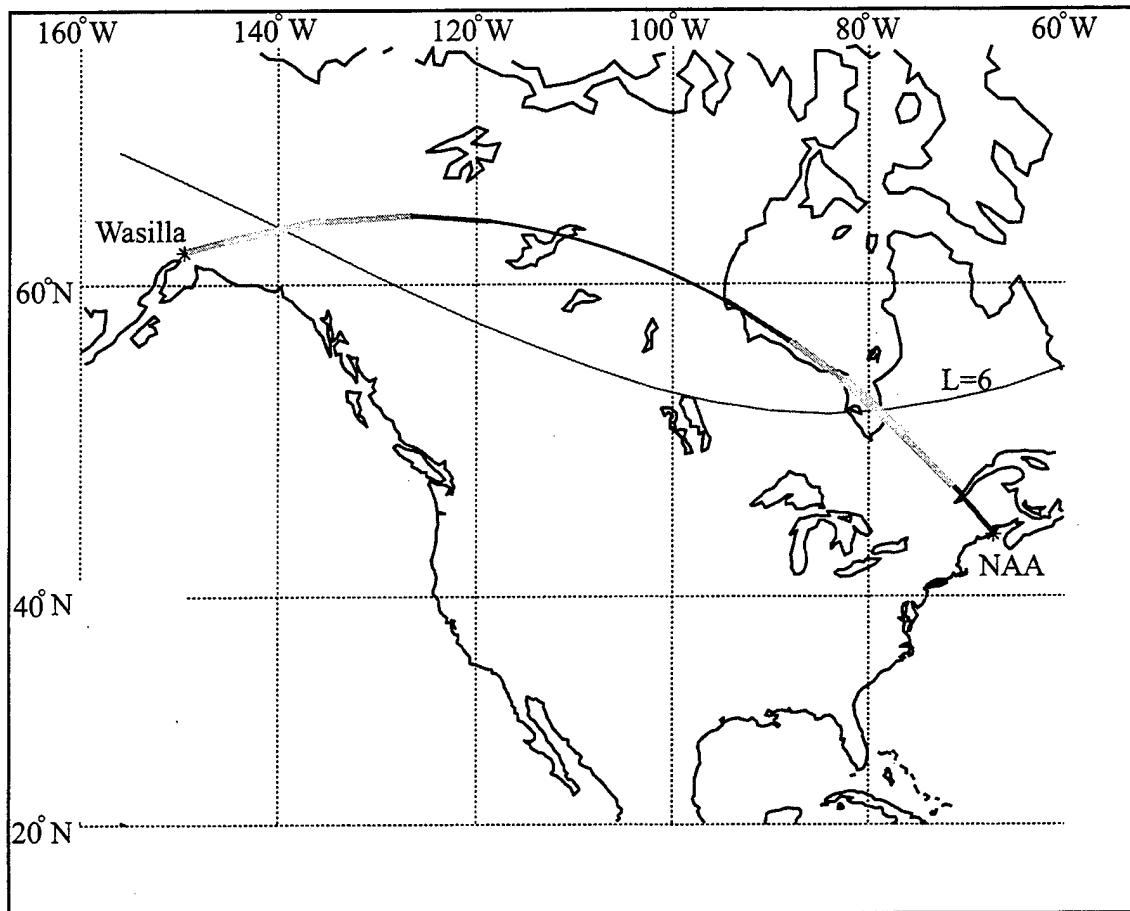


Figure 3.11: The segmentation of the VLF propagation path from NAA to Wasilla according to the Gaussian spatial flux model centered at  $L = 6$ .

profiles corresponding to each of the flux levels, the measured VLF signal amplitudes are used. For a set of different peaks and widths, a segmentation of the propagation path is made, determined by the width of the Gaussian. Figure 3.11 shows the segmentation of the VLF propagation path from NAA to Wasilla, a receiver site used in the March 1999 HAARP Heating campaign, according to this Gaussian spatial distribution model for the relativistic electron flux. In each segment of the propagation path, the flux level is different. As the VLF signal propagates from the transmitter to the receiver, it enters the region affected by the relativistic electron precipitation. As the signal propagates toward higher latitudes, it encounters increasing flux levels, as in each subsequent segment the electron density in the ionosphere increases further and further, reaching its maximum near to  $L \sim 6$ . At the center of the Gaussian distribution corresponding to  $L=6$ , the flux level has the highest value. In the 2D modeling of the propagation of the VLF signal, the electron density profile in the ionosphere over the region drawn in blue in Figure 3.11 is the profile produced by the highest flux as shown in Figure 3.10. As the VLF signal continues to propagate (towards lower latitudes) the flux level decreases and thus the electron density profile in the ionosphere changes. This latitude dependence of the electron density is accounted for in LWPC by using different electron density profiles in different segments of the propagation path.

In this manner LWPC models are generated for a range of Gaussian models with different width and peak values, with the amplitudes of the VLF signal at the receiver corresponding to each of the different models calculated as a byproduct of the LWPC calculations. Thus it is possible to construct a table where each Gaussian width and peak flux level corresponds to a particular VLF amplitude. Having such a table then enables us to identify a unique pair of width and peak by matching VLF amplitudes at three frequencies, necessarily arriving at the receiver over three different paths with the same flux model imposed on them. This method is used to determine the ambient electron density profile along the propagation path of the VLF signal prior to the inversion algorithm.

## Chapter 4

### Modified Collision Frequency

Powerful ionospheric heaters are typically designed to focus an intense beam of HF radiation onto a relatively small spot with transverse dimensions of  $\sim 10$  to  $20$  km at  $D$  region altitudes of interest here. The primary physical effect of a powerful HF electromagnetic wave in the  $D$  region is to heat the electrons via absorption of the wave, which in turn enhances the frequency of the collisions between these electrons and the ambient neutrals and heavy ions. In addition, the enhanced electron temperature changes the rates of chemical reactions which determine the electron density profile. Both electron density and collision frequency changes result in the modification of the electrical conductivity of the heated ionospheric region. Such a patch of ionosphere with modified collisional frequency and electron density in turn diffract VLF radio waves propagating in its vicinity [Barr *et al.*, 1985]. Such diffraction of the VLF radio waves due to ionospheric heating by the HIPAS facility was illustrated in Section 1.4.

Of the two effect discussed above, the electron density modulation resulting from the temperature dependence of the dissociative recombination rates of  $O_2^+$  and  $NO^+$  [Rodriguez and Inan, 1994] is not significant in the context of this work. That this is the case can be seen from the characteristic time of electron density modulation (resulting from the modulation of the recombination process) which is given by [Stubbe *et al.*, 1982] :

$$T_n = \frac{1}{\alpha_{\text{eff}} N_e} \approx \frac{2.5 \times 10^{12}}{N_e (\text{m}^{-3})} \text{ s} \quad (4.1)$$

For a typical  $D$  region,  $N_e \simeq 10^9 \text{ m}^{-3}$ , while  $T_n$  is of the order of thousands of seconds. Since we measure the effects of heating over time scales of seconds, any change in electron density due to changes in the recombination rates can therefore be neglected.

Having described a method in Chapter 3 for the determination of the ambient electron density profile, and assuming this ambient profile to be constant during the heating process, we now discuss the HF heater-induced modification of the collision frequency.

## 4.1 HF Heater-Induced Modification of Electron Collision Frequency

For heater wave power densities at 30 km altitude of  $P_d < 10^{-2} \text{ W/m}^2$ , it is possible to use a model for which  $\nu \sim v_{\text{th}}^2$  where  $v_{\text{th}}$  is the thermal velocity [Inan *et al.*, 1991]. Under these conditions the electron distribution function can be assumed to remain Maxwellian, i.e.,

$$f(c) = N_e \left( \frac{m_e}{2\pi k T_n} \right)^{3/2} \exp \left( -\frac{m_e v_{\text{th}}^2}{2k_B T_n} \right) \quad (4.2)$$

where

$v_{\text{th}} = |\vec{v}_{\text{th}}|$  is the random thermal velocity of the electrons,

$N_e$ , is the number density of the electrons,

$m_e$ , is the mass of an electron,

$k_B$ , is Boltzmann's constant, and

$T_n$ , is the ambient temperature of the electrons.



In this case the modified electron collision frequency  $\nu$  can be written as [Maslin, 1974]:

$$\nu = \left(\frac{\nu_0}{2}\right) + \sqrt{\left(\frac{\nu_0}{2}\right)^2 + \frac{2\nu_0\Gamma}{3Gn_e k_B T_n}} \quad (4.3)$$

where

$\nu_0$  is the ambient electron collision frequency,

$\Gamma$  is the absorbed wave power, and

$G$  is the fraction of electron energy lost per collision, typically taken to be in the range of  $1.3 \times 10^{-3}$  to  $6 \times 10^{-3}$  [Huxley and Zaazou, 1949; Fejer, 1970].

The absorbed wave power  $\Gamma(z)$  at each altitude can be calculated by propagating the wave incrementally in altitude. The absorption of the two propagating waves corresponding to the ordinary and extra-ordinary modes produce the total heating.

The refractive index  $n$  at each altitude can be calculated using equation (4.4):

$$n^2 = 1 - \frac{X(U - X)}{U(U - X) - \frac{1}{2}Y^2 \sin^2 \psi + S_R} \quad (4.4)$$

where

$$S_R = \sqrt{\frac{1}{4}Y^4 \sin^4 \psi + Y^2(U - X)^2 \cos^2 \psi},$$

$$Y = |\vec{Y}| = |e\vec{B}_0| / (m_e \omega),$$

$\vec{B}_0$  is the constant magnetic field of the Earth,

$e$  is the charge of an electron,

$m_e$  is the mass of an electron,

$\omega$  is the angular frequency of the heating wave in radians/sec,

$$U = 1 - iZ,$$

$$Z = \nu/\omega,$$

$$X = N_e e^2 / (\epsilon_0 m \omega^2), \text{ and}$$

$\psi$  is the angle between the wave vector  $\vec{k}$  and  $\vec{B}_0$ .

In this case, the absorbed power can be calculated at each incremental altitude as  $\Gamma_{\text{or}} = (P_d/2) \exp(2\chi_{\text{or}} \frac{\omega}{c} \Delta h)$  and  $\Gamma_{\text{ex}} = (P_d/2) \exp(2\chi_{\text{ex}} \frac{\omega}{c} \Delta z)$  where  $\chi_{\text{or}} = \text{Im}(n_{\text{or}})$ ,  $\chi_{\text{ex}} = \text{Im}(n_{\text{ex}})$ . The absorbed power in each altitude increment is determined separately for each of the two elliptically polarized components (i.e., o-mode and x-mode) that constitute the input HF wave, with the total heating being a superposition of that due to each component [Taranenko *et al.*, 1992].

It is thus possible to determine the modified collision frequency profile, given the frequency, power density, polarization and  $\vec{k}$  vector orientation of the pump wave and for a specified ambient electron density and collision frequency profiles. An example effective collision frequency profile corresponding to heating by the HIPAS transmitter ( $P_d = 9.3 \times 10^{-4}$  Watts/m<sup>2</sup>; also see Section 1.4) is shown in Figure 4.1.

It is clear from the above discussion that the resultant altitude profile of effective collision frequency is a function of the ambient electron density and collision frequency profiles. The ambient electron collision frequency is largely determined by the density of the neutral atmospheric constituents and thus does not exhibit significant variations from night-to-night. On the other hand, the ambient electron density in the nighttime lower ionosphere is notoriously variable [Davies, 1990; p. 143 and Fig. 5.2]. This high degree of variability makes theoretical prediction of the effective collision frequency profiles highly uncertain and underscores the need for diagnostic experiments that can directly determine the modified collision frequency profile. Even if the ambient density profile is known, it should be noted that the HF heating model described in this section is relative simple and approximate, for example in terms of the numerical value and altitude dependence of the quantity  $G$ . In view of this, accurate determination of the modified collision frequency profile can best be done by measurement with methods such as the VLF D region diagnostics technique described in this dissertation.

Based on the fact that subionospheric VLF signals have been shown to exhibit detectable amplitude and phase changes in response to heating of the D region by HF

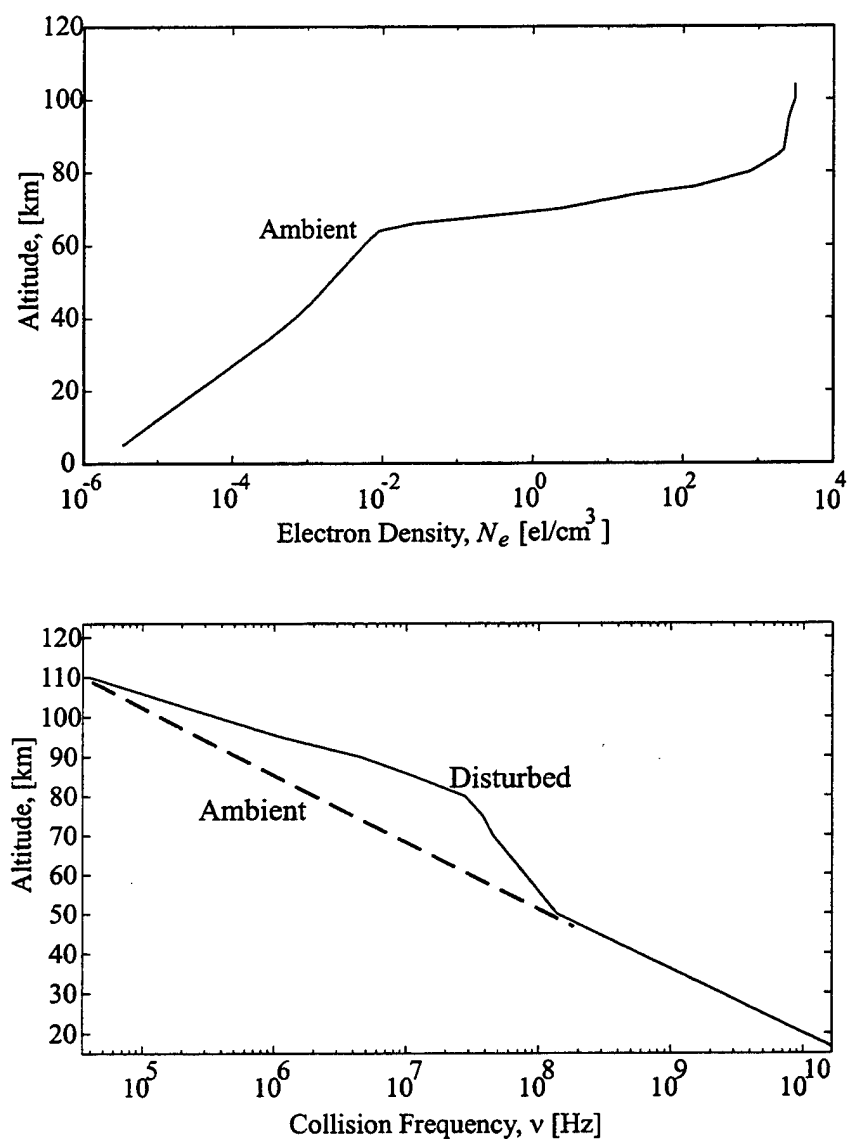


Figure 4.1: Calculated disturbed collision frequency profile for a given ambient collision frequency and electron density profile. The assumed angle between the wave normal and  $\vec{B}$  is  $13.5^\circ$ . The frequency of the heater wave is 2.86 MHz, and the two mode combined power of the HF transmitter is  $9.3 \times 10^{-4}$  watts/m<sup>2</sup>.

[Barr *et al.*, 1985; Bell *et al.*, 1995] or VLF waves [Inan, 1990; Inan *et al.*, 1992], such measurements can potentially be used to infer the altitude profile of effective electron collision frequency in a modified ionosphere. The development and application of an inversion method to this end is the main subject of this dissertation. In the next section, we describe this new procedure and apply it to two hypothetical examples. Application of the method to actual experimental data is the subject of Chapter 5.

## 4.2 Inversion Algorithm to Determine $\nu(z)$

The amplitude and phase changes,  $\Delta A$  and  $\Delta\phi$ , measured by VLF receivers in response to HF heating sensitively depend on ionospheric parameters as described in Chapter 2. Having determined the ambient electron density profile as described in Chapter 3, the only unknown parameter affecting  $\Delta A$  and  $\Delta\phi$  is the disturbed collision frequency profile  $\nu(z)$  in the heated region.

We now describe the inversion technique we use to determine  $\nu(z)$  from measured values of  $\Delta A$  and  $\Delta\phi$ . For this purpose, we use three VLF signals with different frequencies and propagation paths so as to have six measurements at our disposal to specify six degrees of freedom for the collision frequency profile. In the present work these six degrees of freedom are chosen to be the values of the electron collision frequency at six different altitudes as shown in Figure 4.2.

Receiver locations are chosen such that the three VLF signals pass under the heated region as illustrated in Figure 4.3. The fact that the three signals have different frequencies ensures that the resultant amplitude and phase changes provide nonredundant information.

In general, we can define a *calculated change vector*  $\vec{\Delta}$  in the form :

$$\vec{\Delta} = (\Delta A_1^c, \Delta\phi_1^c, \Delta A_2^c, \Delta\phi_2^c, \Delta A_3^c, \Delta\phi_3^c) \quad (4.5)$$

where the vector elements are calculated using the 3D LWPC code with a given collision frequency profile. Thus :

$$\Delta A_i^c = f_i(\nu_1, \nu_2, \nu_3, \nu_4, \nu_5, \nu_6), \quad i = 1, 3, 5,$$

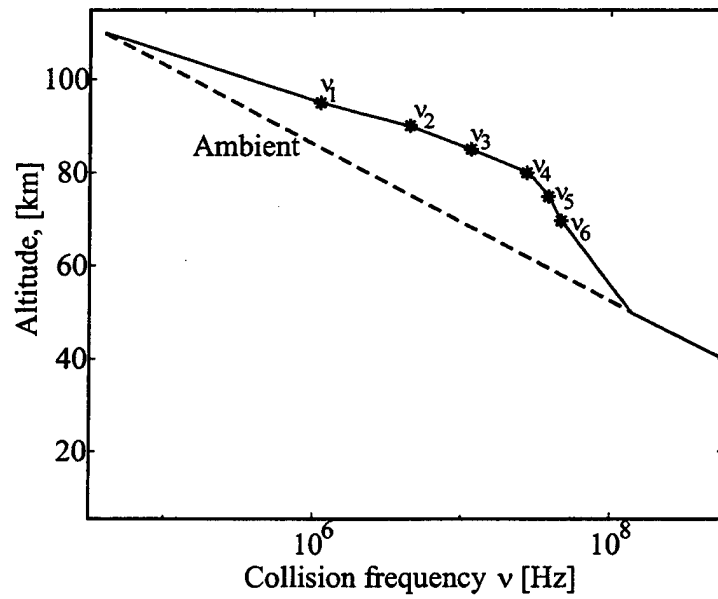


Figure 4.2: Collision frequency profile is modeled with six different values of collision frequency at six different altitudes in the *D*-region. The altitude range sampled is chosen on the basis of the sensitivity of the subionospheric VLF signal to changes at different altitudes.

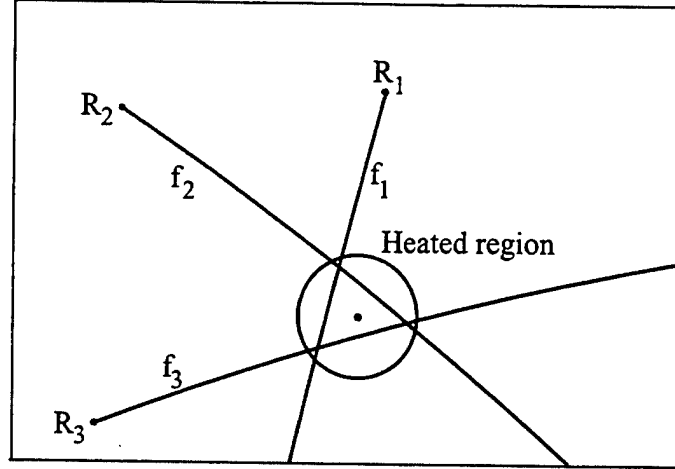


Figure 4.3: Three VLF signals with different frequencies propagating under a heated region will be used in the inversion technique. The propagation paths of the signals from the transmitters (T) to the receivers (R) are also different, since in general each VLF transmitter operates at a pre-allocated frequency.

$$\Delta\phi_i^c = f_i(\nu_1, \nu_2, \nu_3, \nu_4, \nu_5, \nu_6), \quad i = 2, 4, 6,$$

where  $\nu_1, \nu_2, \nu_3, \nu_4, \nu_5, \nu_6$  are the 6 parameters that define the collision frequency profile (Figure 4.2).

Note that each element of  $\vec{\Delta}$  is a function of the collision frequency profile as well as other parameters; the values of which are known.

Given the *measured change vector*  $\vec{\Delta}^{\text{data}} = (\Delta A_1, \Delta\phi_1, \Delta A_2, \Delta\phi_2, \Delta A_3, \Delta\phi_3)$ , where  $\Delta A_1, \Delta A_2, \Delta A_3$  are the three measured amplitude changes, and  $\Delta\phi_1, \Delta\phi_2, \Delta\phi_3$  are the corresponding measured phase changes, a simple algorithm for iteratively solving for the collision frequency profile  $\vec{\nu} = (\nu_1, \nu_2, \nu_3, \nu_4, \nu_5, \nu_6)$  can be described as follows :

- 1) Start with an initial estimate vector  $\vec{\nu}^0 = (\nu_1^0, \nu_2^0, \nu_3^0, \nu_4^0, \nu_5^0, \nu_6^0)$ , where the superscript 0 corresponds to the first iteration number.
- 2) For the  $m^{\text{th}}$  iteration, form 12 distinct collision frequency profiles based on the reference points :

$$\bar{\nu}^m = \bar{\nu}^{m-1} \pm \delta \bar{\nu}_j^m \quad (4.6)$$

where

$$\delta \bar{\nu}_j^m = \alpha_j(0, \dots, \underbrace{1}_{j^{\text{th}} \text{ position}}, \dots, 0) \text{ and } j = 1, 2, \dots, 6,$$

$\alpha_j$  is a constant which will be referred as *step size*, and

$m$  is the iteration number.

3) For each of the 12 profiles, find  $\bar{\Delta}$ .

4) For the new profile choose  $\bar{\nu}^{m+1} = \bar{\nu}^m + \delta \bar{\nu}_k^m$ ,  $k$  being the index which minimizes the error function defined as:

$$|\bar{\Delta}_k^m - \bar{\Delta}^{\text{data}}| = \sqrt{\lambda_1 |A_{1k}^R e^{j\Delta\phi_{1k}} - A_1^R e^{j\Delta\phi_1}|^2 + \lambda_2 |A_{2k}^R e^{j\Delta\phi_{2k}} - A_2^R e^{j\Delta\phi_2}|^2 + \lambda_3 |A_{3k}^R e^{j\Delta\phi_{3k}} - A_3^R e^{j\Delta\phi_3}|^2} \quad (4.7)$$

where the subscript  $k$  denotes the calculated values of  $\Delta A$  and  $\Delta\phi$ ,  $A^R = (A + \Delta A)/A$ , and  $\lambda_{1,2,3}$  are signal quality parameters determined by the signal-to-noise ratio at each receiver site. Note that to first order in  $\Delta A$  and  $\Delta\phi$ , the right-hand-side of (4.7) is simply the common mean square error function. The particular form used here is chosen for convenience, since  $A^R$  is one of the output parameters of the 3D VLF propagation code.

5) Repeat steps 2 through 3 with  $\bar{\nu}^{m+1}$  until the error is reduced below a desired level, i.e., until  $|\bar{\Delta}_k - \bar{\Delta}^{\text{data}}| < \varepsilon_{\text{desired}}$ .

Figure 4.4 shows the flow graph for this algorithm.

For a single VLF signal, each iteration corresponds to finding the amplitude and phase change for 12 different collision frequency profiles generated by  $\bar{\nu}^m \pm \delta \bar{\nu}_j^m$  for  $j = 1, 2, \dots, 6$  and choosing the profile whose predicted amplitude and phase change

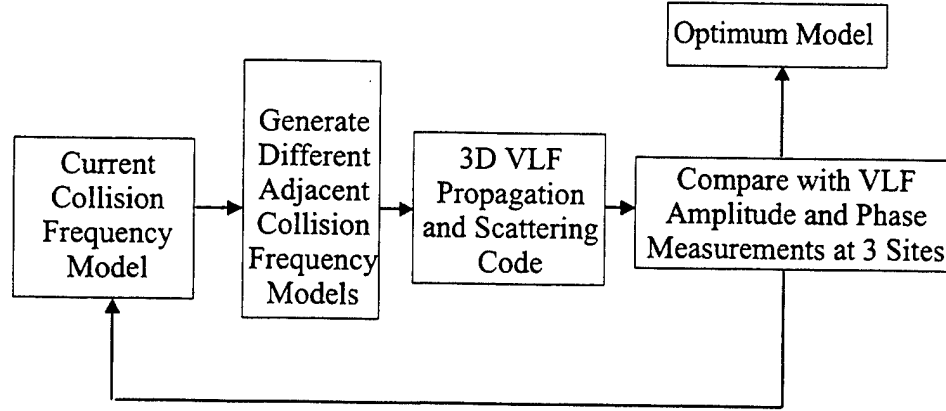


Figure 4.4: Flow graph for the inversion algorithm.

minimizes the right-hand-side of (4.7), as illustrated in Figure 4.5. In this Figure the amplitude and phase changes corresponding to the collision frequency profiles generated by  $\bar{\nu}^m \pm \delta\bar{\nu}_j^m$  for  $j = 1, 2, \dots, 6$  are shown as stars. The amplitude and phase corresponding to the initial collision frequency profile  $\bar{\nu}^0$  is shown as an open circle. The measured amplitude and phase change (in this case corresponding to  $A^R = 0.14$  dB and  $\Delta\phi = 0.95^\circ$ ) is shown in the upper right corner and is the desired model output. Among the different 12 profiles, we choose the profile for which the predicted amplitude and phase changes minimize the error function. The amplitude and phase change corresponding to this model is circled. In the next iteration step, the collision frequency profile corresponding to this point is used as the initial profile.

We now test the inversion algorithm by using the 3D VLF propagation and scattering model to calculate amplitude and phase changes for each of the three signals (with frequencies  $f_{1,2,3}$  and receiver sites  $R_{1,2,3}$ ) for a prespecified  $\nu(z)$  and use these as the measured change vector  $\bar{\Delta}$ . We test the inversion algorithm with two different example collision frequency profiles as shown in Figure 4.6. These collision frequency profiles are used to generate the measured change vector  $\bar{\Delta}$  consisting of the resulting amplitude and phase change predictions ( $A^R, \Delta\phi$ ) as shown in Table 4.1.

In order to start the inversion, the initial collision frequency profile  $\bar{\nu}^0$  is required and is determined by selection from among a set of generic collision frequency profiles



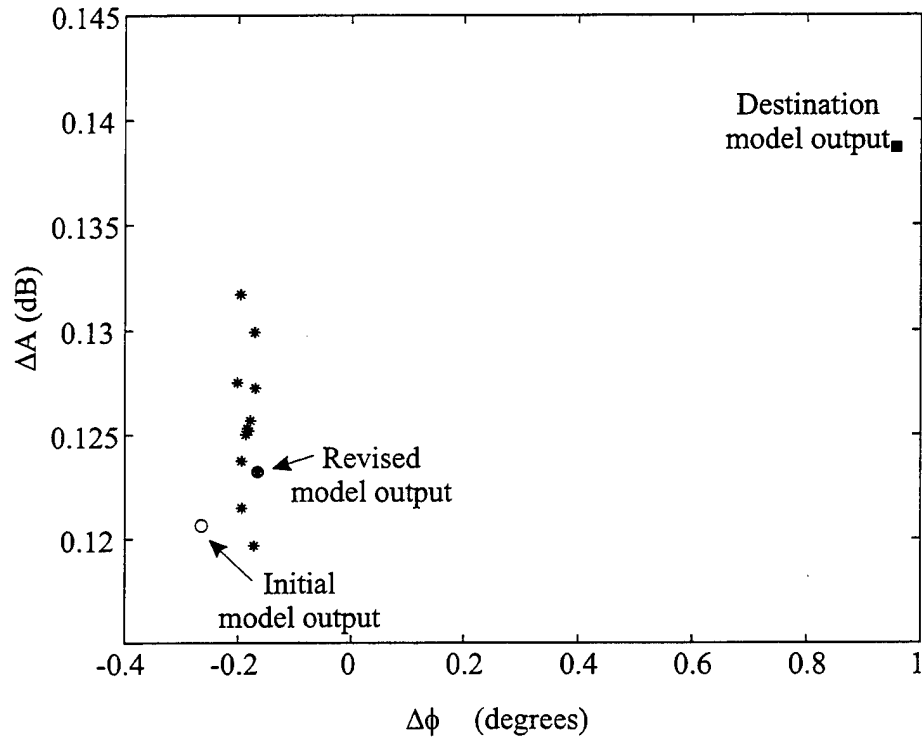


Figure 4.5: For a single VLF signal each iteration corresponds to finding the amplitude and phase change for 12 different collision frequency profiles generated by  $\vec{v}^m \pm \vec{\delta}_j \vec{v}^m$  for  $j = 1, 2, \dots, 6$  and choosing the profile which results in the smallest error value.

	VLF signal	$A^R$ [dB]	$\Delta\phi$ [deg]	$A_{20}^R$ [dB]	$\Delta\phi^{20}$ [deg]
Example 1	$R_1/f_1$	0.15	-0.26	0.14	-0.27
	$R_2/f_2$	-0.01	0.12	-0.01	0.10
	$R_3/f_3$	0.02	0.50	0.02	0.48
Example 2	$R_1/f_1$	0.24	0.53	0.23	0.56
	$R_2/f_2$	-0.04	0.65	-0.04	0.64
	$R_3/f_3$	0.09	0.89	0.10	0.90

Table 4.1: Amplitude and phase changes for the original and regenerated collision frequency profiles.

(Figure 4.7), generally consistent with the range of those expected on the basis of the simplified theory of HF heating described in Section 4.1. The selection of  $\bar{\nu}^0$  is made by using the 3D VLF code with the generic profiles of Figure 4.7 to evaluate the corresponding amplitude and phase changes in the VLF signal closest (in terms of the error function) to the measured values. The initial profiles so chosen are shown in Figure 4.6 and give the closest amplitude and phase changes to the measured values in both examples.

With the initial profile determined from among a finite set which gives the best initial agreement, we proceed with steps 2 through 4 of the inversion algorithm. The final collision frequency profiles obtained after  $m=20$  iterations are shown in Figure 4.6. We note that these profiles are almost identical to the original profiles, and that the amplitude and phase changes corresponding to the regenerated profiles ( $A_{20}^R, \Delta\phi^{20}$ ) are close to the original input values within the measurement limitations as shown in Table 4.1.

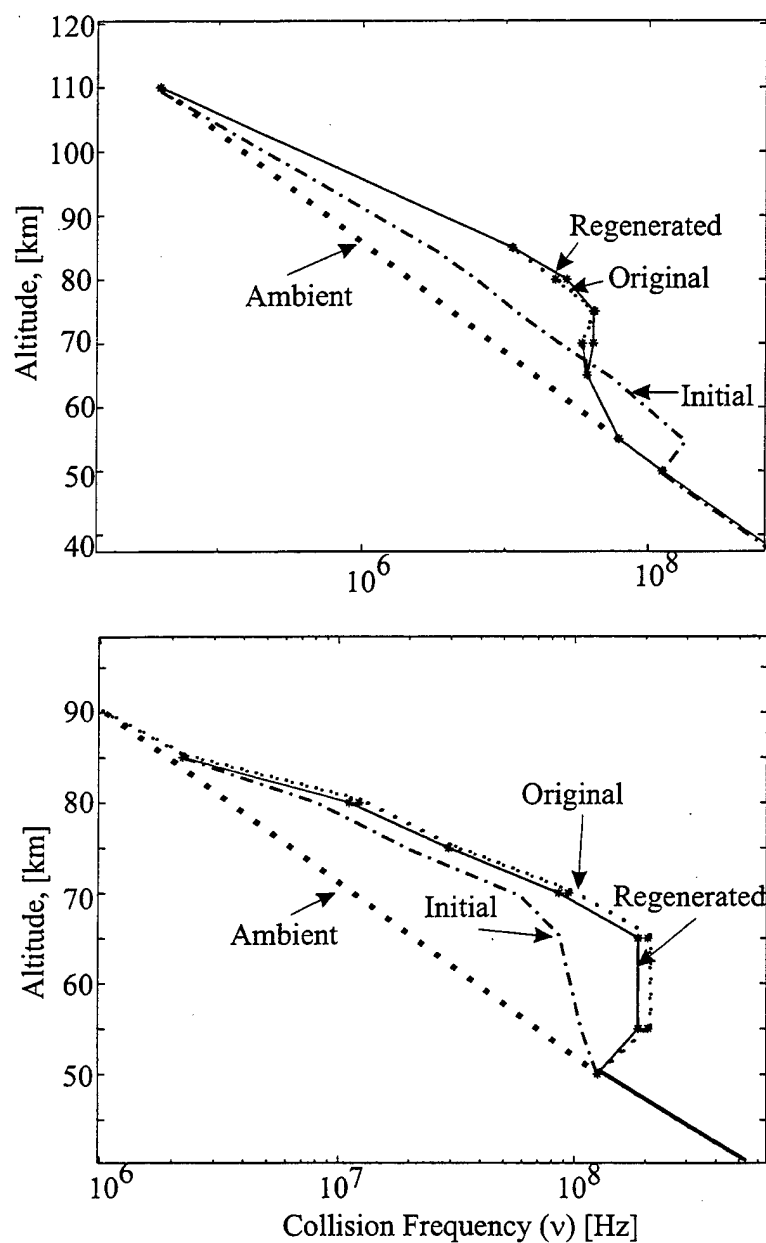


Figure 4.6: Tests of the inversion algorithm. (a) Example 1; (b) Example 2.

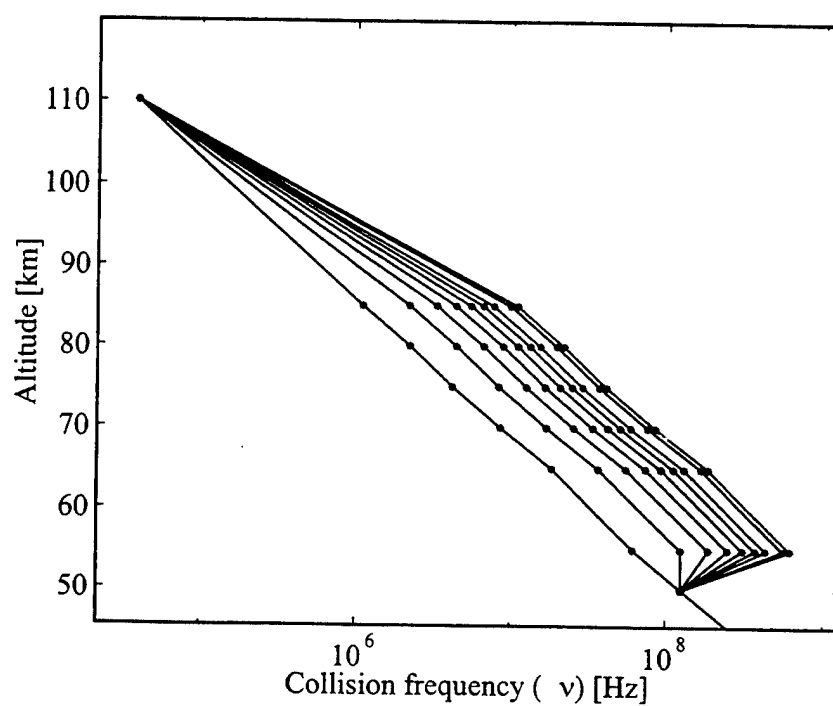


Figure 4.7: Collision frequency profiles used to find the best initial profile to be used in the inversion algorithm.

## Chapter 5

### March 1999 HAARP Campaign

As mentioned previously, the VLF  $D$  region diagnostic technique described in Chapter 4 was developed for the purpose of determining the collision frequency profile in a localized ionospheric patch, as part of the overall suite of diagnostic instruments for the HF Active Auroral Research Program (HAARP). The first opportunity to field test this new diagnostic technique became available in March 1999, where the partially completed HAARP heater was utilized in a month long research campaign. In this Chapter, we describe this campaign and in particular discuss the results obtained with the new VLF  $D$  region diagnostic method.

The HAARP/HIPAS experimental research campaign, conducted in Alaska during March 1999, was a complex undertaking, employing two powerful HF radio transmitters and a variety of radio, radar, and optical diagnostic instruments, located at a number of sites, some in remote areas of the state. A large number and wide variety of experiments were conducted as part of the campaign, carried out during the period of 9-29 March 1999. The HAARP HF transmitter operated on 19 separate days, with a total operation time of approximately 270 hours.

#### 5.1 HAARP Facility Description

Both the HAARP and HIPAS facilities include powerful HF transmitters and a variety of radio and optical diagnostic instruments used to conduct active experimental

investigations to characterize the physical processes that can be initiated and controlled in local regions of the atmosphere, ionosphere and space via interactions with high power radio waves [Kossey and Kennedy, 1999].

The present HAARP HF transmitting system, located in Gakona, Alaska, includes a phased-array antenna, consisting of 48 elements, with crossed dipole antennas driven individually by 10 kW transmitters, resulting in a maximum total radiated power of 960 kW. The HAARP is yet only partially complete. When fully completed in a few years, the HAARP transmitter will consist of 180 antenna elements with a maximum total radiated power of 3.6 MW. Figure 5.1 shows a small section of the HAARP 48 element HF antenna array.

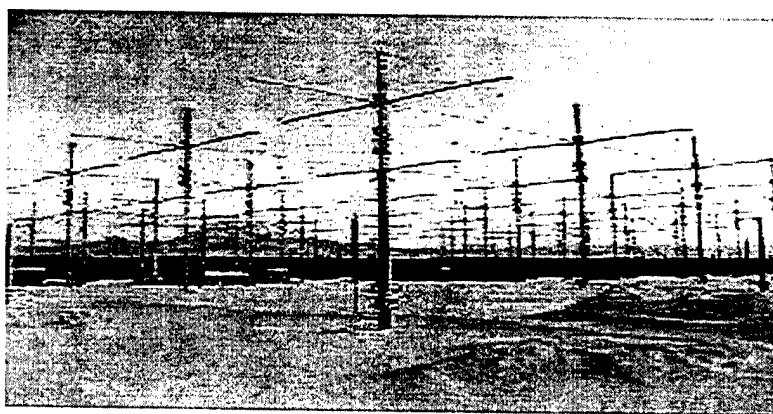


Figure 5.1: The HAARP HF prototype transmitting array.

The HAARP HF transmitter can be operated at any selected and authorized frequency between 2.8 MHz and 10 MHz. It is possible to maximize the deposition of the radiated energy selectively at altitudes between 70 km and 90 km (*D* region of the ionosphere) when operating at 2.8 MHz. At higher frequencies more of the energy is deposited at higher altitudes. Although HAARP operates between 2.8 MHz and 10 MHz, the ionospheric effects it can produce span 16 decades in frequency, from the generation of ULF/ELF waves to the production of optical emissions in the ionosphere. Figure 5.2 lists these physical effects [Kossey and Kennedy, 1999].

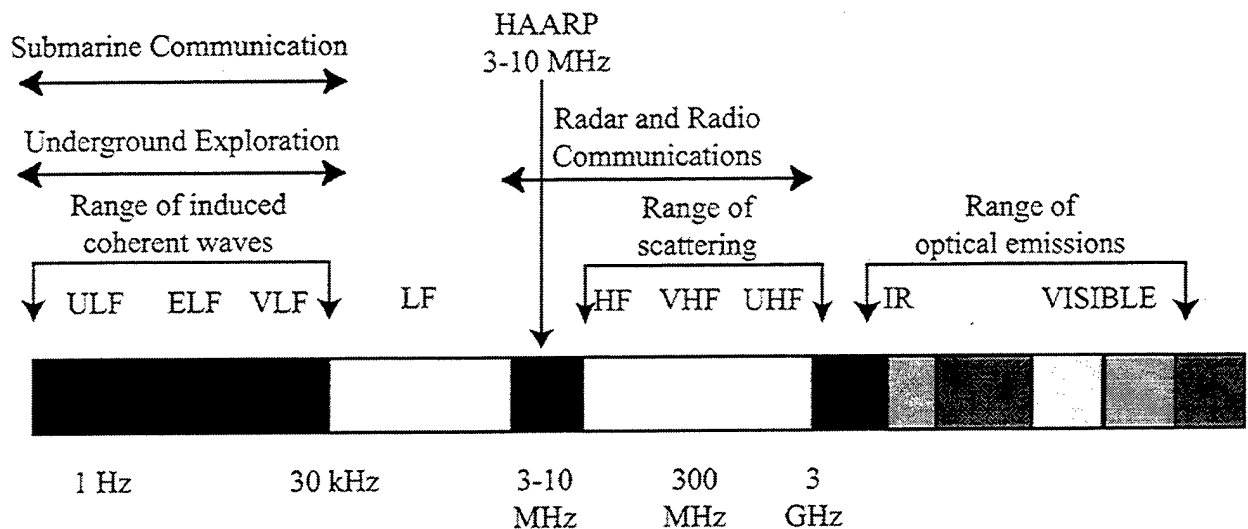


Figure 5.2: Effects spanning 16 decades in frequency produced by HAARP.

The Stanford University VLF D region diagnostic system constitutes only one of the diagnostic instruments built for use with the HAARP facility. The suite of on-site and off-site diagnostic instruments available to the facility play an important role in monitoring the local geophysical and electromagnetic background. They serve an essential role during active experiments employing the HF transmitter, providing knowledge of conditions in the ionosphere and in space prior to, during, and after its operation. Data collected from most of the instruments can be processed and displayed at the site, and can be provided in real-time to other researchers via the Internet. Table 5.1 shows HAARP Diagnostic Instruments [Kossey and Kennedy, 1999].

The HIPAS facility, located near Fairbanks, Alaska, has been in operation for more than a decade. Its HF transmitting system consists of 8 crossed-dipole antennas on a circular field with a diameter of 208 meters. The array has a total radiated power of 1 MW at 2.85 MHz or 4.53 MHz.

VLF <i>D</i> region Diagnostic	
HF vertical incidence sounder	HF SEE receivers
ELF/VLF/LF receivers	Magnetometer
VHF (30 MHz) Riometer	Imaging Riometer
Spectrum Monitor	IR Photometer
HF (28 MHz) radar	VHF (50 MHz) radar
UHF incoherent scatter radar	Optical Imager
Rayleigh LIDAR	UHF scintillation monitors

Table 5.1: List of HAARP Diagnostic tools.

## 5.2 VLF Remote System

During the March 1999 campaign, a VLF *D* region diagnostic system was operated by Stanford University to determine electron temperature changes in the *D* region during active HF heating experiments at the HAARP facility.

The VLF sensor for each receiving system is a square loop antenna with an area of 1.7 m<sup>2</sup>. The signal received by the antenna is amplified by a preamplifier and transmitted down a cable to a VLF line receiver. The output signal from the line receiver is filtered and read by a computer via an A/D card. The amplitudes and phases of the VLF signals from the three transmitters are then extracted and saved [Johnson et al., 1999]. Synchronization in time with the other sites is achieved through the use of a GPS receiver to time stamp the sampled data.

The amplitude and phase of three subionospheric VLF signals propagating through the ionosphere lying over the HAARP facility were measured at three locations in Alaska, namely at Healy, Wasilla and Delta Junction as shown in Figure 5.3. VLF signals from US Navy transmitters in Maine (NAA), Hawaii (NPM), and Washington (NLK) were monitored. At each location the diagnostic system was sited at a local high school. Table 5.2 shows the latitude and longitude of the receivers. Table 5.3 shows the latitudes and longitudes of the transmitters together with the frequency and the power of the radiated VLF signal.

Figure 5.3 shows the location of the receivers and transmitters together with the Great Circle Paths of each VLF signal. Figure 5.4 shows the heated region over HAARP and the receiver sites in expanded detail, illustrating that the locations of



Receiver Name	Latitude	Longitude	High School Name
Healy	63° 52' 22.1" N	149° 00' 49.6" W	Healy High School
Wasilla	61° 35' 16.9" N	149° 25' 58.0" W	Wasilla High School
Delta Junction	63° 59' 59.6" N	144° 44' 00.1" W	Healy Lake High School

Table 5.2: List of VLF receivers used in the VLF Diagnostic System during HAARP 1999 Campaign

Transmitter Name	Latitude	Longitude	Frequency (kHz)	Power (kW)
NLK (Jim Creek, Washington)	48° 12' N	121° 55' W	24.8	850
NAA (Cutler, Maine)	44° 39' N	67° 17' N	24.0	1000
NPM (Lualualei, Hawaii)	21° 25' N	158° 09' N	23.4	300

Table 5.3: List of VLF transmitters used during HAARP 1999 Campaign

the receivers are chosen so that the propagation path of the VLF signals from their respective transmitters pass within 50 km of the heated region over HAARP.

### 5.3 Experimental Results

As part of the March 1999 HAARP campaign, 15 minute nightly periods were allocated for the VLF  $D$  region diagnostic experiment. For this purpose, the HAARP HF output transmissions were 100% amplitude modulated with 25 Hz square waves (i.e., 20 ms ON/20 ms OFF). Figure 5.5 shows an example of the resulting amplitude changes produced in the signals from NPM, NAA and NLK during the HF heating period. The data shown has been averaged through a superposed epoch technique. The right hand panels show the 25 Hz modulation of VLF signals from NPM, NAA and NLK in the time domain. The left hand panels show the peaks at 25 Hz in the Fourier spectrum of the high resolution data. Figure 5.6 shows an example of amplitude and phase changes in the signal from NLK observed at Healy. The 25 Hz modulation is clearly apparent both in the time domain and in the frequency spectra. The peak at 39 Hz in the NPM-Delta Junction spectra is due to local interference, present all the time, regardless of whether HAARP HF transmitter is ON.

The direct association of the observed 25 Hz modulation of the VLF amplitude

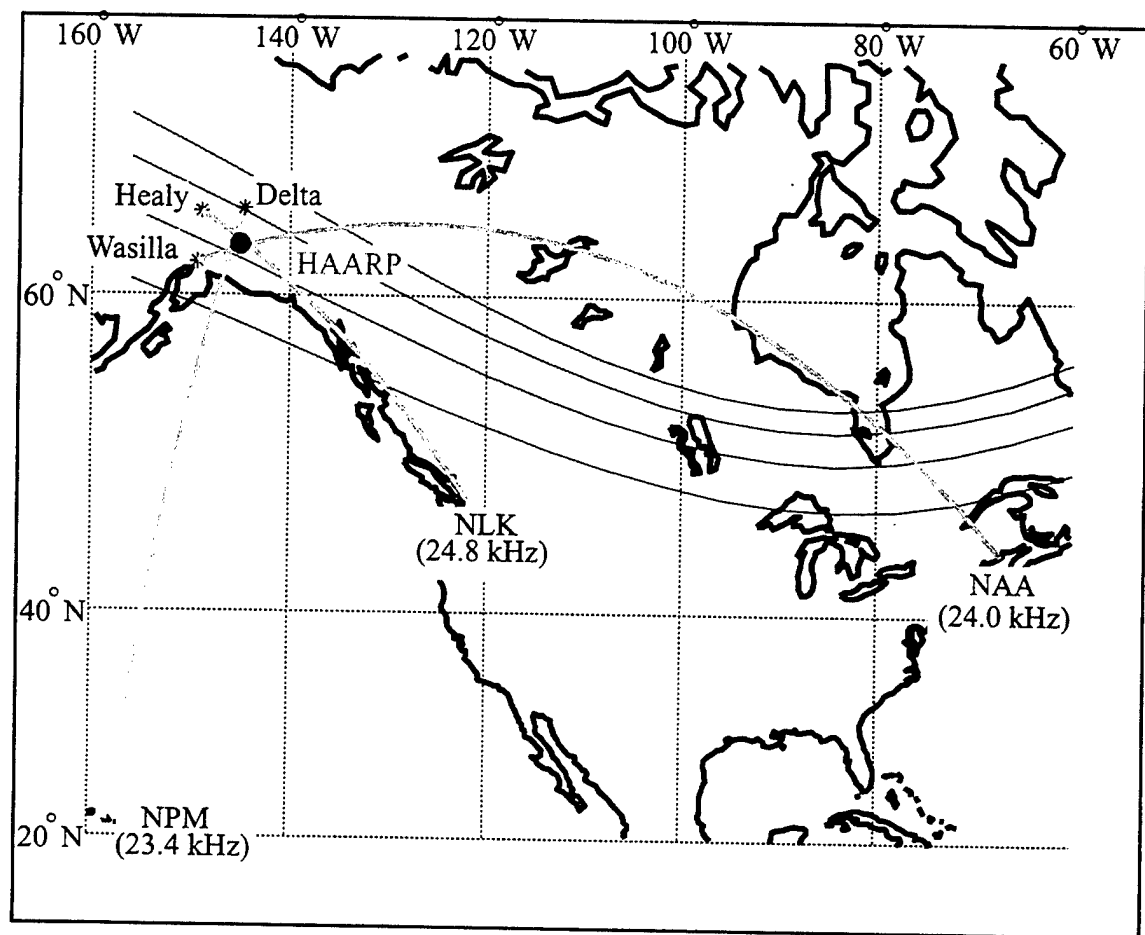


Figure 5.3: VLF transmitter and receiver locations.

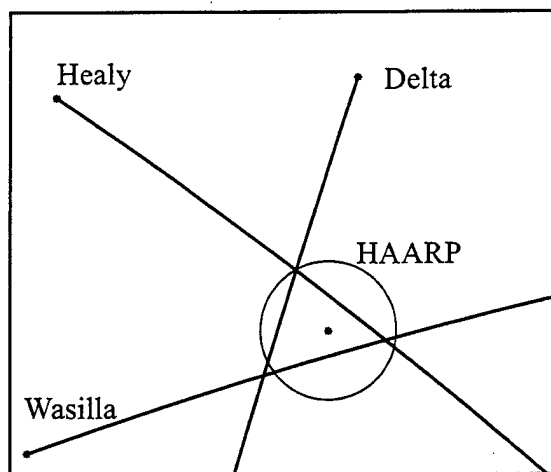


Figure 5.4: Receiver locations with respect to the circular region heated by HAARP. The receivers are located such that the propagation paths of the VLF signals pass through the heated region.

and phase with HAARP transmissions is further illustrated in Figure 5.7 where the spectrum of the VLF amplitude is plotted for 5 sequential 5-min periods, the first being before the 25 Hz modulation of HAARP is turned ON, the next three being during which HAARP is ON and the last being immediately after HAARP is turned OFF. It is clear that 25 Hz is only present when HAARP is ON and that the level of transferred modulation remains approximately constant during the 15 minute period. The HAARP VLF *D* region diagnostic format was transmitted nearly every night during the March 1999 campaign, and VLF data was acquired at all three sites, almost every night. The results of the VLF measurements are summarized in Tables 5.4 through 5.6. In each Table are shown the measured absolute amplitude  $A$  (average value over 15-min period in dB above  $1 \mu\text{V/m}$ ) of the corresponding VLF signal, the amplitude change  $\Delta A$  (in dB above  $1 \mu\text{V/m}$ ), the signal-to-noise ( $\text{SNR}_{\text{amp}}$ ) ratio defined as the ratio of the value of the spectral density at 25 Hz to the average value of spectral density in the 15-35 Hz range, the phase change  $\Delta\phi$  (in degrees), and the phase signal-to-noise ( $\text{SNR}_{\text{phs}}$ ) defined as the ratio of the value of the spectral density of the phase at 25 Hz to its average value in the 15-35 Hz range. The Table for the

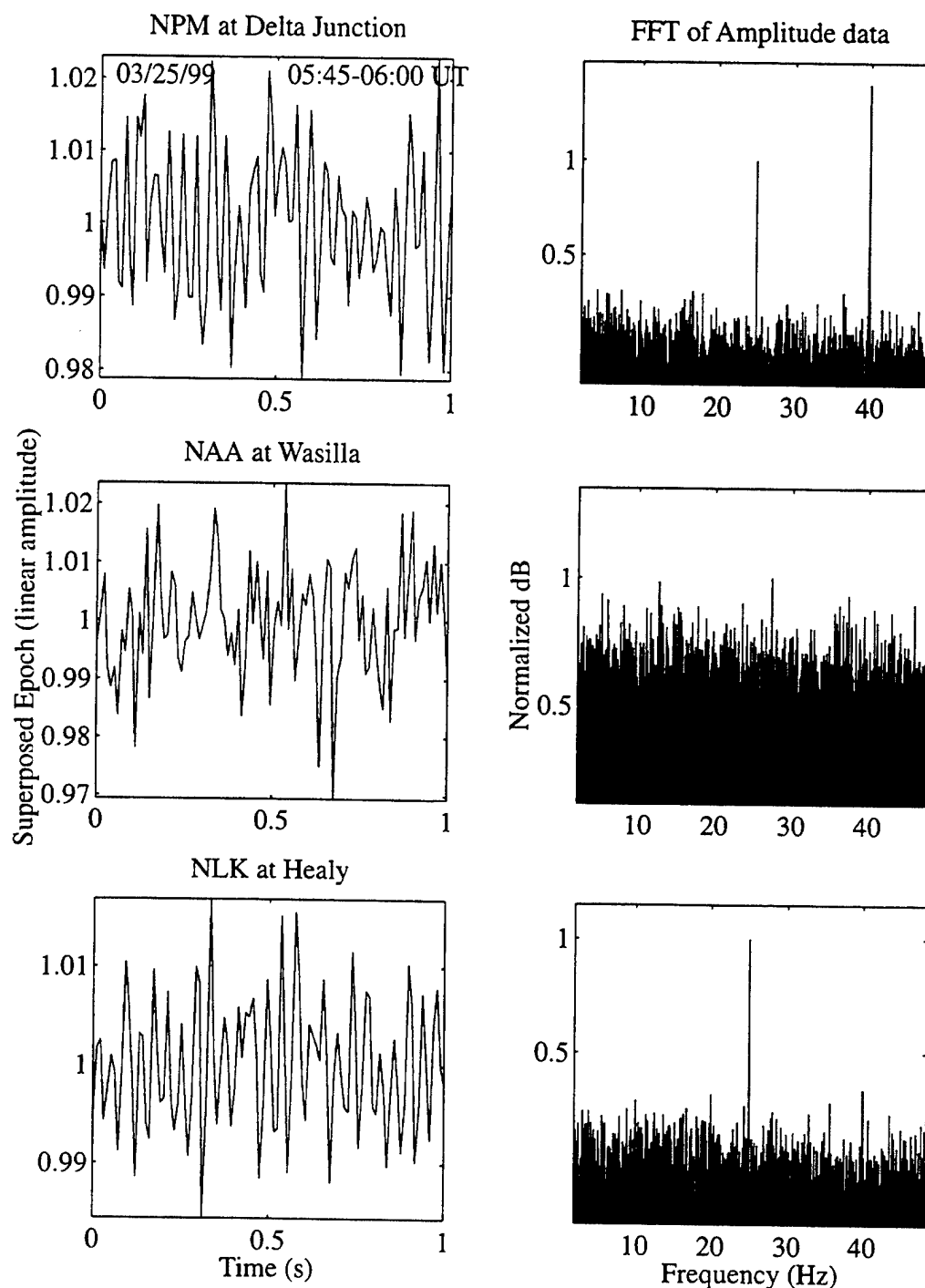


Figure 5.5: Superposed epoch analysis results and spectra of the NPM, NAA and NLK signal amplitudes observed at Delta Junction, Wasilla and Healy respectively, between 05:45-06:00 UT on 03/25/1999. The 25 Hz modulation is apparent on the NLK and NPM signals. The peak at 39 Hz on the NPM signal is due to local interference.

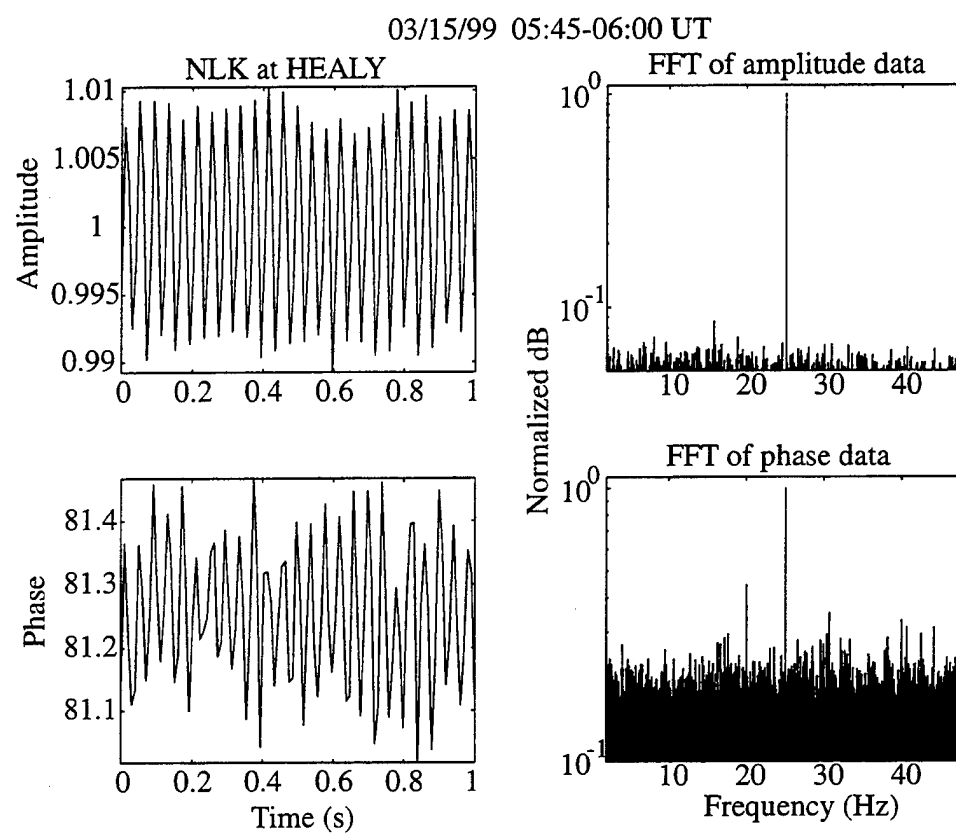


Figure 5.6: Amplitude and phase modulations of the VLF signal from NLK as received at Healy. A 25 Hz modulation is clear both in the time and frequency domains.

NPM signal measured at Delta Junction is short since the NPM VLF transmitter in Lualuelai, Hawaii was undergoing maintenance (and hence not operational) through most of the March 1999 campaign.

The HAARP VLF D region diagnostic system was originally designed for the fully developed HAARP HF heater, planned to be operating at a total radiated power level of 3.6 MW. Accordingly, the range of results obtained (Tables 5.4–5.6) during the March 1999 campaign, conducted at a radiation power level of 960 kW, are indeed quite encouraging, even though the signal-to-noise ratios were marginal ( $\text{SNR} \simeq 1$ ) in a number of days and were too low ( $\text{SNR} < 1$ ) in others. Unfortunately, for many of the days during the campaign the VLF transmitter NPM was not operational, as mentioned above. On days when NPM was operating, the SNR at one or more of the stations was too low. Thus, it was not possible to measure detectable amplitude and phase changes simultaneously on VLF signals from three different propagation paths. Accordingly, the range of data available only allowed application testing of the VLF diagnostic in a case involving simultaneous observation of two identifiable amplitude and phase changes on two different signals. The application of the inversion algorithm to the VLF observations for this case is described in the next section.

## 5.4 Example Inversion of VLF data from 25 March 1999

The last 3 days of the campaign are the only days with VLF amplitude and phase data from all of the 3 VLF transmitters, but as mentioned above, the SNR of the NAA signal was too low. We now apply the VLF *D* region diagnostic method to one of the few days, namely 3/25/99, for which amplitude/phase changes were observed (with  $\text{SNR} > 1$ ) on two VLF signals in order to present a step-by-step description of the inversion procedure.

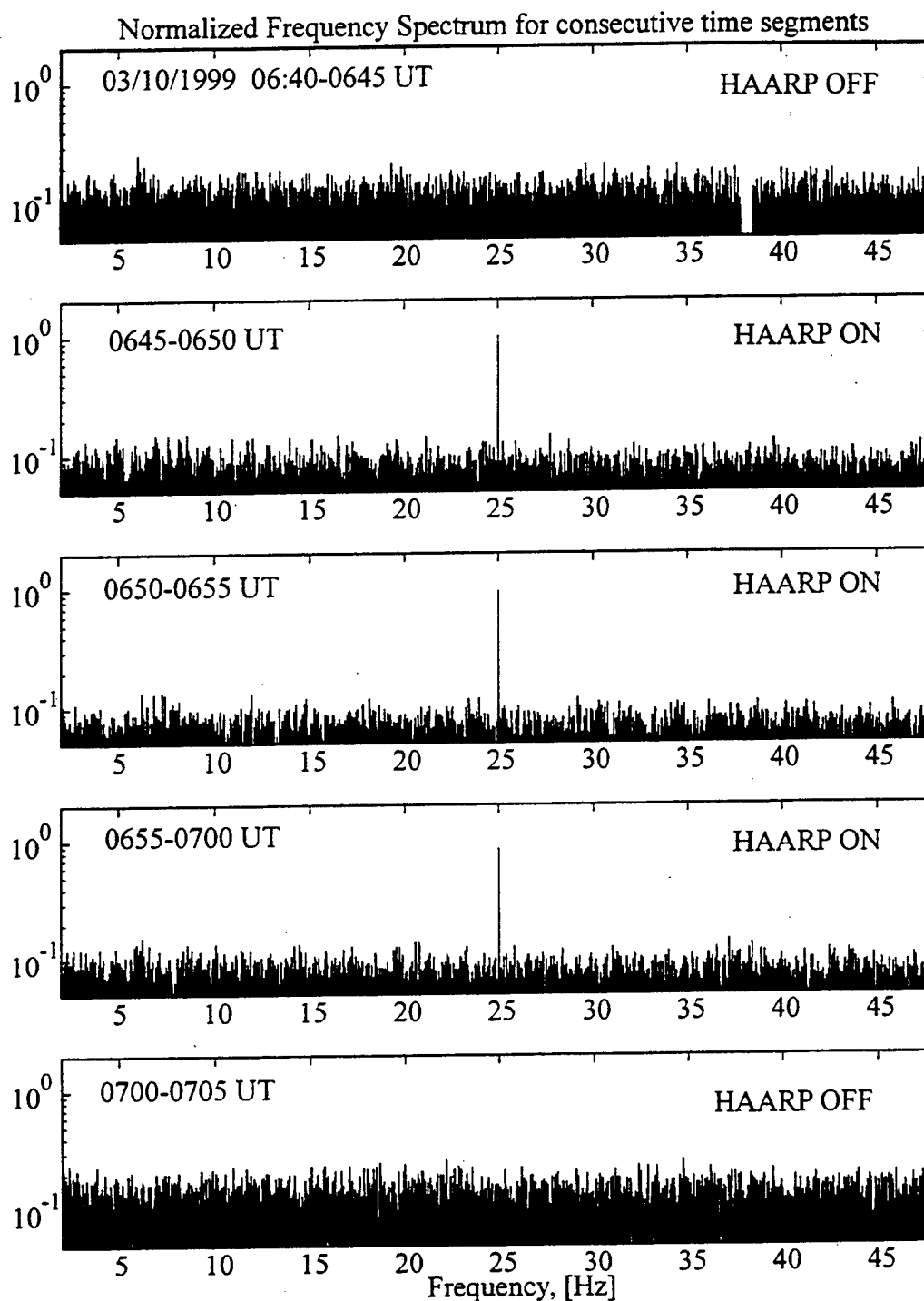


Figure 5.7: NLK amplitude spectrum from 06:40 to 07:05 in 5 minute intervals on 03/10/1999. It is clear that the amplitude modulation is due to HAARP.

UTC Date	UTC Time	NLK A (dB above $1\mu\text{V/m}$ )	$A^R$ (dB)	$\text{SNR}_{\text{amp}}$	$\Delta\phi$ (deg)	$\text{SNR}_{\text{phs}}$
3/09/99	0645-0700	66.75	0.28	25.78	0.08	1.04
3/10/99	0645-0700	68.65	0.21	41.73	0.18	4.30
3/11/99	0445-0500	70.72	0.03	5.44	0.26	6.51
3/15/99	0545-0600	70.65	0.16	53.00	0.30	13.53
3/16/99	0645-0700	67.01	0.17	13.16	2.14	21.42
3/17/99	0645-0700	69.57	0.10	16.81	0.48	11.73
3/18/99	0645-0700	72.18	0.18	27.28	1.64	2.27
3/19/99	0545-0600	67.95	0.04	2.98	1.40	16.45
3/20/99	0545-0600	67.73	0.05	8.13	0.32	7.66
3/22/99	0545-0600	69.11	0.04	6.25	1.08	28.66
3/23/99	0545-0600	70.56	0.08	10.55	0.58	10.72
3/24/99	0645-0700	No Data	-	-	-	-
03/25/99	0545-0600	66.83	0.14	9.89	0.96	8.50
03/26/99	0745-0800	70.19	0.00	0.52	0.04	0.90
03/27/99	0845-0900	72.69	0.01	2.03	0.40	20.98

Table 5.4: List of the amplitude and phase measurements at Healy.

UTC Date	UTC Time	NAA A (dB above $1\mu\text{V/m}$ )	$\Delta A$ (dB)	$\text{SNR}_{\text{amp}}$	$\Delta\phi$ (deg)	$\text{SNR}_{\text{phs}}$
03/09/99	0645-0700	No Data	-	-	-	-
03/10/99	0645-0700	65.00	0.02	1.72	0.10	1.02
03/11/99	0445-0500	67.21	0.01	1.06	0.16	2.31
03/15/99	0545-0600	66.13	0.02	1.29	0.12	1.49
03/16/99	0645-0700	67.18	0.03	2.18	0.10	1.34
03/17/99	0645-0700	72.52	0.01	1.10	0.08	2.21
03/18/99	0645-0700	72.41	0.01	1.02	0.12	2.89
03/19/99	0545-0600	69.96	0.01	1.21	0.10	2.02
03/20/99	0545-0600	62.16	0.04	2.14	0.24	1.75
03/22/99	0545-0600	72.75	0.02	3.17	0.08	2.63
03/23/99	0545-0600	66.64	0.01	0.56	0.08	0.95
03/24/99	0645-0700	72.58	0.00	0.19	0.02	0.43
03/25/99	0545-0600	69.73	0.01	0.54	0.10	2.03
03/26/99	0745-0800	74.65	0.01	1.23	0.48	0.30
03/27/99	0845-0900	76.10	0.00	0.49	0.04	1.38

Table 5.5: List of the amplitude and phase measurements at Wasilla.



UTC Date	UTC Time	NPM $A$ (dB above $1\mu\text{V/m}$ )	$\Delta A$ (dB)	$\text{SNR}_{\text{amp}}$	$\Delta\phi$ (deg)	$\text{SNR}_{\text{phs}}$
03/09-24/99	Various	Transmitter OFF	-		-	
03/25/99	0545-0600	69.78	0.01	1.16	-7.42	0.87
03/26/99	0745-0800	71.51	0.00	0.51	0.02	0.75
03/27/99	0845-0900	70.81	0.00	0.29	0.06	1.33

Table 5.6: List of the amplitude and phase measurements at Delta Junction.

### 5.4.1 Data Selection and Calibration

The VLF amplitude and phase data from NLK and NPM received on 3/25/99 respectively at Delta Junction and Healy are shown in Figure 5.8. The NAA signal at Wasilla did not exhibit any detectable changes as indicated in Table 5.5. We see that both NLK-Healy and NPM-Delta Junction signals clearly show the 25 Hz modulation. (NLK amplitude shows another peak at  $\sim 39$  Hz, which is due to local noise and is visible during other periods when the HAARP transmitter was not operational.)

For comparison, the spectra of both raw data and the superposed epoch analysis for the NAA-Wasilla signal are shown in Figure 5.9. There is no clear peak at 25 Hz showing any indication of HAARP modulation.

A block diagram representation of the VLF receiver at each site is shown in Figure 5.10. In order to compare the recorded VLF values with LWPC calculations (which give the value of the vertical electric field measured at the receivers), it is necessary to determine the amplitude of the vertical electric field measured at each site in  $\mu\text{V/m}$ . In our experiment, we utilize vertically deployed magnetic loop antennas which measure the horizontal magnetic field, simply related to the electric field, i.e.  $E_{\text{in}} = cB_{\text{in}}$ , where  $c$  is the speed of light. The measured units generated by the receiver ( $D_{\text{out}}$ ) is eventually expressed in terms of the equivalent field strength ( $E_{\text{in}}$ ).

The overall transfer function,  $D_{\text{out}}/E_{\text{in}}$  consists of three gain stages:

- $V_{\text{in}}/E_{\text{in}}$ , the gain of the antenna with respect to the effective input electric field strength. The effective field  $E_{\text{in}}$  has the value  $E_{\text{in}} = cB_{\text{in}}$ , where  $B_{\text{in}}$  is the magnetic field measured by the loop. The gain of the air-core loop antenna used in the Stanford VLF receivers is  $\sim 1.88$ .

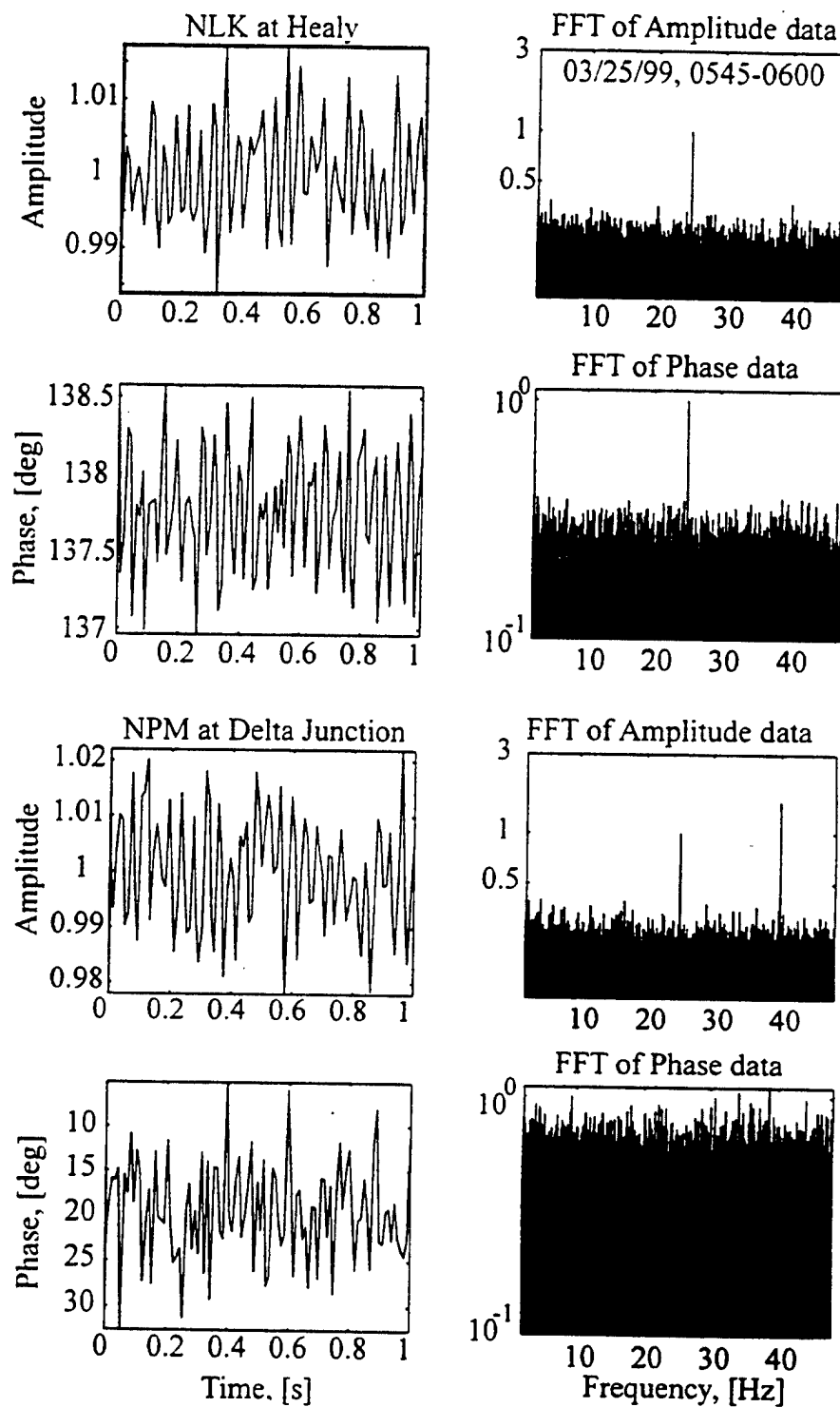


Figure 5.8: On the left panels, superposed epoch analysis of amplitude and phase data from NLK and NPM are shown. On the right panels, the spectra of the respective data are shown.

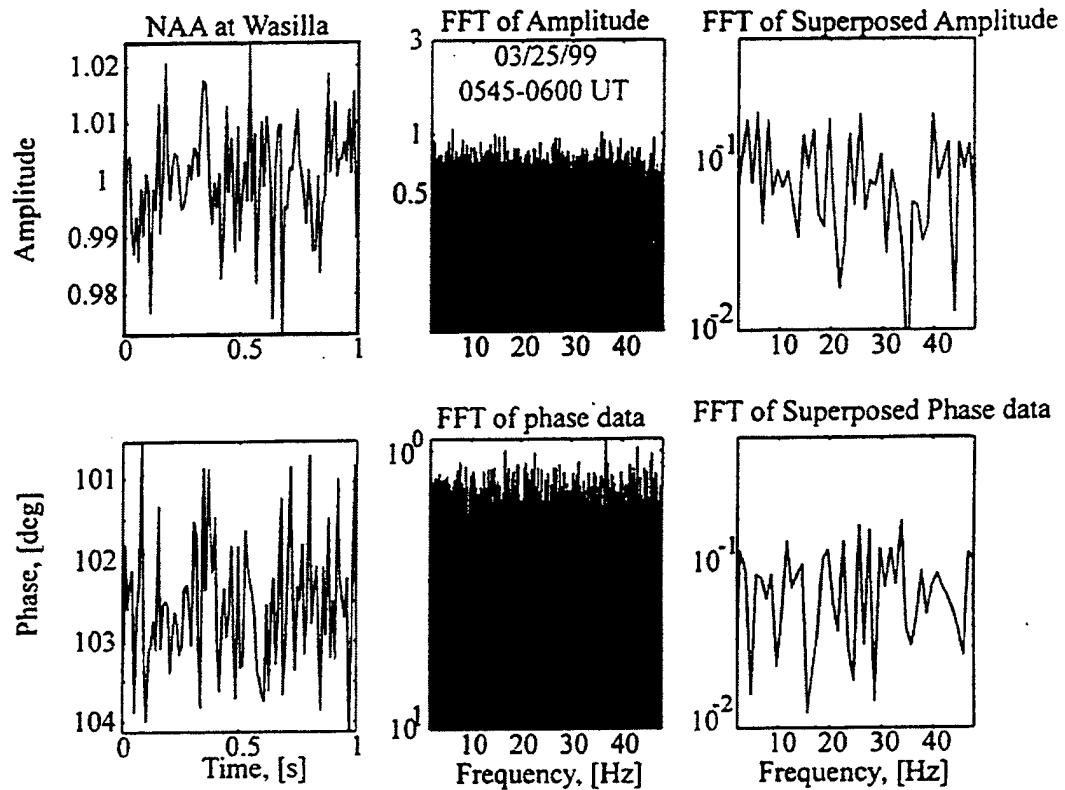


Figure 5.9: NAA amplitude shows no 25 Hz modulation on 03/25/1999.

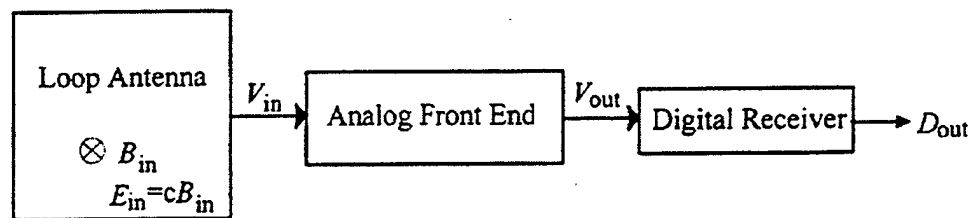


Figure 5.10: The overall transfer function  $D_{out}/E_{in}$  consists of three transfer functions, gain of the antenna, gain of the analog front end, and gain of the digital receiver.

- $V_{\text{out}}/V_{\text{in}}$ , the gain of the analog front end. This gain depends on the frequency of the VLF signal being received. In order to determine the analog front end gain, a dummy loop consisting of a lumped circuit with terminal impedance identical to the input impedance of the loop antenna is connected to the antenna terminals. A voltage  $V_{\text{in}}$  is then injected by a function generator, and the voltage at the output of the analog front end is measured at selected frequencies. From these measurements plots of the analog gain vs frequency are generated, which can be used to find the gain at any frequency by interpolation. Figure 5.11 shows this calibration plots for 3 different receivers.
- $D_{\text{out}}/V_{\text{out}}$ , the gain of the digital receiver. This gain mainly depends on the dynamic range of the A/D card used and the representation of the digital numbers. In our case, the A/D card has an input range of  $\pm 5\text{V}$  and the values are recorded as 16 bit unsigned integers, which gives a digital gain of  $2^{16}/10$ .

Further details on the operation and calibration of the narrowband system used in the Stanford VLF receivers can be found at <http://www-star.stanford.edu/~hail/>.

#### 5.4.2 The Ambient Electron Density Profile

Once the measured VLF amplitudes are converted to field values in  $\mu\text{V}/\text{m}$ , the next step is to determine the ambient electron density profile for which 2D LWPC calculations as described in Chapter 3 produce approximately the same measured values. For this step the collision frequency profile is assumed to be a constant standard profile (Figure 1.3-b) throughout the propagation path for all 3 different receivers, and the electron density profile is assumed to be described by a Gaussian flux model described in Chapter 3. The determination of the ambient electron density profile relies upon a stored data file which contains the absolute ( $\mu\text{V}/\text{m}$ ) values calculated with the 2D LWPC code for different models which is used to select the best fit to the measured values as the ambient electron density profile. A computer program written for this purpose reads in the data file, finds the best fit, and automatically generates the LWPC model input files (see Section 2.1) for three different propagation paths for the next steps. Figure 5.13 illustrates the segmentation of the propagation path

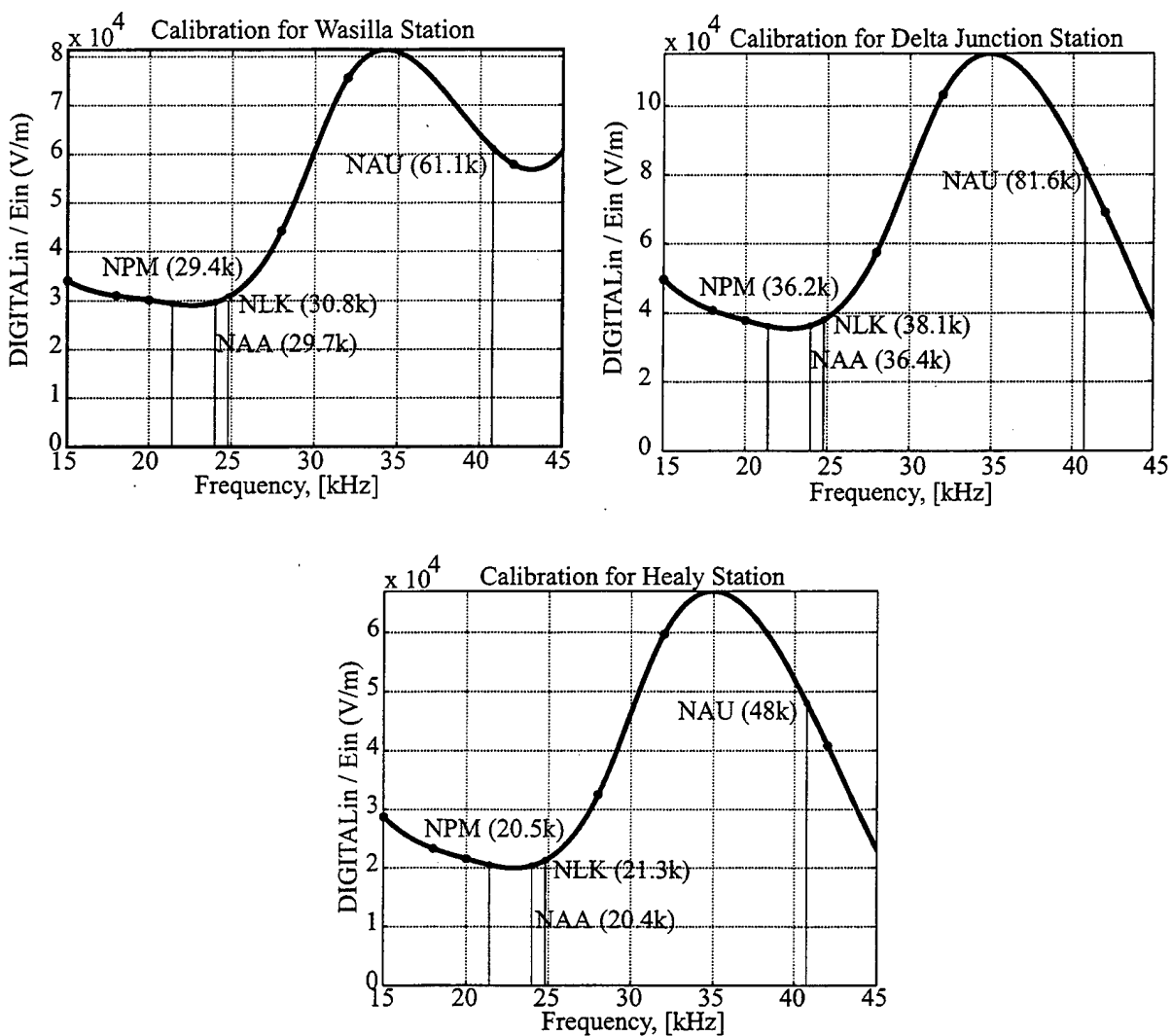


Figure 5.11: Calibration plots for the receivers at Wasilla, Delta Junction and Healy.

into segments having different electron density profiles. Figure 5.12 shows the electron density profiles that are used in generating the stored data file.

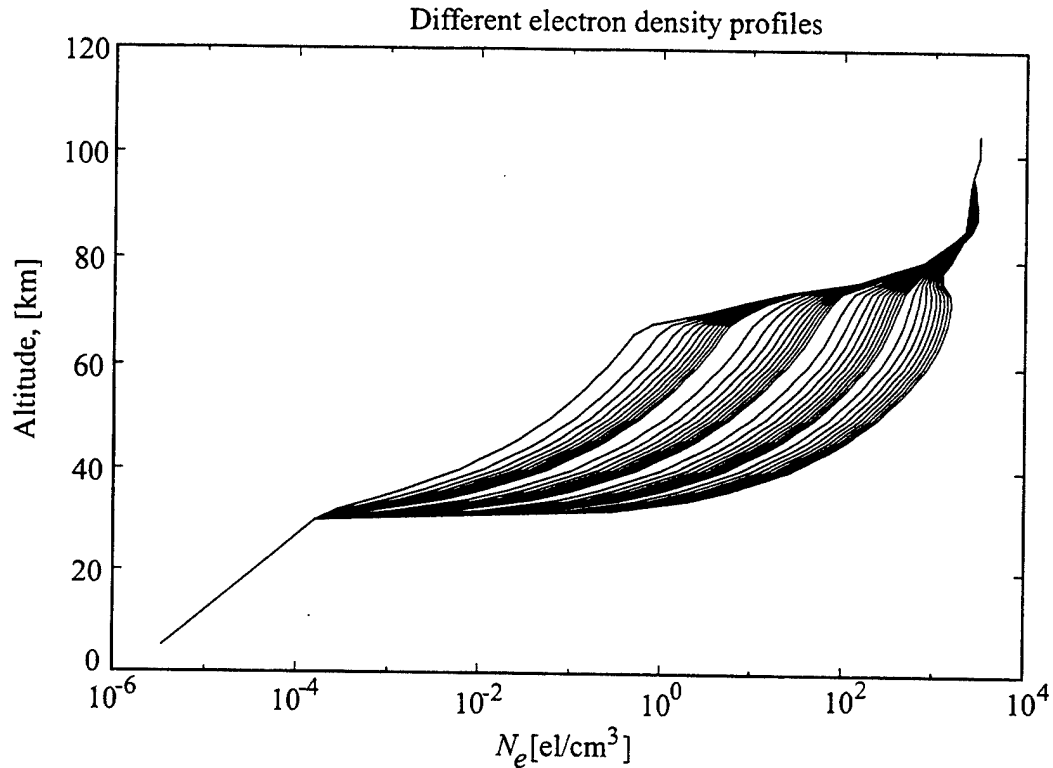


Figure 5.12: Different electron density profiles used in the modeling of the Gaussian spatial distribution centered at  $L = 6$ .

Following the procedure described above, and using the field values (in  $\mu\text{V/m}$ ) measured at three different sites, the best Gaussian model for the electron density is found. The measured field values (normalized by the power levels of the transmitters) and the values produced by 2D LWPC code for the electron density profile determined in this was are given in Table 5.7. Note that the NAA-Wasilla data was not included in this determination since the signal-to-noise ratio for this case was less than unity.

The electron density profiles corresponding to the different segments shown in Figure 5.13 are plotted in Figure 5.14. As indicated in Chapter 4, the electron density profile in the  $D$  region of the ionosphere can be assumed to be constant during

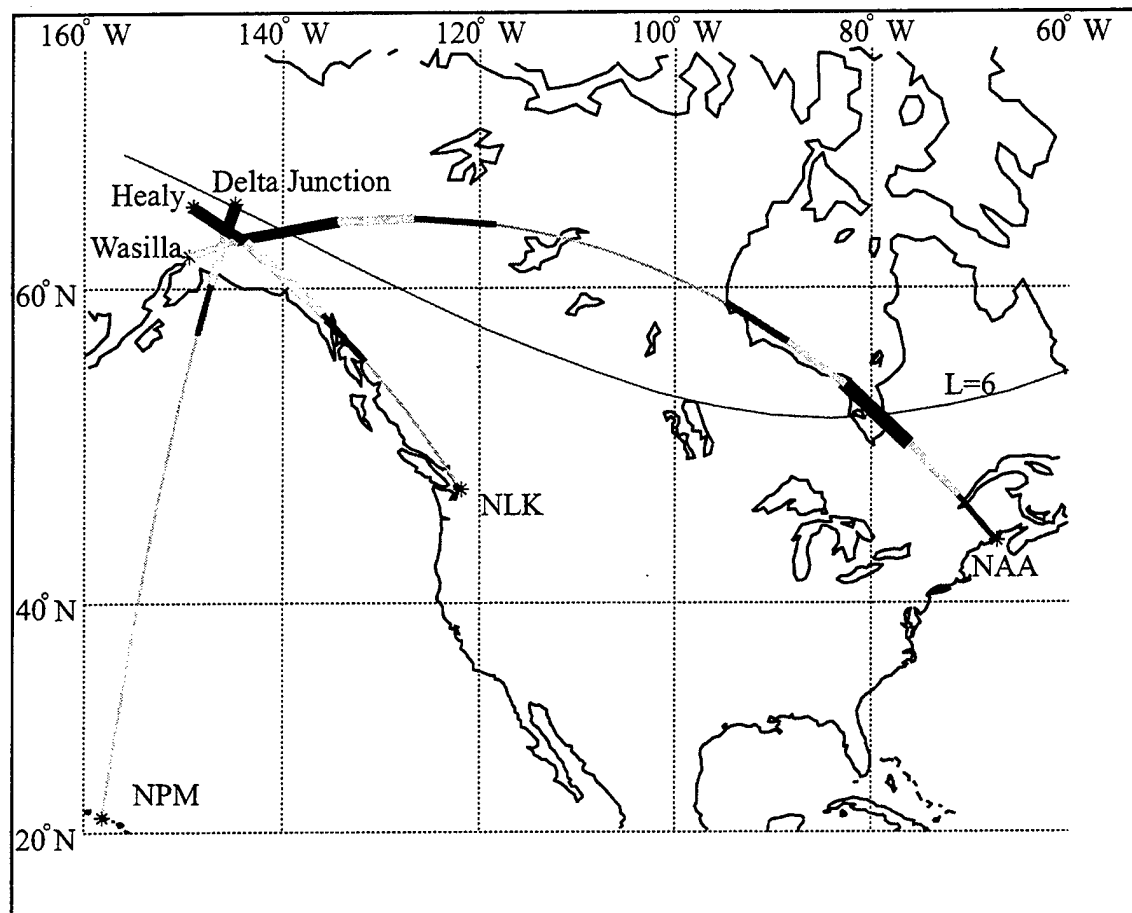


Figure 5.13: The GCP paths of the three VLF signals are divided into segments where the electron density profiles are different and correspond to a Gaussian flux level model as described in Chapter 3.

	Measured field value (dB above $1\mu\text{V/m}$ )	Gaussian Model Result (dB above $1\mu\text{V/m}$ )
NLK	34.02	34.27
NPM	31.61	31.43

Table 5.7: The measured values of the transmitter signals at the receivers and model results.

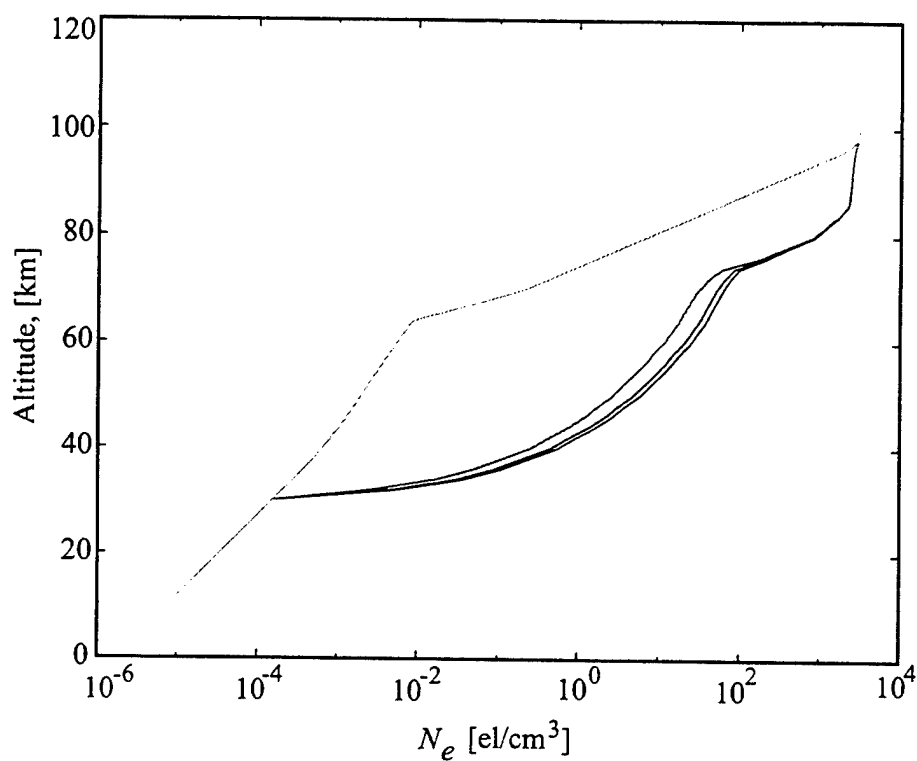


Figure 5.14: Different electron density profiles shown here are plotted in the same color as the segments of the propagation paths where they are used to model the ionosphere.



HAARP modulation. Thus the profiles shown in Figure 5.14 are used in the later steps and specifically in the next section.

### 5.4.3 The Modified Collision Frequency Profile

The disturbed collision frequency profile is determined using the inversion algorithm explained in Chapter 4. It is first necessary to identify an initial guess for the six parameters that describe the disturbed collision frequency profile. For this purpose, we select the one profile (from among a prescribed set as described in Chapter 4) which gives the amplitude and phase changes closest to the measured ones. The initial profile selected in this way is indicated in Figure 5.16.

With the initial profile so determined, the final step is to use the inversion algorithm described in Chapter 4. The iterations for the NLK amplitude and phase are shown in Figure 5.15 in the same format as in Figure 4.5. The final collision frequency profile is shown in Figure 5.16 as a solid line.

It is interesting to note that the final profile that we arrive at with the inversion method is substantially different from the theoretical profile calculated using the simple theory of HF heating described in Section 4.1. The inferred profile (i.e., that which is marked "final" in Figure 5.16) indicates that the electron collision frequency is enhanced by nearly an order of magnitude at 90 km altitude and by nearly a factor of 30 at 80 km altitude. The sharp variations in the profile below  $\sim 75$  km altitude are probably not real, and may be an artifact of the fact that we have used only four measurements (i.e., two VLF signals) to characterize a 6-parameter profile. This observation underscores the need to use at least 6-parameters to characterize the disturbed collision frequency profile, as the Stanford VLF *D* region diagnostic system is designed for. Nevertheless the maximum heating does appear to occur near 80 km altitude, a result which may be a manifestation of the HAARP HF frequency used for heating on this day (2.87 MHz). Follow-on heating experiments at other HF frequencies may further clarify the manner in which HF heater energy is actually deposited in the lower ionosphere.

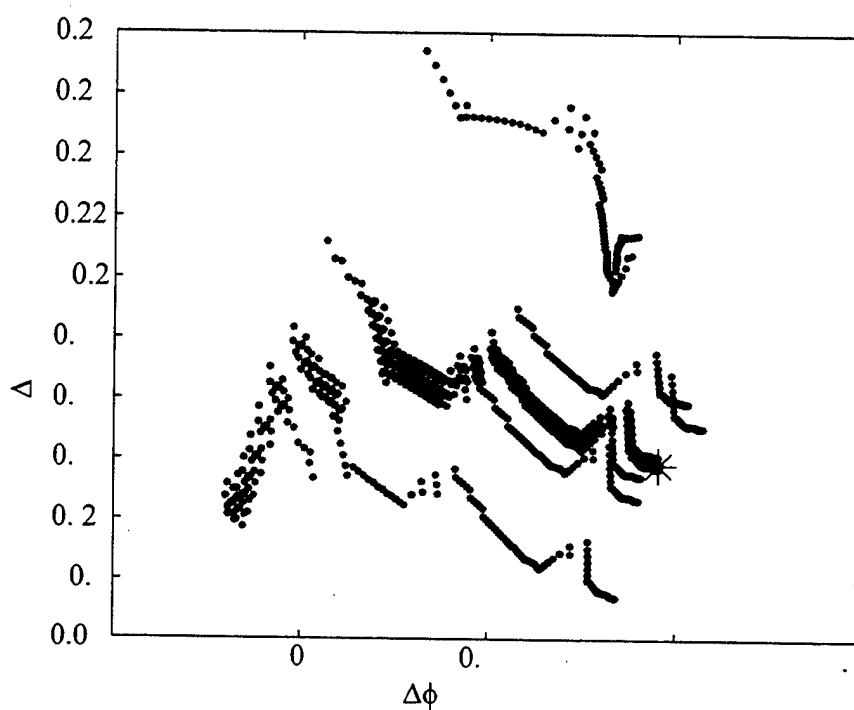


Figure 5.15: Amplitude and phase change pairs arrived at in different steps  $m$  of the iterative inversion process. The measured amplitude and phase change is shown by the circle.

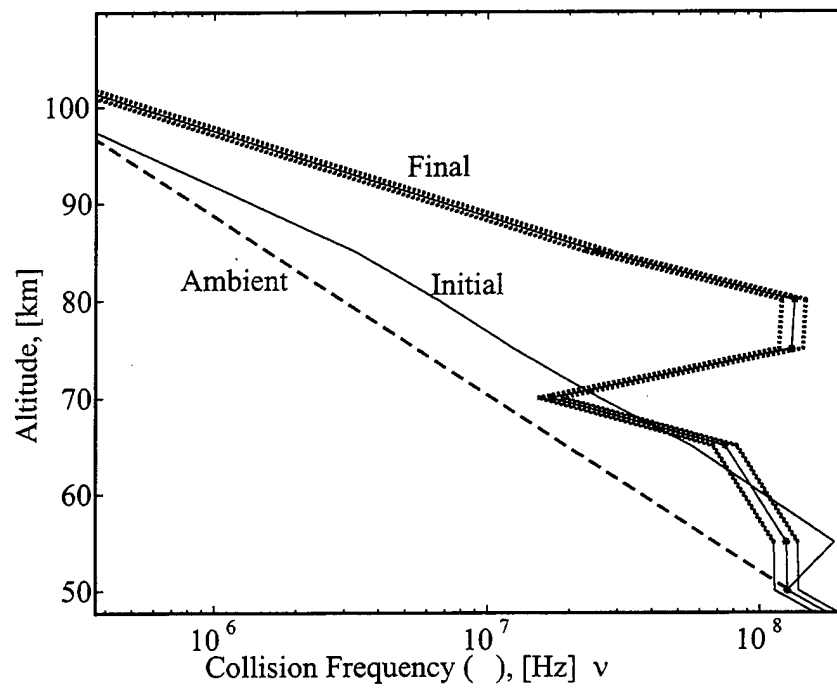


Figure 5.16: Collision frequency profile used as an initial estimation, the final profile generated at the end of the inversion, and the theoretically expected profile is shown.

## Chapter 6

# Summary and Suggestions for Future Work

### 6.1 Summary

We have developed a new method for determination of the electron collision frequency profile within a localized region of the ionosphere modified in a transient manner by radiowave heating, via inversion of measurements of associated subionospheric VLF signal changes. Localized disturbances in the  $D$  region of the ionosphere are routinely produced by powerful HF transmitting facilities such as the High Power Auroral Stimulation (HIPAS) facility and the High Frequency Active Auroral Research Program (HAARP), as well as by lightning discharges. The new VLF diagnostic method which is the subject of this dissertation takes advantage of the fact that electron density and temperature changes in the  $D$  region are sensitively manifested in changes in the amplitude and phase of subionospheric Very Low Frequency (VLF) signals propagating beneath the perturbed region.

Amplitude and phase changes of VLF waveguide signals scattered from artificially heated ionospheric patches can be measured with appropriately placed VLF receivers. The new inversion algorithm is designed to determine the altitude profile of electron collision frequency within the patch by using the measured amplitude and phase of three different VLF signals at three separate frequencies. The algorithm is primarily

based on the recursive application of the three dimensional version of the Long Wave Propagation Capability (LWPC) code used to model the subionospheric propagation and scattering of VLF signals in the earth-ionosphere waveguide in the presence of ionospheric disturbances. The amplitude and phase changes at each receiver produced by different collision frequency profiles were found to be detectably different from each other even though the measured signals spanned a narrow range of frequency (24-25 kHz), and the inversion algorithm was successfully utilized to determine the modified collision frequency profile.

The new algorithm is applied to experimental data acquired during March 1999, when a VLF *D* region diagnostic system was operated in Alaska in association with an ionospheric heating campaign. The aim of the experiment was to determine electron collision frequency and temperature changes in the *D* region, during active HF heating experiments conducted with the HAARP facility. For this purpose, the HF (2.87 MHz) transmissions from the HAARP system were 100% amplitude modulated with a 25 Hz square wave (ON/OFF) pattern, for 15-minute periods each night. The transfer of this modulation to the VLF signals passing through the heated region was detected through amplitude and phase changes produced in the signal from NPM, NAA and NLK, using a superposed epoch analysis of data acquired during the same 15 minutes. The HAARP 25 Hz modulation was clearly apparent both in the time domain and frequency domain for most of the days on at least one of the NPM, NLK or NAA transmitter signals. The inversion algorithm for both finding the ambient electron density profile and the modified collision frequency profile was applied successfully to the available data.

The altitude profile of electron collision frequency produced by an HF ionospheric heater depends sensitively on the electron density profile in the lower ionosphere. For this purpose, we have shown that it is possible to take advantage of a newly observed association between relativistic electron enhancements and nighttime *D* region electron density [Demirkol *et al.*, 1999], to model propagation of VLF waves in subauroral regions, and to assess the ambient electron density profile from measured values of VLF signal amplitudes. We were thus able to determine the ambient electron density profile along the propagation path of the VLF signals for the HAARP March

1999 experiment, prior to applying the inversion algorithm for determination of the collision frequency profile.

## 6.2 Suggestions for Future Work

### 6.2.1 Improved Electron Density Model

Determination of the ambient electron density profile is a necessary step for inferring the modified collision frequency profile in a disturbed region of ionosphere by an HF heater. In this work, the ambient electron density profile on the propagation path of the VLF signal was assumed to be modulated by relativistic electron precipitation flux level. Since the latitude range that was of interest was in the subauroral regions where the precipitation events frequently take place, the Gaussian modeling of the spatial distribution of the flux level was applied successfully. However, in the determination of a Gaussian model which would best fit the measured VLF signal levels, only the amplitude of the VLF data was used for comparison. Thus 2 unknown parameters (the width and the peak of the Gaussian) were determined by 3 amplitude measurement of VLF signal. In the future, the additional use of VLF phase data may allow us to relax some of the fixed parameters in the current model (such as the center of the Gaussian distribution) allowing for more flexible modeling of the electron density profile. An alternative method would be inferring the ambient electron density profile using an inversion method similar to described in Chapter 4, with 6 measurements and six degrees of freedom.

### 6.2.2 Future Experiments

Results from March 1999 HAARP campaign were encouraging for the future utilization of the *D* region VLF diagnostic system. Although the VLF diagnostic system was designed for use with full power operation of the HAARP facility, it was possible to observe amplitude and phase modulations in many cases with very reasonable signal-to-noise ratio. When the HAARP heating facility is fully functional, measurements and phase changes with substantially higher SNR will be available from each of the

three receiver sites, making the diagnostic system more effective. It is also possible to increase the number of received VLF signals in order to increase the number of free variables in the modeling of the collision frequency profile and/or to generate a test case for determining the ambient electron density profile. For example, by observing 5 distinct VLF signals which have propagated over HAARP, we could allocate 5 degrees of freedom to the ambient electron density profile and another 5 to the electron collision frequency profile. In this case it would not be necessary to predetermine the ambient electron density profile by other methods, such as those described in Chapter 3.